FACULTY OF SCIENCE
UNIVERSITY OF COPENHAGEN

Master's Thesis

Mikkel Skaarup

Diffractive pp interactions

A study of diffractive pp interactions at the LHC using a tagged proton at $\sqrt{s} = 8$ TeV

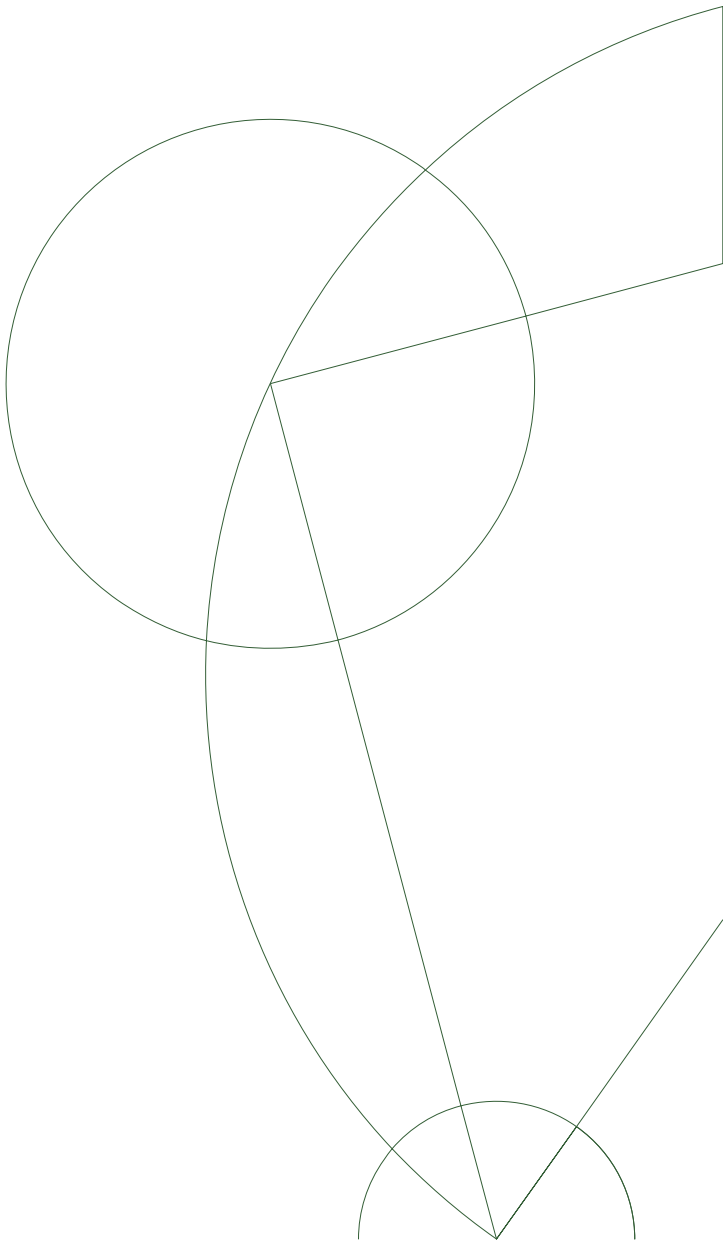

Supervisor: Peter Henrik Hansen

October 15, 2013

"It is of the highest importance in the art of detection to be able to recognize out of a number of facts which are incidental and which are vital... I would call your attention to the curious incident of the dog in the nighttime. The dog did nothing in the nighttime. That was the curious incident."
- Sir Arthur Conan Doyle

Abstract

This thesis is a study of diffractive processes in proton-proton (pp) collisions. To understand what these are and what to expect from them, a summary of the Standard Model and sections describing collider- and diffractive-physics are included. It is discussed that the experimental expectation is, for a single diffractive (SD) interaction, a proton scattered at very low angles on one side of the interaction point (IP) while the other proton breaks into a system of particles produced in the forward region. This is due to the colourless exchange of a diffractive interaction. A detailed description of the detectors used, ATLAS and ALFA, is also given.
A study of a SD event selection at collision energies of $\sqrt{s} = 8$ TeV is presented. The result of the selection is compared to a toy model Monte Carlo (MC) simulation using Pythia 8, and a rough agreement of this simple MC and data is seen. A selection of central diffraction (CD) is also discussed. As elastic events are background candidates to, especially, central diffractive events, a breif analysis of these is also presented, and they are used to remove background elastic events from the CD event selection. Diffractive parameters relevant to the selections are also discussed, such as the energy loss, ξ, and forward rapidity gap, $\Delta\eta_F$. It is seen that the SD selection provide energy loss and rapidity gap measurements that are in agreement with theory, but a more detailed study and simulations are needed for further conclusions. For CD events, a first look into event structures, such as the Bengtsson-Zerwas, Körner-Shierholtz-Willrodt and Nachtmann-Reiter angles, is presented as a first step towards measuring a triple-Pomeron vertex and the colour flow of CD interactions. As these are done using a naive approach, the result is preliminary.

Acknowledgements

First, I would like to thank Oldrich Kepka, who helped me enormously with the analysis. Thanks for answering all my questions and your suggestions on what to do next. Without your help and guidance this thesis would not have happended. And thank you for your help with programming when all hope seemed lost.
Likewise a great thank you goes to Tim Martin who also contributed greatly to the work done in this analysis. Thanks for taking the time to help me when I was stuck.
Thanks to the ALFA comunity at CERN for helping me with my elastic analysis when I had just started this thesis and later with ALFA related questions or parts of my analysis. Especially to Sune Jakobsen without whom I would not be writing on this subject. Thanks for taking the time and energy to kick the whole diffractive analysis team at Copenhagen into gear. Thank you for the time and interest in our work as well, and for answering questions left and right regarding the ALFA detector.
The HEP group at NBI deserves a thank you as well. For providing a welcome atmosphere at the office as well as being ready to answer any question or take any discussion that arose during the year. A special thank you goes to Jørgen Bech Hansen who was always around and willing to discuss just about everything.
Thanks to Gösta Gustafson who invited Simon, Morten and me to Lund to give a spontaneous lecture on Regge and diffractive theory. Along the same lines, a great thank you goes to Jorn Dines Hansen who basically knows everything about diffraction and was happy to share that knowledge.
A special thank you goes to my supervisor, Peter Hansen, for taking me on, be willing to answer questions, give comments on my thesis and always be around if I needed help.
Last, but definitely not least, a great big thank you to my office mates, Morten Ankersen Medici and Simon Stark Mortensen. For keeping me sane and for helping me out with any odd question that might pop into my head. It has been great to have other master students around to share experiences with and keeping a good atmosphere at the office.

Contents

1 Introduction

In high energy particle physics, the most successful theory to date is the Standard Model. Using the framework of quantum field theory, it describes the known fundamental particles, their interactions and the way they combine into composite particles, such as hadrons or atoms.
To study these particles, accelerators are used to collide beams of particles at high energies, and then, via large and complex detectors, study the remnants of the collision and any properties the event might have. The collisions can be categorised into three types. The first is elastic scattering where the two colliding particles emerge unaltered, except for changes in the kinematics of said particles. In this type of collision, the two elastic scattered particles are also the only particles involved in the interaction, i.e. no other final state particles were produced. This means that the kinetic energy of the two initial particles is unchanged. Elastic events are expected, at the energies considered in this thesis, to correspond to $\sim 20\%$ of the total amount of interactions (Ref. [1]).
Another type of collision is the inelastic interaction. Here, the kinetic energy of the initial particles is not conserved, and the result is the creation of a multi-particle final state. It is split into diffractive and non-diffractive collisions. In general, the multi-particle state of inelastic scattering is connected by colour. This is the second type of collision, called non-diffractive collisions, and this is the type of collision that occurs with the highest frequency. About $\sim 55\%$ of all events are expected to be non-diffractive events.
However, sometimes a colourless exchange occurs between the two initial particles resulting in the third type of collision, called diffractive interactions. If the exchange is colourless and with the quantum numbers of the vacuum, the result will be two separate systems of particles. This can happen in three different ways. The first is the single diffrative (SD) interaction which is when one of the initial particles emerges as a final state particle, but with an energy loss. The other initial particle breaks up into a multi-particle state which will, based on the energy, travel in roughly the same direction as the initial particle. This means that the final state consists of one of the initial particles and a system of new particles. These two systems are separated in space by a gap, a region empty of particles, and they move in the direction of the initial particle from which they originated. SD events are expected to correspond to $\sim 14\%$ of all collisions.
The second type of diffractive collision is the double diffractive (DD) interaction. Here both initial particles break up into multi-particle states, as the result of a colourless exchange with vacuum quantum numbers. The two systems are produced in two distinctive regions, i.e. they are separated by

a gap of a particle-empty region. Both SD and DD interactions are thought to occur as a result of a Pomeron exchange, and DD events are expected to correspond to $\sim 10\%$ of all events.
The last type of diffractive events is central diffractive (CD) interactions. This is thought to occur as the result of a collision of Pomerons from both of the initial particles. This means that the initial particles remain unchanged, except for a loss of energy and changed kinematics. In addition, the two colliding Pomerons result in a multi-particle final state. Each of these three systems, the two intial particles and the multi-particle state, are separated distinctly from the others by gaps where no particles are found. About $\sim 1\%$ of all events are expected to be CD events.
As diffractive events correspond to a significant percentage of the total cross section, somewhere around 25%, it is of great interest to study them. They are also expected to explain the collision energy dependence of the the total cross section.

In this thesis a study of diffractive events will be presented, and this is done using the Large Hadron Collidor (LHC), located beneath the border between France and Switzerland, just outside of Geneva. The LHC collides hadrons at the highest energies achieved so far, and in this thesis proton-proton (pp) diffractive events will be studied. It is a circular collider, and it has a circumference of 27 kilometres. To detect the results of a collision, detectors are placed at the interaction points around the ring. This thesis will use the ATLAS (A Toroidal LHC Apparatus) detector which is one of the four detectors of the LHC. Diffractive events have been studied before at the LHC, however the study in this thesis will use the ALFA (Absolute Luminosity For ATLAS) detector, which is located roughly 240 metres down the ring from ATLAS. The ALFA detector will be used to tag the surviving protons from a diffractive event, thus providing a more accurate selection of diffractive events. This, however, excludes DD events from the scope of this thesis. Therefore the analysis will only involve SD and CD events.

The aim of this thesis is to develop a selection of SD and CD events, using ALFA to tag the protons, and measure some of the properties of these events, such as the energy of the surviving protons and distributions of particles in ATLAS. In addition to this, one of the goals will be to look into one of the very core signatures of a diffractive event, the rapidity gap. This is the variable most commenly used to the describe the separation of the survining proton(s) and the multi-particle state, and it is expected to clearly separate non-diffractive events from diffractive events. As a part of the analysis, a look into elastic events will also be done as these are background candidates

to diffractive events. Previously, analysis has been carried out on diffractive events, however not with the use of a tagged proton at the collision energies of this thesis. Thus, this thesis will provide new results on SD and CD event signatures, such as the energy distribution of the diffractively scattered proton and the rapidity gap. The focus will be on the selection of diffractive events and what this implies for the measurable diffractive parameters as well as the background found in the selection.
As the diffractive events occur due to a colourless Pomeron exchange, it is interesting to measure the colour flow of the event. This is usually done using substructures of an event, such as multigaps and event shape angles. As a part of the work of this thesis, a first look into event shape angles will be presented for CD events. CD events are chosen as they are thought to occur as the result of a double Pomeron exchange, and therefore these studies could possibly lead to clarification on the presence of a triple-Pomeron vertex.

The thesis is build around three parts. Part one is the theory needed to understand diffractive events at high energy particle colliders. Section 2 will describe the Standard Model and the interactions involved, section 3 will give an introduction to the physics at high energy colliders and, in section 4, a shortened theoretical description of diffractive events will be given.
Part two is a detector description. This will include a general description of the LHC and the beam of the LHC in section 5. In section 6 a detailed desciption of the ATLAS detector will be given and finally section 7 will introduce the ALFA detector.
The third part is the analysis. Elastic events will be introduced in section 12, and a SD event selection will be developed in section 14. Likewise a CD event selection is discussed in section 15.

1.1 Definitions and units

In this thesis, units where $c = \hbar = 1$ are chosen. This means that the unit for mass, energy and momentum are the same as the difference lies in powers of c. The unit is electron volts (eV), defined as the energy an electron achieves by being accelerated through a 1 volt electric field. All interactions are pp collisions unless otherwise specified.
When considering four vectors, the notation will be regular letters with a greek index to denote the space time index, e.g. p^μ. Other vectors will be written using bold characters, e.g. $\mathbf{p} = (p_x, p_y, p_z)$.

Part I
Theory

2 The Standard Model

In the study of high energy particle physics, there is one theory that has been tested to a great degree and not yet failed. That theory is the Standard Model, describing the known fundamental particles and the interactions between them. As the particles involved in the analysis of this thesis are Standard Model particles, it is relevant to know their properties. This section will give an introduction to the particles and how they interact, and it is based on ref. [2] and [3].

In 1897 the electron was discovered by J. J. Thompson, and that laid the grounds for future particle physics experiments. This was the first elementary particle to be discovered, and it set off the field known today as high energy particle physics. Throughout the 20th century many more particles were discovered, and the Standard Model was formed towards the mid to the end of the century. The Standard Model combines the theory of relativity with quantum mechanics into quantum field theory. It describes the fundamental particles and their interactions via the fundamental forces, however it is not a complete description of nature as gravity is not included, and neither are other observed phenomena, like dark matter, included.
The four fundamental forces of nature are the strong and weak nuclear force, the electromagnetic force and gravity. The strong force is responsible for keeping quarks together in protons and neutrons as well as keeping the protons and neutrons together in nuclei. The range of the strong force is of the order 10^{-15} m or smaller. The weak force is the mechanism behind radioactive decays, such as a neutron decaying into a proton, and it acts on particles with a range of 10^{-17} to 10^{-16} m. Electromagnetism is the force keeping the electron in orbit around the proton, and it can act on particles at infinite range. Gravity, being the only force not included in the Standard Model, is not discussed in detail in this thesis. It also acts at infinite range, and it is the weakest of all four forces, but it is, nonetheless, the only force that acts over great distances, by keeping objects in the universe together and in orbit. The reason for this is the short range of the strong and weak forces and the fact that, although the electromagnetic force also has infinite range, it is electrically neutral to a degree that the net force is zero above distances the size of an atom. In order of relative strength, the forces are the

strong force, the electromagnetic force, the weak force and the gravitational force. The Standard Model describes interactions between the fundamental particles through three of these four fundamental forces.

A fundamental partice is a particle that cannot be divided into other particles. In the Standard Model, these are split into two groups, the bosons and the fermions. The fermions make up matter while the bosons mediate the forces between the fermions. The fermions are split further into two groups, leptons and quarks. Each group has a set of quantum numbers that are conserved in an interaction. The leptons include the electron, muon and tau as well as their corresponding neutrino. The muon and tau essentially acts as a heavier electron, and each pair of electron-like particle and neutrino represents a generation of leptons. Each generation carries a leptonic flavour quantum number called the electron, muonic or tauonic number. They are $+1$ for particles and -1 for antiparticles.
The quarks are the up, down, charmed, strange, top and bottom quarks. All quarks carry a baryon number of $1/3$, and the baryon number is conserved under all interactions. Like the leptons, they are split into generations, the first generation being the up and down, the second is the charmed and strange quark and the third generation is the top and bottom quark. The quark flavour quantum numbers are isospin, strangeness, charm, bottomness and topness, and this number is conserved under strong and electromagentic interactions. All quarks carry isospin of $\pm 1/2$ depending on whether they are up-like or down-like. The strange quark has strangeness -1, the charm quark has charm $+1$, the bottom quark has bottomness -1 and the top quark has topness $+1$. These are the only non-zero flavour quantum numbers. All fermions also have an antiparticle defined as a particle with the same mass but with opposite additive quantum numbers., i.e. the charge, baryon number and flavour quantum numbers.
The bosons includes the photon, the $W^{\pm}$ and Z bosons, the gluon and the Higgs boson. Each boson is thought to be responsible for one of the fundamental forces. The photon represents the electromagnetic interactions, the $W^{\pm}$ and Z bosons mediate the weak nuclear force and the gluon the strong force. The Higgs boson is thought to give mass to the other particles. The W^{+} boson's antiparticle is the W^{-} boson, and the photon, Z-boson and gluon are their own antiparticles. For a complete overview of the particles see figure 2.1.
In figure 2.1 the particles' electrical charge, mass and spin is also shown. Along with the charges of the strong and weak force, colour and weak isospin, and the quantum numbers of the particles, these are what allows or forbids an interaction between the particles. The particles in each group are all dif-

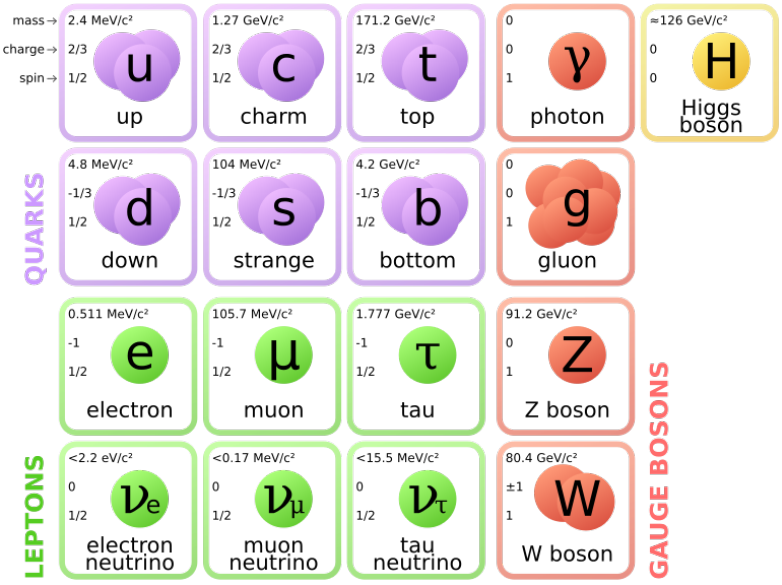

Figure 2.1: All the particles of the standard model. The name, spin, electric charge and mass is shown. They are split into subgroups of leptons (green), quarks (purple), bosons (red) and the Higgs boson (yellow). [32].

ferent, but they have similar traits, the most obvious being spin. Leptons and quarks all have spin 1/2 while the bosons all have integer spin. Leptons also have integer charge in units of e, the fundamental charge equal to 1.602×10^{-19} Coulombs, while quarks have non-integer charges of either $-1/3$ e or 2/3 e. All fermions carry weak isospin. The electron-like particles have isospin $-1/2$, the neutrinoes have $+1/2$, the up-type quarks carry isospin $+1/2$ and the down-type quarks carry $-1/2$. In addition, the quarks and gluons carries a colour charge of either red, green or blue. The colours does not refer to actual colour, but it is rather an electric charge-like component of the quarks and gluons. It represent the fact that the world is colourless above the quark level, meaning that particles that can propagate freely in the vacuum carry a total colour charge of white, where white represents either one of each colour or a colour and the same anti-colour. This is referred to as colour confinement. It is these charges that the bosons couple to. The photon couples to electric charge, the $W^{\pm}$ and Z bosons couple to the isospin and the gluon couples to colour.

2.1 Interactions of Particles

The interactions of the fundamental particles are described theoretically by a gauge quantum field theory. The details of this is not important to the aim of this thesis, and therefore only some of the results will be introduced here, without great mathematical description. In addition, Feynman diagrams will also be introduced to explain and display the interactions needed in the further analysis of this thesis.

To kinematically describe a relativistic free field one uses a Lagrangian density of the form

$$\mathscr{L} = \frac{1}{2}\partial^\mu\phi\partial_\mu\phi - \frac{m^2}{2}|\phi|^2 \quad , \tag{2.1}$$

where ϕ is the field, m is the mass of the field and μ refers to the space-time indicies. The first term is the kinetic term, and the second is the mass term. In gauge theory one requires the Lagrangian to be invariant under local gauge transformations, and, in order to ensure this symmetry is preserved, a gauge field is introduced. This means that, in the kinematic term in the Lagrangian, the derivative is replaced by

$$\partial_\mu \rightarrow D_\mu = \partial_\mu + igA_\mu \quad , \tag{2.2}$$

where A_μ is the gauge field and g is the coupling constant between the field and the gauge field, describing the strength of the interaction. If this new covariant derivative is used in the free field lagrangian of equation 2.1, four kinetic terms appear. One is the original kinematic term of the field while the three others, of the form

$$\sim gA^\mu\phi\partial_\mu\phi, \quad \sim g\partial^\mu\phi A_\mu\phi \quad \text{and} \quad \sim g^2A^\mu\phi A_\mu\phi, \tag{2.3}$$

correspond to the interactions of the field with the gauge field. This is the basic principle for a bosonic free field theory, and it has no real relevance for the Standard Model except to explain the principle of gauge theory. The gauge boson, A_μ, corresponds to the force carrier of this simple theory.
The gauge bosons of the Standard Model are the photon, the $W^\pm$ boson, the Z boson and the gluon. However, in gauge theory the gauge boson can never have a mass, and therefore the Higgs field is introduced which spontaneously breaks the gauge symmetry. This is what gives rise to the masses of the fermions and the $W^\pm$ and Z bosons. The excitations of the Higgs field is the scalar Higgs particle. This also requires the unification of the electromagnetic and weak force into the electroweak force.
The result is that the electromagnetic force has the following coupling terms

$$\gamma l^+l^-, \quad \gamma q\overline{q}, \tag{2.4}$$

where γ is the photon, $l^{\pm}$ represent an electron-like lepton, $\overline{q}$ is an antiquark and q is a quark. The coupling constant is g_{em}, and it is proportional to the fine-structure constant, $\alpha \sim 1/137$. The gluon has the coupling terms

$$gq\overline{q}, \tag{2.5}$$

where g represents the gluon. Note that there are in fact 8 different gluons because of the different colour combinations available in a $gq\overline{q}$ interaction. The coupling constant is g_s, and it is proportional to the fine structure constant of the strong force, $\alpha_s \sim 0.1$. And last, the weak force has the following coupling terms

$$W^{\pm}q\overline{q}', \quad W^{\pm}l^{\mp}\nu_l, \quad Zq\overline{q}, \quad Zl^+l^-, \quad Z\nu_l\overline{\nu_l}, \tag{2.6}$$

where ν_l corresponds to a neutrino of the same type as the lepton, l. For the $W^{\pm}q\overline{q}'$ interaction it is required that the quark pair is from the same generation and that the $W^{\pm}$ mediating the interaction conserves the charge. However the generations of the weak interactions are not quite the same as those of other interactions, but rather a linear combination of the latter. This feature is called quark mixing. The coupling constant is g_W, and it is proportional to $\alpha_W \sim 1/30$. These are the allowed interactions of fermions in the Standard Model.
These, however, are not all of the allowed interactions of the Standard Model. The symmetry used to describe the Standard Model is $U(1) \times SU(2) \times SU(3)$, where the $SU(3)$ part give rise to the stong interactions and the $U(1) \times SU(2)$ corresponds to the electroweak interactions. The electromagnetic force is only described by a subgroup of the $U(1)$ part of the electroweak symmetry, and because the photon has no electric charge, it does not couple to itself. The weak interactions are described by the rest of the $U(1) \times SU(2)$ part. The fact that the weak and strong force are described by a higher symmetry is what gives rise to more than one boson mediating the weak and strong forces. Because these carry the weak isospin and colour charges, this also gives rise to self-coupling terms of the gluon, $W^{\pm}$ and Z bosons,

$$ggg, \quad gggg, \quad W^+W^-ZZ, \quad W^+W^-W^+W^-, \quad W^+W^-Z. \tag{2.7}$$

Because the $W^{\pm}$ carry electric charge, they can also couple to the photon, giving the couplings

$$W^+W^-\gamma, \quad W^+W^-\gamma\gamma, \quad W^+W^-\gamma Z. \tag{2.8}$$

Last, the Higgs couples to mass, and it can therefore interact with any particle that have a mass.

The allowed vertices in the Standard Model have been introduced, but there exists additional multiplicative discrete symmetries that are conserved in some particle interactions. These are the charge (C), parity (P) and time (T) reversal symmetries.
The charge symmetry, when acting on a particle, flips all charge quantum numbers. These include electric charge, baryon and lepton numbers as well as the quark numbers, isospin, strangeness, charm, bottomness and topness. It does not change the momentum, mass or enegy of the particle, and the result is that the particle is converted into its antiparticle.
Parity operations flips the sign of the spatial coordinates while leaving the sign of the time component. This affects a number of particle variables. For instance, under a parity transformation the spin projection on the momentum direction is changed from left- to right-handed, and the velocity, acceleration, force and electric field are all reversed.
The last symmetry, time reversal, implies excatly what the name suggests. An interaction should also be possible in the reverse direction, i.e. $\mu^+ + \mu^- \rightarrow e^+ + e^-$ implies that $e^+ + e^- \rightarrow \mu^- + \mu^+$ is also possible. Although, in this case, the reverse interaction is limited in possiblity by energy and momentum conservation. Because the muons are essentially heavier electrons, it is required that the electrons have high energy and momentum in order for the reverse interaction to occur.
The CPT-theorem requires that any quantum field theory must have CPT symmetry, i.e. be invariant under the simultaneous application of all three operations. Hence it is already built into the Standard Model, but it can be worth mentioning some consequences of this, especially because purely electromagnetic interactions conserve C, P and T operations separately. As does the strong interaction. This forbids certain interactions. For example, the decay $\pi^0 \rightarrow \gamma + \gamma$ is allowed by the C conjugation while $\pi^0 \rightarrow \gamma + \gamma + \gamma$ is not as the photon has $C = -1$ and the π^0 has $C = +1$.

Previously vertices has been mentioned. This refers to Feynman diagrams, which is a tool used in high energy particle physics to calculate amplitudes for a certain interactions or decays. The square of an amplitude determines the probability for a certain interaction to occur. However, in this thesis, the diagrams will only be used to display interactions. An example of a Feynman diagram can be seen in figure 2.2. The figure shows a scattering of two electrons via the exchange of a photon. The diagram is drawn such that moving from left to right corresponds to moving forward in time. Likewise, going up and down corresponds to moving in space. This way the two electrons move towards each other until they come close enough for a photon to be

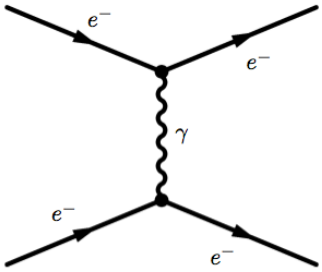

Figure 2.2: An example of a Feynmann diagram, describing the scattering process $e^- + e^- \rightarrow e^- + e^-$.

exchanged between them, changing their direction and thus scatter of each other. The reason that γ is drawn exactly horisontally is that, when calculating the amplitude of this interaction in quantum field theory, one has to consider both the diagram where the upper e^- emits the photon, i.e. the photon slope going from the upper electron to the lower in time, but also the diagram where the opposite is true, i.e. the photon being emitted from the lower electron. When calculating the combined amplitude, it is found that all the terms cancel except the horizontal contribution.

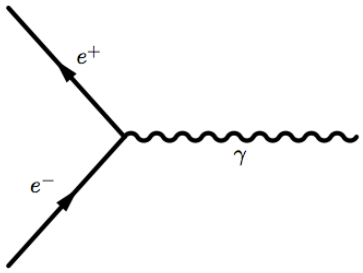

Figure 2.3: An example of a Feynman diagram with a virtual photon.

In some diagrams there will be vertices that are not possible due to momentum conservation. In figure 2.3, an electron and positron annihilate to create a photon. In the center of mass frame, the initial momentum will be zero however the photon cannot possibly have zero momentum, and therefore momentum conservation is violated, and the interaction is not possible. However, within a larger diagram, this vertex is allowed because the photon emitted is not a real particle but a virtual particle, and virtual particles can have any mass. This is often said as being on- and off-shell, where on-shell refers to real particles carrying real mass while off-shell particles are virtual and can have any mass but cannot be represented as a final state particle.

3 Collider Physics

This section will describe the relevant physics involved in high energy particle collisions. The purpose is to describe, theoretically, the interactions used in the later analysis. This includes the kinematics of the colliding particles, some mechanisms involved in high energy particle collisions and parameters relevant for collisions. Only proton-proton (pp) collisions will be discussed, unless otherwise specified, as these are the ones used in the analysis. This section is based on ref. [2] and [7].

In pp collisions, the protons travel at relativistic speed. This means that total energy and momentum is always conserved, but mass is not, except for elastic collisions. Total energy and momentum conservation in particle collisions can be expressed with four vectors called the four momentum,

$$p_1^\mu + p_2^\mu = p_3^\mu + p_4^\mu + ... + p_N^\mu \quad , \tag{3.1}$$

where 1, 2, 3 and so on refers to different particles, and μ is the four index ranging from 0 to 3. The 0th component is the total energy of the particle and the 1st, 2nd and 3rd refers to the x-, y-, z-components of the momentum.
A two body process, i.e. with two initial- and two final-state particles, is shown in figure 3.1. Notice that the outgoing particles are not necessarily the same as the incoming. In that case, $1 + 2 \to 1' + 2'$, the interaction is an elastic scattering, and although the original particles have altered kinematics they remain the same particles. In the center-of-mass (CM) system, the four

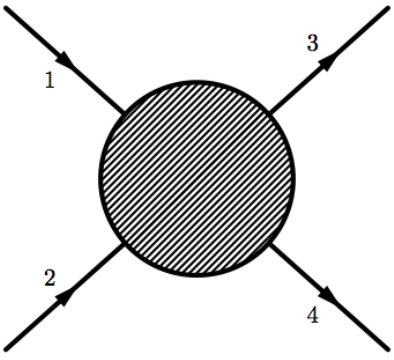

Figure 3.1: A Feynman diagram showing the two body process $1+2 \to 3+4$.

vectors describing the particles before and after are

$$\begin{aligned} p_1 &= (E_1, 0, 0, p_z) \\ p_2 &= (E_2, 0, 0, -p_z) \\ p_3 &= (E_3, \mathbf{p}_T, p'_z) \\ p_4 &= (E_4, -\mathbf{p}_T, -p'_z) \quad , \end{aligned} \tag{3.2}$$

where $\mathbf{p}_T$ is the transverse two compontent momentum. The twobody process is described by two variables normally chosen from the Mandelstam variables, defined as

$$\begin{aligned} s &= (p_1 + p_2)^2 = (p_3 + p_4)^2 \\ t &= (p_1 - p_3)^2 = (p_2 - p_4)^2 \\ u &= (p_1 - p_4)^2 = (p_2 - p_3)^2 \quad . \end{aligned} \tag{3.3}$$

The blob shown in figure 3.1 represents all possible exchanges and interaction that would lead to a final state with particle 3 and 4. Consider now a specific bosonic exchange of the blob. This exchange can occur in the three different channels of equation 3.3. Figure 3.2 shows the different exchange channels in Feynman diagrams.

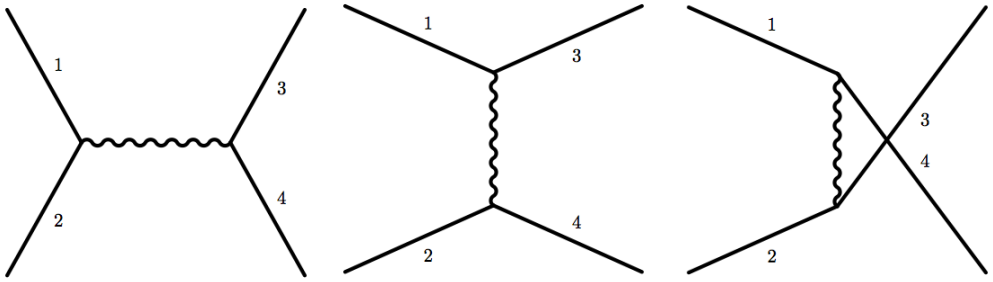

(a) (b) (c)

Figure 3.2: The different exchange channels that can occur, given a specific bosonic exchange that leads to the reaction $1 + 2 \rightarrow 3 + 4$. (a) is the s channel, (b) is the t channel and (c) is the u channel.

The different channels represents the possible momentum flows of the interaction. The s channel represents the interaction where particle 1 and 2 collide, become the intermediate boson for a short period of time and then decays into particle 3 and 4. In the t channel particle 1, for example, emits a boson while decaying to particle 3. Particle 2 then absorbs the boson causing it to become particle 4. The u channel is the same as the t channel except the

order of the final state particles has been changed. Therefore, in the u and t channels, a momentum transfer occurs between the two particles whereas in the s channel the incoming momenta is combined to a whole new set of particles.
For the two body interaction shown in figure 3.1, s is equal to the square of the CM energy. Therefore the CM energy is often written as $\sqrt{s}$ for two body collisions and will be for the rest of this thesis.
In particle collisions, many different particles can be part of the final state particles. Some of these however have a short lifetime. The $Z, W^{\pm}$ bosons, for example, have a lifetime of the order 10^{-25} s, meaning they decay before detectors have any chance of seeing them. Therefore, they are identified by looking at the mass spectrum of their decay products. In this spectrum there will be a mass peak, or resonance, around the true mass of the boson.

When considering particle collisions, the actual hit mechanism is different from what is seen in everyday life. Due to the size and velocity of the particles, it is not a simple case of hit-or-miss, but it is rather a question of what, how close and how. The cross section is a way to describe this by expressing the likelihood of certain interactions between particles. Suppose a particle, an electron, is travelling towards a stationary target, a proton. The proton then acts as a potential for the electron, meaning that the electron will be scattered off the proton by some angle θ. The size of the angle depends on the impact parameter, b, which describes the closest distance between the center of the potential and the electron, had it not been scattered. If instead the incoming particle had an impact parameter of $b + \mathrm{d}b$ the scattering angle would have been $\theta + \mathrm{d}\theta$, or more generally, if the particle travels through an infinitesimal area $\mathrm{d}\sigma$, it will be scattered by a solid angle of $\mathrm{d}\Omega$. The cross section, $\mathrm{d}\sigma$, represents the probability per unit time, per unit flux of the incoming beam and per unit area density of target particles, for scattering the beam out into the solid angle. Therefore the total cross section is the integral of $\mathrm{d}\sigma$ over all solid angles. This can be generalised to two beams of incoming particles with luminosity, L, where luminosity is the number of particles passing each other per unit time, per unit area. Then $\mathrm{d}N = L\mathrm{d}\sigma$, where $\mathrm{d}N$ is the number of particles scattered per unit time, and the differential scattering cross section can be defined as

$$\frac{\mathrm{d}\sigma}{\mathrm{d}\Omega} = \frac{\mathrm{d}N}{L\mathrm{d}\Omega} \quad . \tag{3.4}$$

The cross section is usually given in units of nb or pb where a barn is defined as $b = 10^{-28}$ m^2. This equation also leads to $N = \sigma L$ when all solid angles are considered. The luminosity can be thought of as a potential number of

collisions per unit area per unit time. The integrated luminosity is used as a measure of the size of collected data. It is defined as

$$\int L \mathrm{d}t \quad , \tag{3.5}$$

and it is often expressed in terms of the inverse cross section, i.e. in units of pb^{-1} or nb^{-1}.
The above describes the process $e + p \rightarrow e + p$, i.e. an elastic collision. However the idea is the same when decribing other collisions, such as a pp collision. In this case there are many outcomes depending on what type of interaction occurs as well as what forces are involed. The type of collision can be either elastic, non-diffractive or diffractive. The diffractive interactions are described in section 4. Non-diffractive events describe events with a momentum and colour transfer between the two initial particles. The total cross section is then a sum of all possible interaction cross sections,

$$\sigma_{\mathrm{Tot}} = \sigma_{\mathrm{ND}} + \sigma_{\mathrm{elastic}} + \sigma_{\mathrm{SD}} + \sigma_{\mathrm{DD}} + \sigma_{\mathrm{CD}} \quad . \tag{3.6}$$

The proton is a composite particle, consisting of three quarks, two up- and one down-quark. This is at energy scales the size of the binding energy of the proton, the QCD scale, $\Lambda_{QCD} \sim 200$ MeV. However at the energies at modern colliders the transverse momentum is by far greater than this. This type of collision is referred to as being 'hard'. The proton is thought of as consisting of three valence quarks, $u + u + d$, and a 'sea' of other quarks and gluons. In addition, when the proton aquires large amounts of energy, it becomes larger. This is due to the fact that the strong force holding the proton together becomes weaker at high energies, and thus the internal quarks and gluons are more loosely bound together. To a limit, as colour confinement is still active.

The probability of extracting a given quark or gluon is given by a parton distribution function, $f_i(x)$, where i referes to which parton is described and x is the proton momentum fraction of the parton. In a collision, when the two extracted partons collide, the rest of the proton form what is called the underlying event. This consist of 'soft', $\mathbf{p}_T \sim 0.4$ GeV, particles, mostly pions. An overview of this is shown in figure 3.3.
Which particles make up the collision is determined by the parton distribution functions, and these are experimentally determined. Figure 3.4 shows the distribution function, given a collision occurs, of extracting a certain parton with momentum fraction x. This distribution depends on the mass scale,

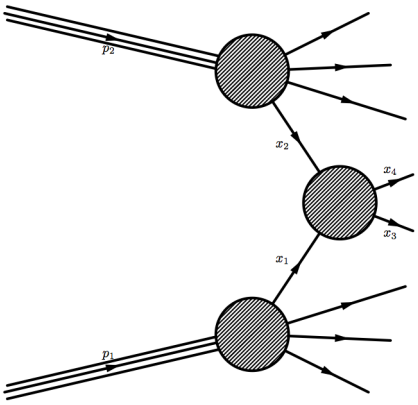

Figure 3.3: A figure showing the proton-proton interaction at a collider, including the underlying event as the remnants of the two initial protons, p_1 and p_2. x_1, x_2, x_3 and x_4 are momentum fractions of the initial protons.

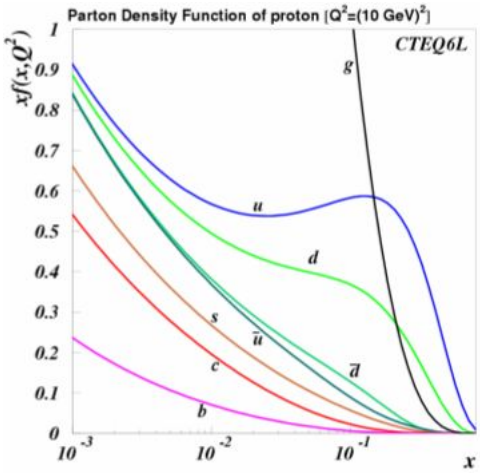

Figure 3.4: The probability of finding a parton with a certain momentum fraction from the proton-proton collision. [33].

Q, at which the collision occurs, however this variation is slow, $\sim$ logarithmic. QCD pertubation theory can predict the behaviour at different mass scales, and the result is that all the distributons in figure 3.4 are squeezed towards lower x. This means that, when Q increases so does the probability of finding a low x parton while the higher x partons become less likely. Note also that the most probable parton extraction is the gluon with a low x. This means that the LHC is basically a gluon-gluon collider due to the high mass scales available.
The next step in figure 3.3 is the actual interaction. This can be virtually

anything depending on the parton extracted and the colour carried by those partons. The result of the interaction is the final state particles. In a few cases, when the final state particles involves, for example, electrons, muons or neutrinoes, these particle remain long enough for a detector to detect them. In most cases however, the final state particles will be quarks and gluons, and because of colour confinement they cannot exist on their own. Therefore if an interaction has quarks or gluons as the final state particle, a quark-antiquark pair is pulled from the vacuum to ensure colour neutrality. These quarks, together with the one from the final state, then bind together to form hadrons or mesons. This will happen a number of times, resulting in a jet of different hadrons in a cone around the original quarks direction. This process is called hadronisation, and figure 3.5 gives an overview of this process. The process is not entirely understood. The limit between a single quark or gluon pulling more quarks from the vacuum, to actual mesons and baryons in particular is not well defined, and can be seen in figure 3.5 as the grey blobs. Notice also that in figure 3.5, an example of colour connections is shown. Due to colour conservation of an interaction, the final state particles can be colour connected, and hence the final state quarks are also typically colour connected.

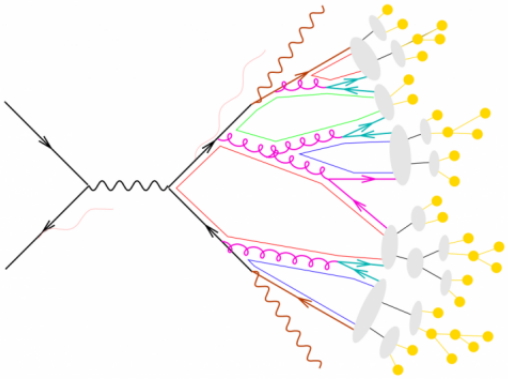

Figure 3.5: The hadronisation process. An example of colour connection is also shown. [34].

An example of initial state radiation (ISR) and final state radiation (FSR) is shown in figure 3.6. ISR is defined as one of the partons, pulled from the colliding protons, radiating a boson before the main interaction happens. Likewise, final state radiation is when one of the final state particles radiate a boson. Both types causes additional jet structures in the final state of the interaction.
Depending on the CM-energy of the collision and the momentum fraction

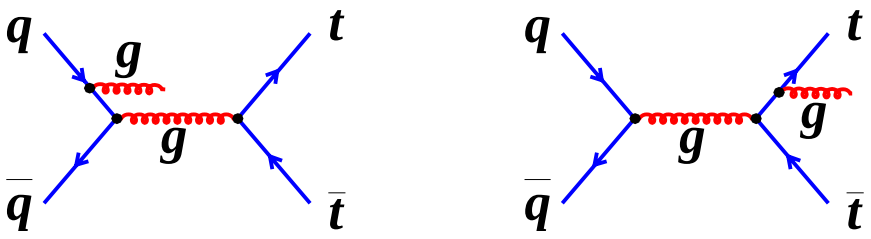

(a) (b)

Figure 3.6: (a) shows a Feynamn diagram with initial state radiation. (b) shows the same for final state radiation. [35].

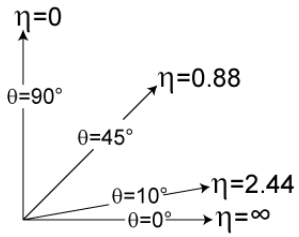

Figure 3.7: The numerical values of pseudorapidity and the corresponding angle between the incoming protons direction and the particle produced. [36].

of the colliding partons, the resulting particles and jets will be more or less forward. Forward refers to particles moving closely along the path the initial proton would have followed had there been no interaction. A measure of how forward a jet or particle is, is the rapidty. Rapidity is an additive speed variable for relativistic particles. It is defined as

$$y = \frac{1}{2} \ln \frac{E + p_z}{E - p_z} \quad , \tag{3.7}$$

where E is the energy of the particle and p_z is the momentum in the z-direction, the initial direction. However in experimental particle physics, one usually uses pseudo-rapidity instead. The definition is

$$\eta = \frac{1}{2} \ln \frac{|\mathbf{p}| + p_z}{|\mathbf{p}| - p_z} \quad , \tag{3.8}$$

where $|\mathbf{p}|$ is the size of the spatial momentum of the particle. In the limit where the speed of the particle is close to the speed of light or the mass of the particle is close to zero, these two definition are approximately equal. In the rest of this thesis mentions of rapidity will refer to η and not to y.
In figure 3.7 different values of η and the corresponding angles are shown.

The scattering angle, θ, is defined as the angle between the incoming particle direction and the track or jet. Rapidity is often preferred over the angle because particle production at a collider experiment is roughly constant as a function of η.
There is a kinematic limit to the maximum value of rapidity depending on the energy of the collision. However at rapidity zero, the particle production is roughly constant meaning that the distribution of particles will be constant. This is often referred to as the rapidity plateau. For the LHC, the size of the plateau is $\Delta\eta \sim 6$.
Another variable used to describe events is the azimuthal angle, ϕ. It is defined as the angle between the x axis and the transverse momentum, $\mathbf{p}_T$. It describes where in the transverse plane a track or jet is found.

4 Diffractive Physics

In this section, the physics behind diffractive events will be introduced as a theoretical description and reasoning for diffractive events at high energy collisions. This includes an introduction of diffractive events signatures, the S-matrix, Regge theory and the so called Pomeron. This section is based on ref. [4] and [5].

When considering high energy particle collisions, there are various ways a collision can occur. The total cross section can be divided into two parts, the elastic cross section and the inelastic cross section. Elastic scattering is defined by the inital particles emerging from the scattering without any exchange of quantum numbers and no multi-particle final state. A multi-particle final state refers to final states with either more or different particles than the two initial protons. Elastic scattering is expressed as

$$1 + 2 \to 1' + 2' \quad , \tag{4.1}$$

where $1'$ and $2'$ refers to the particles' different kinematics after the scattering. The inelastic cross section can be divided into diffractive and non-diffractive events. Non-diffractive events are events with multi-particle final states that include a colour quantum number exchange between the protons,

$$1 + 2 \to X \quad , \tag{4.2}$$

where X refers to the system of final state particles. Diffractive events are defined as events which result in multi-particle final states but with a vacuum quantum number exchange between the two initial protons. However this

definition is not sufficient to distinguish between non-diffractive and diffractive events experimentally. In non-diffractive events, the large rapidity gaps in the final state are exponentially suppressed,

$$\frac{\mathrm{d}N}{\mathrm{d}\Delta\eta} \sim e^{-\Delta\eta} \quad , \tag{4.3}$$

where $\Delta\eta$ is the largest rapidity gap. A rapidity gap is defined as a region in η that is empty of particles. This suppression is due to the colour quantum number exchange between the two protons. After a colour exchange, the two systems are moving apart pulling a colour field between them. Neither system is colour neutral and the energy of this field is roughly proportional to the separation, and therefore, when the separation becomes of the order one unit in rapidity, new particles will be created to fill the rapidity gap.
To ensure that there are two seperate systems, with the same quantum numbers as the two incoming protons, it is required that there is a large, non-exponentially suppressed, rapidity gap distribution of the final state,

$$\frac{\mathrm{d}N}{\mathrm{d}\Delta\eta} \sim \text{constant} \quad . \tag{4.4}$$

These are the two conditions of a diffractive event,

- No colour exchange
- Non-exponentially suppressed rapidity gap distributions of the final state.

There are three kinds of diffractive events, single-, double- and central-diffractive. By definition, these events occur due to the exchange of another colourless object than a particle. The theory describing this exchange is Regge theory. It describes hadronic interactions at high energies as an exchange of an object rather than a particle. These objects are called Reggeons. The Reggeon responsible for diffractive events is called the Pomeron. Single diffractive (SD) events occur by the exchange of a Pomeron, causing one of the protons to emerge unchanged, except for kinematic changes, while the other proton results in a multi-particle state, M_X. M_X is, for the rest of this thesis, also referred to as the diffractive mass system, and it represents the remnants of the diffractive interaction that is not the initial proton. Here p', the diffractive proton, and M_X is by definition separated by a rapidity gap. Likewise double diffraction (DD) is the result of a Pomeron exchange leaving both protons as multi-particle final states, M_{X_1} and M_{X_2}, separated by a rapidity gap. Central diffraction (CD) is slightly different as it is a Pomeron

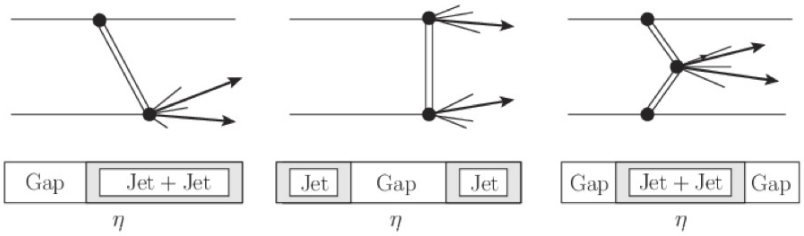

Figure 4.1: Single- (left), double- (middle) and central-diffraction (right). The interactions are shown both via a diagram and the gap distribution. [37].

from both protons interacting, via a double Pomeron interaction, resulting in a multi-particle final state, M_X, while both protons remain intact, p_1' and p_2'. A large rapidity gap separates p_1' from M_X, but a gap also separates M_X from p_2'. The interactions,

$$\begin{aligned} 1+2 &\underset{\text{SD}}{\rightarrow} 1' + M_X \\ 1+2 &\underset{\text{DD}}{\rightarrow} M_{X_1} + M_{X_2} \\ 1+2 &\underset{\text{CD}}{\rightarrow} 1' + M_X + 2' \quad , \end{aligned} \tag{4.5}$$

are shown in figure 4.1.
Kinematically, focusing on SD events, diffractive events are described by the momenta and energy of the particles involved. Using the approximations derived in appendix A, one finds that the variables useful to describe the event are

$$\begin{aligned} s &= (p_1 + p_2)^2 \\ x_F &= \frac{|p_z'|}{p_z} \\ \mathbf{p}_t^2 &= p_1'^2 \sin^2\theta \quad , \end{aligned} \tag{4.6}$$

where x_F is the momentum fraction of the proton. In appendix A, a theoretical gap size is also found to be

$$\xi \equiv 1 - x_F = e^{-\Delta\eta} \sim \frac{M_X^2}{s} \quad , \tag{4.7}$$

where $\Delta\eta$ is the rapidity gap and the last step is an approximation of ξ valid only when $s, M_X^2 \gg m_3^2, \mathbf{p}_T^2$. ξ is the energy loss of the diffractive proton, and this is the main variable used in the later analysis.

4.1 Regge Theory

This section will discuss the current theories regarding diffraction using Regge theory and Pomeron physics. The discussion will not be in great detail and only the important results will be shown here. Details can be found in ref. [4] and [5].

In order to understand Regge theory, one needs to briefly consider the relativistic S-matrix. Consider orthonormal states $\langle f|$ and $|i\rangle$, where $\langle f|f\rangle = \langle i|i\rangle = 1$ and $\langle f|f'\rangle = \delta_{ff'}$. i represents the initial states and f the final states. The S-matrix is defined such that the probability, given an initial state i, of finding the system in the final state f is

$$P_{if} = |\langle f|S|i\rangle|^2 = \langle i|S^\dagger|f\rangle\langle f|S|i\rangle \quad . \tag{4.8}$$

Given that the orthonormal set of final states, f, is complete, S is unitary, $S^\dagger S = SS^\dagger = 1$. S can be rewritten in terms of the transition matrix T as $S = \mathbb{1} + iT$. Then $\langle f|S|i\rangle$, for the process $1 + 2 \to 3 + 4 + ... + N$, can be written in terms of T as

$$\langle f|S|i\rangle = \langle p_3 p_4 ... p_N|\mathbb{1} + iT|p_1 p_2\rangle = \mathbb{1} + i(2\pi)^4\delta^4(p_f - p_i)\langle f|A|i\rangle \tag{4.9}$$

where the momentum conservation has been extracted from T. Here A is the amplitude of the interaction, p_f is the sum of final state four momenta and p_i is the sum of four momenta of the initial state. This leads to, from quantum field theory, a total cross section of

$$\sigma^{\text{Tot}}_{1+2\to N} = \frac{1}{4|p_1|\sqrt{s}} \sum_{n=3}^{N} (2\pi)^4\delta^4(p_n - p_1 - p_2)|\langle f|A|i\rangle|^2 \quad , \tag{4.10}$$

where p_n is the four momentum of the n'th particle in the final state. A represents the relativistic scattering amplitude, and since this includes an integral over the four-momentum of the form

$$\int \mathrm{d}^4 p \delta(p^2 - m^2) = \int \frac{\mathrm{d}^3\mathbf{p}}{2p_0}\theta(p_0) \quad , \tag{4.11}$$

the cross section can be written as

$$\begin{aligned}\sigma^{\text{Tot}}_{1+2\to N} =& \frac{1}{4|p_1|\sqrt{s}} \int \left(\prod_{n=3}^{N} \frac{\mathrm{d}^3 p_n}{2E_n(2\pi)^3}\right) (2\pi)^4\delta(\sum_{n=3}^{N} p_n - p_1 - p_2) \\ & \times |\langle p_3 p_4 ... p_N|A|p_1 p_2\rangle|^2 \quad .\end{aligned} \tag{4.12}$$

Consider the two body process, $1 + 2 \to 3 + 4$, with equal masses, and this will reduce to

$$\mathrm{d}\sigma = \frac{1}{16\pi^2 s(s-4m^2)} |\langle p_3 p_4 | A | p_1 p_2 \rangle|^2 \quad . \tag{4.13}$$

Generally one has to average over initial spins and sum over final state spins in order for this to be true.

The unitarity of S leads to

$$\mathbb{1} = (\mathbb{1} - iT^\dagger)(\mathbb{1} + iT) \Rightarrow i(T^\dagger - T) = T^\dagger T \quad , \tag{4.14}$$

which gives

$$\langle j|T|i\rangle - \langle j|T^\dagger|i\rangle = (2\pi)^4 i \sum_{n=3}^{N} \delta(p_n - p_i) |\langle i|A|j\rangle|^2 \quad . \tag{4.15}$$

Considering the elatic case $i = j$, the left hand side becomes $2\mathrm{Im}\langle i|A|i\rangle$. The right hand side can be identified with part of the right hand side of equation 4.12. Hence the elastic amplitude relates to the total cross section as

$$\sigma_{12}^{\mathrm{Tot}} = \frac{1}{2|p_1|\sqrt{s}} \mathrm{Im} A(s, t = 0) \quad . \tag{4.16}$$

This is the optical theorem, and it has certain consequences that are relevant for Regge theory and diffractive physics which will be discussed later. Notice that the total cross section depends on the center of mass energy of the collision, $\sqrt{s}$.

In a two body process, it is found that the existence of a forward production peak of particles depends on the quantum numbers of the exchanged particles. A forward peak requires a low momentum transfer, i.e. small t. It is also seen that interactions that have no forward peak of particle resonances also have a significantly lower cross section. An example of this is the process $K^- + p \to \pi^- + \Sigma^+$ and $K^- + p \to \pi^+ + \Sigma^-$. The interaction involving $\pi^- + \Sigma^+$ has a forward peak, a higher cross section, zero charge exchange, and the possiblity of either a $\frac{1}{2}$ or $\frac{3}{2}$ isospin exchange in the t channel. The other interaction can only have exchanges of $\frac{3}{2}$ isospin in the t channel as well as a charge exchange. Since there is no meson with these quantum numbers, the former interaction is more likely because, for example, the meson K*(890) can be exchanged in the t channel. It is also seen that the cross section of the interaction with $\pi^- + \Sigma^+$ decreases slower with center of mass energy in

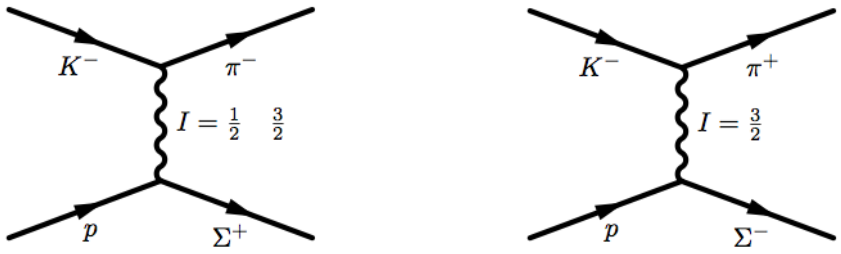

(a) (b)

Figure 4.2: The two interactions, (a) $K^- + p \to \pi^- + \Sigma^+$ and (b) $K^- + p \to \pi^+ + \Sigma^-$. The allowed isospin exchanges are also shown. The bosonic line represents all possible exchanges in this figure.

the low regime, $\sqrt{s} < 20$ GeV. Both interactions can be seen in figure 4.2 along with the allowed isospin exchange.
The total cross section is not described solely through a few of these exchanges. It can be described through the use of partial wave series in the t channel for spinless particles,

$$A(s,t) = 16\pi \sum_{l=0}^{\infty} (2l+1) A_l(t) P_l(z_t) \quad , \tag{4.17}$$

where l is the angular momentum, $z_t = 1 + 2s/(t - 4m^2)$ and $P_l(z_t)$ are the Legendre polynomials. It is easy to see that for $s \to \infty$, z_t equally goes to infinity. This leads to $P_l(z_t) \sim s^l$ which diverges.
Consider, instead of a series of partial waves, a single resonance being exchanged. This would mean that the sum in equation 4.17 would collapse into a single term with the spin of said resonance, σ,

$$\begin{aligned} A(s,t) =& 16\pi(2\sigma+1) A_\sigma(t) P_\sigma \left(1 + \frac{2s}{t-4m^2}\right) \\ \sim& f(t) s^\sigma \quad , \end{aligned} \tag{4.18}$$

where the last approximation is valid for large s. Combining this with the total cross section found in equation 4.16 it is seen that the cross section, as a function of center of mass energy, goes as $\sigma^{\text{Tot}} \sim s^{\sigma-1}$. Hence a particle of spin 0 would give rise to a cross section that decreases as s^{-1}, the contribution to the cross section of a particle of spin 1 does not depend on s and a particle of spin 2 gives a cross section that rises linearly with s. This could explain the rise in the total cross section for higher s, however there exists a bound on the total cross section called the Froissart-Martin bound. It states that

the total cross section cannot grow faster than

$$\sigma^{\text{Tot}} \leq C \ln^2 s, \quad \text{for } s \to \infty \quad , \tag{4.19}$$

where C is some constant. As it turns out this type of contribution, $s^{\sigma-1}$, is not seen in data.
Consider instead the exchanged resonances contributing collectively, as a family of mesons. A family of mesons or resonances is then a group of mesons, contributing simultaneously to the total cross section. In a family, two mesons cannot have the same spin. This is the idea of Regge theory. Regge found that the partial wave amplitudes, $A_l(t)$, can be considered as a function of a complex angluar momentum, l, as $A(l,t)$. This leads to singularities, or poles, of $A(l,t)$ decribed by

$$l = \alpha(t) \quad , \tag{4.20}$$

in the complex plane of l. These poles are referred to as Regge poles and the function $\alpha(t)$ as a Regge trajectory. The trajectories represent a given family of exchanged resonances in scattering theory. $\alpha(t)$ is defined such that the t_σ value, corresponding to $\sigma = \alpha(t_\sigma)$, defines the mass squared of a particle with spin σ. A Regge trajectory is called a Reggeon.

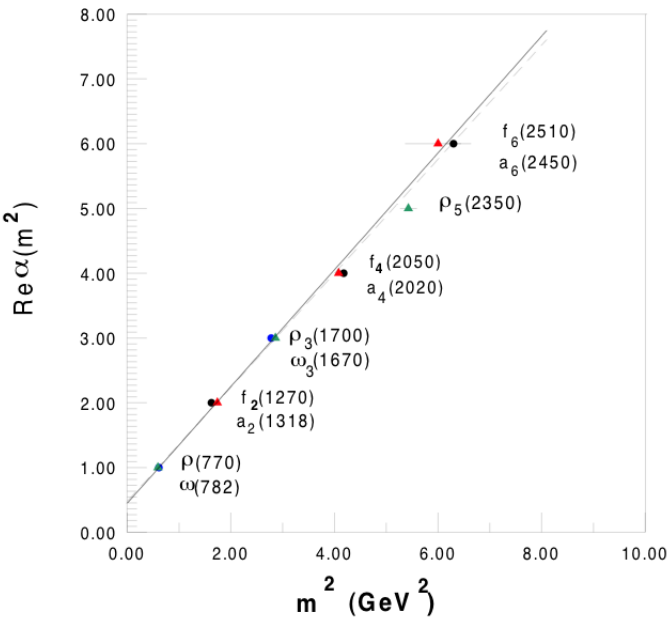

Figure 4.3: The four leading mesonic Reggons, f, a, ρ and ω. They are superimposed onto each other. Also shown is a fit line to the meson distribution. [38].

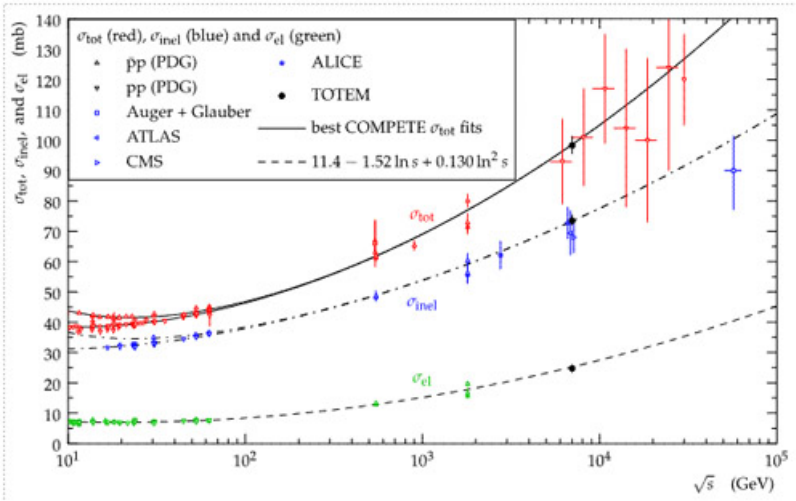

Figure 4.4: The dependance of the cross section on s. [39].

A way to more intuitively understand the Reggeons is to expand $\alpha(t)$ around $t = 0$. For small t, it is sufficient to write

$$\alpha(t) = \alpha(0) + \alpha' t \quad , \tag{4.21}$$

where $\alpha(0)$ is the intercept and α' is the slope. It turns out that this expansion, when considering resonances from a particular family, holds for larger values of t as well. An example of four mesonic Reggeons can be seen in figure 4.3. The resonance families shown in the figure all carry the same quantum numbers, apart from spin. Note that the intercept is ≈ 0.5, this means that the contributions does not violate the Froissart-Martin bound on the total cross section. An intercept above 1 is required before this happens.
Consider now the relation between the total cross section and the elastic scattering amplitude described by equation 4.16. For large s, $|p_1|$ becomes $\sim \sqrt{s}/2$, and therefore the total cross section becomes

$$\sigma^{\text{Tot}}(s) \sim s^{-1} \text{Im} A(s, t = 0) \quad . \tag{4.22}$$

Because $t = 0$, the amplitude is $A(s, t = 0) \sim f(t) s^{\alpha(0)}$ this leads to a total cross section dependence of

$$\sim s^{\alpha(0)-1} \quad . \tag{4.23}$$

From figure 4.3 it is seen that $\alpha(0) \sim 0.5$, and thus the dependence is roughly $1/\sqrt{s}$ for each Reggeon. However, measurements of the total cross section, see figure 4.4, initially decreases as a function of s, and then, at ~ 20 GeV,

it rises. This rise does not follow $1/\sqrt{s}$. This is the reason for introducing the Pomeron in addition to the mesonic Reggeon of figure 4.3. All these Reggeons then add to the total cross section as

$$\sigma^{\text{Tot}} \sim \sum_i A_i s^{\alpha_i(0)-1} \quad , \tag{4.24}$$

where the sum is over the different possible Reggeon exchanges.

4.2 The Pomeron

The Pomeron has, unlike the mesonic Reggeons, an intercept of $\alpha(0)$ just above 1. This intercept is expected because it will explain the rise in cross section as a function of s. A simple fit to the cross section as a function of energy yields

$$\sigma^{\text{Tot}} = Xs^{0.0808} + Ys^{-0.4525} \quad , \tag{4.25}$$

where X and Y are reaction dependent constants. Remembering equation 4.23, the first power of s can be indentified with a Pomeron exchange with an intercept $\alpha(0) = 1.0808$, and the second power can be identified with a mesonic exchange with an intercept of $\alpha(0) = 0.5475$. However this will violate the Froissart-Martin bound. There exists some ways out of this dilemma, one is simply the argument that, at present energies s is still far from the limit, and thus new physics could possibly kick in to stop the growth of the cross section. Another way around the dilemma is to introduce cut singularities which counter-act the contributions from the Pomeron by exchanging two or more Regge trajectories. However, more insight in the Pomeron is needed.

The Pomeron is not expected to be a particle based on quarks, like the mesons, or maybe even a particle at all. It is currently thought of as a glueball, a complicated exchange of two or more gluons simultaneously. It is thought to be the dominating trajectory in elastic and diffractive interactions, and therefore thought to have the quantum numbers of the vacuum. To describe it in the full framework of pertubative QCD is rather complicated, and that will not be discussed here. However an earlier and more introductionary example of the Pomeron in QCD will be introduced along with some of the results of the full description.
The simplest field theory for Regge poles is a massive ϕ^3 theory with coupling constant g. In this theory the Regge pole is described by the exchange of a ladder of bosons. The tree level diagram, shown in figure 4.5a, will give an

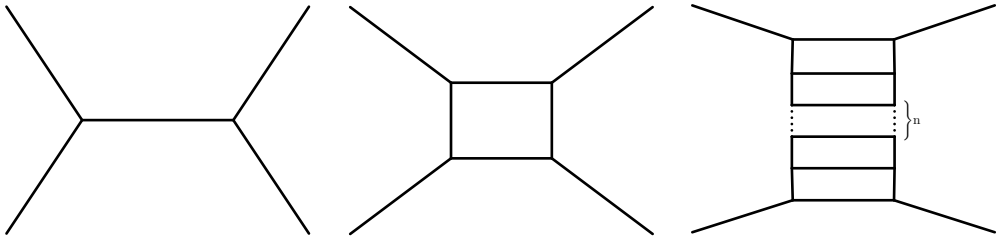

(a) (b) (c)

Figure 4.5: (a) A ladder diagram with 1 step. (b) Two step ladder diagram. (c) n step ladder diagram

amplitude of, in the limit $s \to \infty$,

$$A^{(1)} \underset{s\to\infty}{\sim} \frac{g^2}{s} \quad , \tag{4.26}$$

where the superscript on A denotes the number of steps in the ladder. The second order, see figure 4.5b, is a box diagram, and, in the limit $s \to \infty$ and fixed t, the amplitude is

$$\begin{aligned} A^{(2)} &\underset{s\to\infty}{\sim} \frac{g^2}{s} K(t) \ln s \quad , \\ K(t) &\sim g^2 \int \frac{\mathrm{d}^2\mathbf{k}_t}{(\mathbf{k}_t^2 + m^2)[(\mathbf{k}_t + \mathbf{q}_t)^2 + m^2]} \quad , \end{aligned} \tag{4.27}$$

where $t \equiv q^2 \approx -\mathbf{q}_t^2$. This can be continued to the n step ladder shown in figure 4.5c, and the result is, for $s \to \infty$ and fixed t,

$$A^{(n)} \underset{s\to\infty}{\sim} \frac{g^2}{s} \frac{(K(t)\ln s)^{n-1}}{(n-1)!} \quad . \tag{4.28}$$

The total amplitude is then a sum of all the ladder diagrams, from the one-step to the infinity step,

$$\begin{aligned} A(s,t) = \sum_{n=1}^{\infty} A^{(n)} &\sim \frac{g^2}{s} \sum_{n=1}^{\infty} \frac{(K(t)\ln s)^{n-1}}{(n-1)!} \\ &\sim \frac{g^2}{s} \mathrm{e}^{K(t)\ln s} \sim g^2 \mathrm{e}^{\alpha(t)} \quad , \end{aligned} \tag{4.29}$$

with $\alpha(t) = K(t) - 1$.
Thus, the amplitude is found to have the same exponential behaviour as a Reggeon. Therefore a Regge pole can be described by an infinite sum of

powers of $\ln s$. This is for the unphysical ϕ^3 theory, but the idea continues to pertubative QCD and Regge poles. In QCD the Regge pole amplitude is essentially found to be, in the high s limit, a sum of $\ln s$ powers and originate from a gluon ladder exchange.
The QCD theoretical framework of the Regge pole formalism is far from complete. Nonetheless, the Pomeron exchange model is used for diffractive scattering as these events occur at a regime of extreme small angle scattering where pertubative calculations are presently too difficult.

4.3 Summary

As the theory needed for understanding the kinematics and signatures of diffractive events has been developed, the next step is to discuss how to detect them using a particle accelerator.

Diffractive events occur mostly at low momentum transfer in the t channel, i.e. the proton and diffractive system continue along the initial particles paths, and therefore forward detectors and a high η coverage is of the utmost importance. In addition to this, it is also required that it is possible to detect rapidity gaps to ensure that the exchange was colourless.
The detector system chosen is the ATLAS detector, for detecting the diffractive mass systems, and ALFA, for detecting the diffractively scattered protons. ATLAS because it is a detector designed for all around physics and provides high accuracy tracking and η coverage. ALFA is chosen because it is designed to detect protons at very low scattering angles, and it is placed far from the interaction point, therefore offering a high η coverage region of detection. In section 5, 6 and 7 the detectors are described in detail.

Part II
The Detectors

5 The Large Hadron Collider

In this section an overview of the detector system at the LHC will be presented, as it was used in the collection of the data analysed in this thesis. This section is based on ref. [6], [7], [8], [9] and [10].

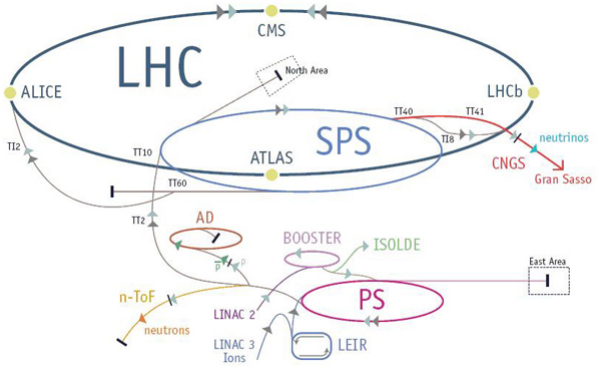

Figure 5.1: The LHC accelerator system. [40].

Outside of Geneva, beneath the French-Swiss border, lies the LHC (Large Hadron Collider). It is a large system of accelerators and detectors designed to accelerate particles and collide them at certain interaction points (IP) where detectors are located. The LHC is buried underground, at a depth of 50 to 175 meters, in a ring with a circumference of 27 km. For an overview of the LHC detector system, see figure 5.1.
The LHC system collides beams of particles, typically protons but occasionally also heavy ions. The beams are accelerated through a number of smaller accelerators before finally being injected into the LHC where they are circulated in both directions in two vacuum beam pipes lying next to eachother. To keep the two beams moving in a circular motion, 1232 dipole magnets are used to bend the beams. They are based on NbTi (nNiobium-Titanium), which is superconducting at 10K, and they are designed to operate at 1.9 K with a current of 11700 A which will yield a magnetic field of 8.33 T. When the beams reach a detector the beams no longer travel in separate beampipes, but they are brought to collision in the center of the detector.

Since the colliding particles are very small, getting them to collide is very difficult, and this is the reason for colliding large bunches of particles. After a collision point, the protons that did not collide will again continue down the two separate beam pipes. There are four of these collision points, one at each of the main detectors at the LHC. The four main detectors are ALICE, LHCb, CMS and ATLAS.
The purpose of ALICE (A Large Ion Collider Experiment) is to study heavy ion collisions, such as proton-lead and lead-lead collisions. In these types of collisions the temperature and energy density is expected to be high enough to generate a quark-gluon plasma, i.e. a state where gluons and quarks are no longer colour confined.
LHCb (LHC beauty) is designed to study b physics. This includes measuring CP-violation in B meson decays which is hoped to give insight into the matter-antimatter asymmetry of the universe. In addition, LHCb will determine cross sections of electroweak interactions in the forward region.
The CMS (Compact Muon Solenoid) detector is one of the two general purpose detectors at the LHC, the other being ATLAS. The aim is to study a wide range of physics topics such as the Higgs boson, dark matter candidates and extra dimensions.
The last detector, ATLAS, is the detector used in this thesis and it will be described in detail in section 6.

5.1 The LHC Beam

The collisions at the LHC are produced by colliding beams of protons at certain points, thus creating the events studied later. This section will describe the beams at the LHC, and this includes the luminosity, bunches and the optics

The LHC beam consists of, at full intensity, 2808 bunches of 1.15×10^{11} protons. In the transverse direction, the beam is roughly the size of a millimetre. However at the collision points it is squeezed to about 16 μm. The bunches are separated by roughly 25 ns and travel at 0.999999991 c. Even with these numbers, most protons miss each other and continue along the beam pipe.
The luminosity at the LHC can be defined by

$$L = \frac{fN_1N_2}{4\pi A} = \frac{fN_1N_2}{4\pi\sigma_x\sigma_y} \quad , \tag{5.1}$$

where N_n is the number of protons in bunch n, f is the frequency between bunch crossings and A is the cross sectional area of the bunches. The last

equal sign is valid when assuming a gaussian profile of the bunches, and σ_x and σ_y denote the gaussian widths of the bunches in the transverse plane.
The total luminosity is determined from the instantaneous luminosity summed over a series of small steps in time, $\Delta\tau$. These steps are called lumi blocks (LB), and they are defined as the shortest amount of time that the instantaneous luminosity can be determined. A LB size is of the order of a few minutes. In a LB it is required that there is a roughly constant dead time and instantaneous luminosity, where dead time is the length of time needed between events for the detector parts to be able to measure again. Each lumi block is assigned a unique number, called the lumi block number (LBN), to be able to identify them in the analysis.

At the collision points, the beams are squeezed to increase the probability of an interaction. When the beams are squeezed, the width, σ_t, of the distribution is decreased. The squeezing can be done at different levels depending on the luminosity wanted. The variable used to describe the squeezing is β^*. β^* is defined as the distance between the interaction point and the the point where σ_t of the beam is twice as large as at the interaction point, see figure 5.2.

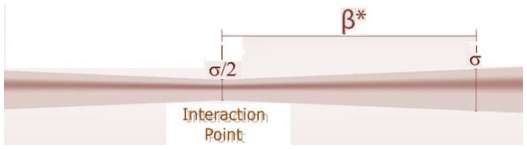

Figure 5.2: A figure showing the definition of β^*. [41].

The squeezing is done using magnetic lenses, and this gives, at standard LHC options, a squeezing of $\sigma_x = \sigma_y = 16$ μm. This, when considering the length of a bunch, leads to a volume much greater than the volume of an atom, meaning collisions are still rare. When a collision does occur, and the triggers deem it interesting enough to store, it is assigned a bunch crossing ID (BCID) used to indentify the collision in data analysis.
The value of β^* is often referred to as the optics. The standard LHC optic is $\beta^* = 0.65$ m, however special dedicated runs have $\beta^* = 90$ m optics.
In order to protect the magnets guiding the beam around the LHC, beam screens are used. They are cylindrical and placed inside the magnets, screening them from the beam. The purpose is to shield the magnets from synchrotron radiation emitted from the beam, which corresponds roughly to 0.22 W/m. For more informaton on the beamscreen, see ref. [11].

6 The ATLAS Detector

The ATLAS (A Toroidal LHC Apparatus) detector system consists of the main detector and several smaller ones distributed along the beampipe up to ± 240 meters. These smaller detectors are (in order of closeness to the ATLAS main detector) LUCID, ZDC and ALFA. The ATLAS main detector is 45 meters long, and it has a diameter of roughly 25 meters. Its weight is around 7000 tons. This is the detector, along with ALFA, used to collect the data used in this thesis, and therefore this section is dedicated to a detailed description of ATLAS. It is based mainly on ref. [12], [13] and [14].
The ATLAS detector is a cylindrical detector. Innermost in the detector, where the particles collide, is the inner detector and solenoid magnets. Surrounding this is the electromagnetic and hadronic calorimeter. Further out are the toroidal magnets and the muon detectors. A complete overview is shown in figure 6.1.

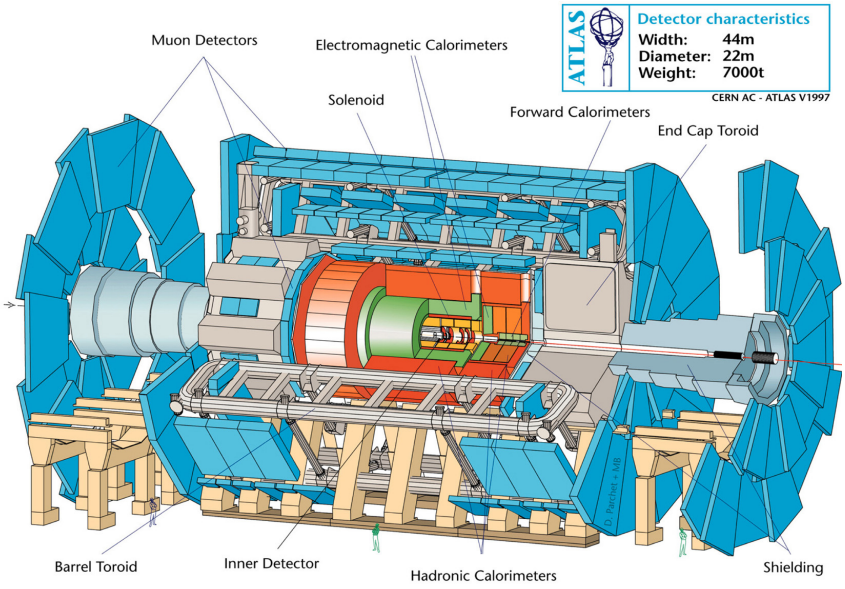

Figure 6.1: The ATLAS main detector, showing the inner detector, the electromagnetic and hadronic calorimeters, the magnets and the muon detector. [43].

It is this system of detectors that allow detection and identification of particles because of the different signatures left by different particles. Figure 6.2 gives an overview on how this is done. A more detailed explanation on how the parts work will follow in the next subsections.

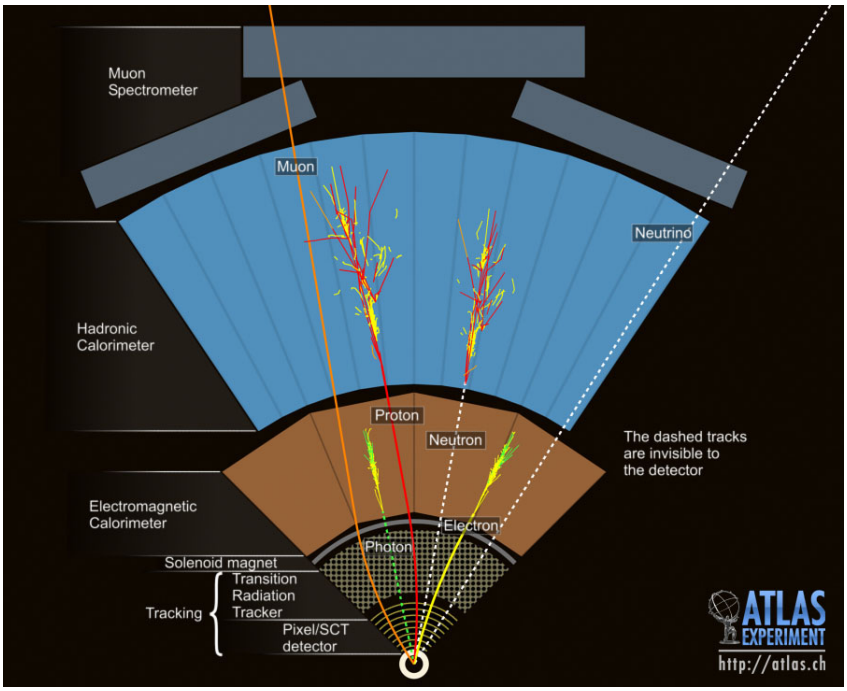

Figure 6.2: An illustration on how the ATLAS detector identify different particles. [44].

6.1 The Magnet System

A magnetic field is used in the ATLAS detection system to bend charged particles. The particles produced at the LHC collisions are all relativistic, i.e. travelling with almost the speed of light. A charged particle moving in a magnetic field will bend in a circular motion, in the plane perpendicular to the field. Therefore the particles will bend inside the inner detector, and high momentum particles will bend very little while low momentum particles bend more. The bending can be measured, and thus the particle momentum can be determined. In addition, the direction in which the bending occurs determines the charge of the particle. A complete overview of the magnets of the ATLAS detector can be seen in figure 6.3.

6.1.1 The Soleniod Magnet

The magnet system in the ATLAS detector consists of two parts. First, there is the inner magnet. It is a solenoid magnet providing the magnet field used in tracking system of the inner detector. It has a 2 Tesla magnetic field which gives rise to the curvature of the charged particles in the inner detector. The strength of the magnetic field is such that particles with momenta below

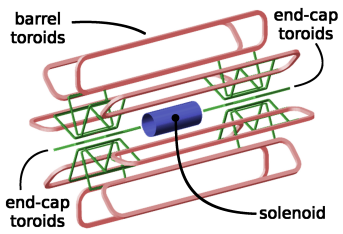

Figure 6.3: An overview of the magnets of the ATLAS detector. [45]

about 400 MeV will be curved to a degree where the particle is likely to not make it out of the inner detector and will not be measured elsewhere in ATLAS. This magnetic field is almost uniform in strength and direction which gives accurate measurements in the inner detector.

6.1.2 The Toroidal Magnet

Outside the calorimeters, but within the muon detection system, is the second magnet system. This outer toroidal magnet system consists of two parts, the two end-cap air toroidal magnets and the eight air-core superconductiong barrel loops. The purpose of this magnet system is to bend the muons when they travel through the muon detector. This field is not uniform, but its strength varies between 2 and 8 Tesla-meters, and it covers an area 26 meters long and 20 meters in diameter. The toroidal magnet will provide bending of muons in the range of up to 2.7 in pseudorapidity.

6.2 The Inner Detector

The inner detector, ranging from a few centimeters from the beam to about 1.2 meters, is mainly used to track charged particles. When the particles move through the detector and interact with the material at a finite number of points, it is possible to reconstruct a track. The inner detector is also used to determine impact parameter and vertex position. The inner detector itself consists of three parts, the pixel detector, the semi-conductor tracker (SCT) and the transition radiation tracker (TRT). In the central region these three parts are setup in a barrel detector around the interaction region. In the forward part, the detector consists of concentric circular disks around the beam. See figure 6.4 for an overview. The inner detector system covers tracks with $|\eta| < 2.5$.

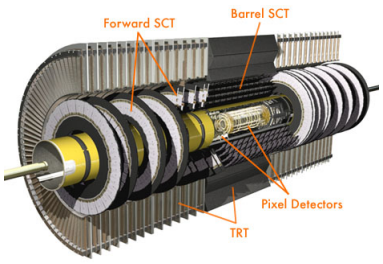

Figure 6.4: The inner detector of ATLAS. [46].

6.2.1 The Pixel Detector

The pixel detector is a silicon detector, and it consists of 1744 modules, all of them measuring 2×6 centimeters and have a thickness of 250 μm. The modules are distributed between the central part (1456 modules) and the forward region (288). Each module have 16 readout chips, and these chips are able read out a pixel of size 50 by 400 μm. It is designed to give extremely accurate tracking measurements as close to the interaction point as possible. Because of its closeness to the interaction point it is also exposed to a huge amount of radiation, and therefore it needs radiation hard components.

6.2.2 The Semi-Conductor Tracker

After the pixel detector is the SCT. Its pupose is the same, to provide tracking of the particles produced, however to do so with a larger coverage than the pixel detector. It does this in the same way as the pixel detector, by using readout chips. The SCTs chips are longer and more narrow which makes coverage of larger areas simpler. These strips measure 80μm $\times$12 cm, and they are placed in four double layers. It is designed to give eight precision measurements contributing to the overall measurement of momentum, impact parameter and vertex position. The SCT gives the most accurate tracking of particles in the plane perpendicular to the beam.

6.2.3 The Transition Radiation Tracker

The last component of the inner detector is the TRT. This part of the detector consists of straw trackers, each straw being 4 mm in diameter and up to 144 centimeters long. Each of these straws are filled with a gas mixture, of Xe and CO_2 with a small admixture of O_2, that becomes ionised when a charged particle passes through. By constantly applying an electric field of -1500 V on each of the straw one ensures that all the electrons from ionisation drift to a wire going down the center of the straw and cause this wire

to produce a current signal. By measuring the drift time of the electrons and combining these signals from several wires, a track is reconstructed. The resolution of the track measurement is around 130 μm, and hence it is not as great as the other two parts of the inner detector. However in order to cover a larger volume and provide transition radiation tracking, this was necessary. Between the straws is material of varying refractive indices, and this causes transition radiation of extremely relativistic particles which leaves stronger signals in some straws.

The inner detector is used to distinguish charged particles such as electrons, protons and muons from non-charged particles such as neutrons, photons and neutrinos by measuring a track and the bending of this track.

6.3 The Calorimeters

After the inner detector and the solenoid coil lies the calorimters which consists of two parts, an electromagnetic calorimeter and a hadronic calorimter. The purpose of both parts is to measure the energy of the incoming particle. In addition to measuring the energy of the incoming particle, it also determines the pseudorapidity and the azimuthal angle.
The electromagnetic calorimeter absorbs all the energy from particles that interact electromagnetically while the hadronic calorimeter absorbs the energy of particles that interact via the strong force, i.e. only particles consisting of quarks and gluons, the hadrons. The electromagnetic calorimeter consists of a barrel component (EMB), two end-caps (EMEC) on either side and the forward calorimeter (FCAL). The hadronic calorimeter consists of the Tile calorimeter and the hadronic endcaps (HEC). It is assembled such that the EMB is the innermost barrel shaped detector with the Tile calorimeter positioned just outside. In the forward direction, there is the end cap and the FCAL. The end cap is assembled in the same order as the barrel, with the EMEC being the innermost detector immediately followed by the HEC. The FCAL is then positioned further outside the endcaps. The barrel region has an η coverage of $|\eta| < 2.5$, the endcaps cover $1.375 < |\eta| < 3.2$ and the FCAL covers an η region of $3.1 < |\eta| < 4.9$.
The calorimeter system supplies two different methods for detecting particles. The first being the liquid argon calorimeters. This method is used in all the electromagnetic components as well as the HEC. These are build of layers of lead (steel in the hadronic case) which is used as absorbtion material. Between these layers is the liquid argon. When an incoming particle hits the first absorbtion layer it creates a shower of particles which will then ionise the liquid argon. These then hit the next layer to create even more particles,

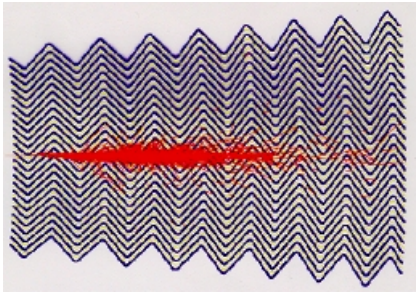

Figure 6.5: A shower created in the calorimeter due to an incoming particle. [47].

and this continues until there is no more energy left to create more particles. Thus a shower of particles are created. The absorbtion layers are made in a zig-zag shape to increase the resolution. The total ionisation charge is proportional to the energy loss of the incoming particle and is read out, see figure 6.5.
The build-up for the hadronic tile calorimeter is the same as the electromagnetic one, except it uses scintillation tiles as detection material and iron as the absorbtion material. These are coupled to optical fibers and the readout is done via photomultipliers.

6.4 The Muon Spectrometer

The muon spectrometer is the largest component of the ATLAS detector. The reason for this is that muon is the only charged particle that is able to travel through the calorimeters without being stopped. The purpose is basically the same as the inner detector, tracking, momentum determination of the muons and simply identification of a muon. It consists of two parts, a forward region and the central region, to cover larger η regions while keeping the barrel shape of the ATLAS detector. The magnetic field is supplied by the toroidal magnets. It is designed to work as a standalone detector, meaning it has its own separate triggers and detection system.
The muon spectrometer is a straw detector, similarly to the TRT of the inner detector. The detector has both forward detection regions as well as a central detector. It consists of 1200 chambers, which gives a high spatial resolution of the tracks as well as triggering chambers to provide precise time-resolution.

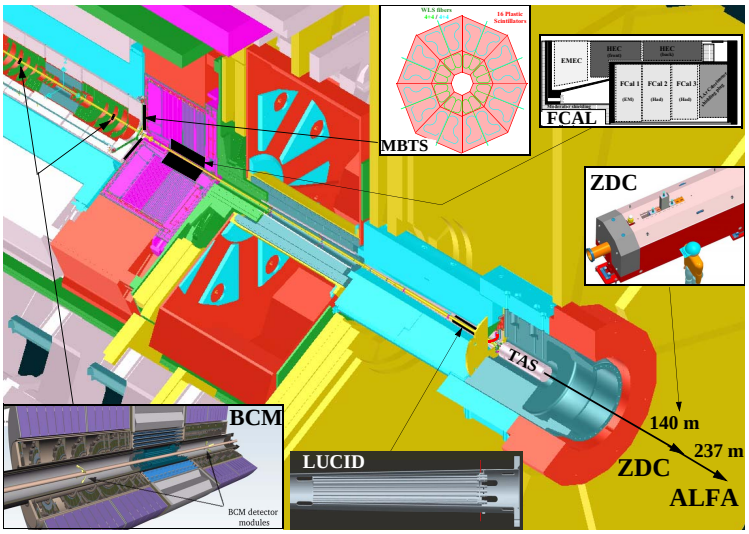

Figure 6.6: The forward detectors of ATLAS. These include the MBTS, the FCAL and LUCID. [48].

6.5 The MBTS

The Minimum Bias Trigger Scintillator (MBTS) is located just outside the inner detector in the forward region, and its purpose is to provide information for a minimum bias trigger. Because of this, it is also a relatively simple detector. It is made up of 32 scintillating plates, 16 on either side of the inner detector. It is located 3.5 m from the center of ATLAS. An overview of the forward detectors of ATLAS can be seen in figure 6.6. The MBTS is, on both sides, split into two rings of 8 as can be seen in figure 6.6. Each of these 8 segments covers a range of $2\pi/8$ in the azimuthal direction. It covers an η region of 2.09 to 3.84. The scintillators emit light when hit, and that light is guided via wavelength shifting optical fibers to a photomultiplier tube. Because of the simpleness of the MBTS detector, it does not give any information as to the η, $\mathbf{p}_T$ or ϕ of the particle. One only knows which segment of the detector was hit and how much energy was deposited in that sector. Therefore, when considering the number of hits in the MBTS, it refers to the number of segment plates hit. Based on this, when a certain number of sectors are hit above some threshold value the triggers are configured accordingly.

6.6 LUCID

The LUCID detector consists of 16 tubes, on both sides of ATLAS, made of aluminium and filled with the gas C_4 F_{10}. These tubes are located at ± 17 m, have a length of 1.5 m and a diameter of 15 mm. The tubes are oriented towards ATLAS. Its purpose is to measure the luminosity in ATLAS.
When a charged particle hits one of the tubes, Cerenkov photons are created in the gas. These photons are reflected down the walls of the tube where a photomultiplier collects the data. As with the MBTS detector, LUCID collects number of particle hits only, and it covers an η range of 5.6 to 5.9.

6.7 Triggers

The amount of information being produced every second at the LHC is enormous, and therefore a way to quickly sort through all the data has been devised. By doing this, only the events deemed interesting will be saved for analysis, and that greatly reduces the huge amount of data.
The trigger selection is done on several levels. The first, the level 1 trigger (L1), usually makes a decision based on information from the calorimeters and the muon detectors only. The L1 trigger requires around 2 μs to reach a decision. This includes the propagation of the cables from the detector to the trigger logic software. The information from the detector is stored in pipeline memories while the L1 trigger makes its decision.
The L1 trigger is still a very rough calculation in most cases. Therefore a level 2 trigger (L2) is also used. For events triggered by the L1 trigger, the L2 trigger does further analysis while the data is temporaily stored in readout buffers. The L2 trigger conducts a full analysis using both inner detector, calorimeters and muon detector parts, but only based on regions of interest determined by the L1 trigger.
In case of a positive L2 result, the event data is checked against a third trigger level, the event filter. Here, an analysis similar to that of the offline level is done.

7 The ALFA Detector

The ALFA (Absolute Luminosity For ATLAS) detector consists of four stations, two on each side of the ATLAS detector. They measure protons that have deviated from the beam due to interactions in ATLAS. The main purpose is to measure the absolute luminosity and cross section for ATLAS by using elastic events. In this thesis it will be used to identify diffractive events. This is due to the high pseudo-rapidities accepted by the detector. This section is mainly based on ref. [15].

7.1 The ALFA Setup

The four stations are located, symmetrically, on either side of the interaction point (IP) in ATLAS. The inner stations are positioned at ±237.398 m and the outer at ±241.538 m. See figure 7.1 for an overview of the forward detectors of ATLAS.

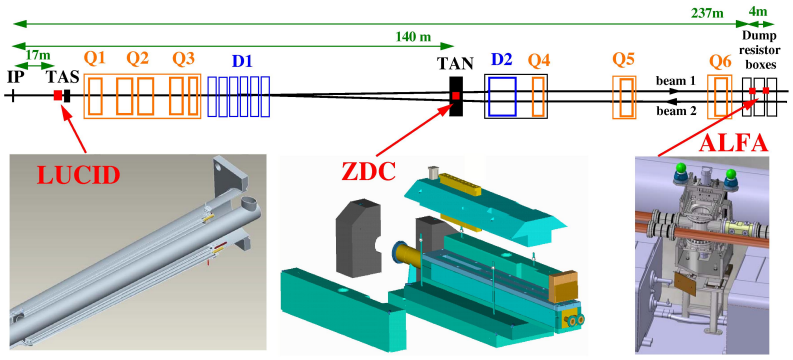

Figure 7.1: The forward detectors on one side of ATLAS. The position of LUCID and ZDC are also included as well as the magnets along the beampipe (Q for quadrupole and D for dipole). [49].

The detector is shown in figure 7.2. The actual detector is the green diamond shape shown in the figure. In addition, the roman pots are shown as well as the electronics used to read out the signals. Details on the components follow later.
As shown in figure 7.1, the ALFA detectors are located after the beam is split into the two seperate pipes used for the majority of the accelerater. The detector stations are located at the beampipe containing the outgoing particles. Due to the LHC beam not being in the same location for all runs, the ALFA detection system uses movable roman pots as detectors. For each

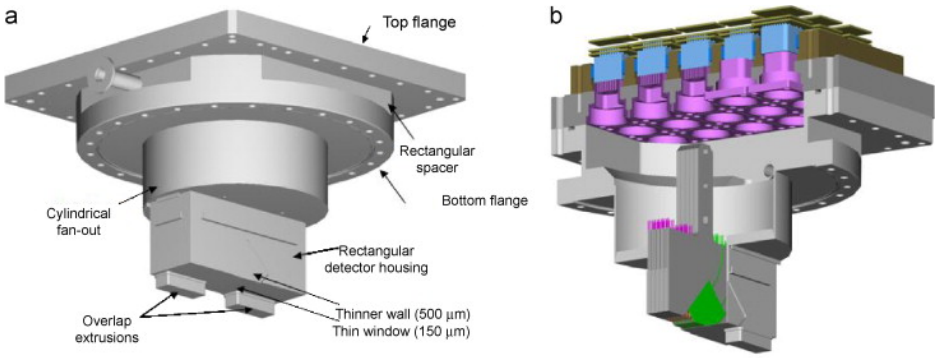

Figure 7.2: A figure showing the upper part of one of the ALFA stations. On the left, the roman pot is shown while, on the right, the inside of the detector is shown. The latter includes the electronics and the actual detecter (in green). [50].

run the detectors are moved in towards the beam until the beam halo is seen in the detector. The beam halo are particles created by inelastic and elastic collisions between the beam and left-over gas particles of the LHC vacuum and inefficiency of the beam cleaning (Ref. [29]). To avoid detection of beam particles, the detectors are then moved back again until they are positioned a satisfactory number of sigmas away from the beam. Sigma, here, refers to the statistical width of the bunches.
Since the ALFA detector is split into an upper and lower part, some form of alignment must be used to ensure the two roman pots are in a symmetric position around the beam. This is done using overlap detectors, and they are described later. They are rectangular detectors positioned on either side of the main ALFA detector on both the upper and lower part, i.e. four in total per station. They measure 6×15 mm and are installed with a fixed distance to the main ALFA detector. They are positioned such that the top of one overlaps the bottom of the other. This allows the same proton to be seen by both detectors, and therefore the overlap detector can be used to align the two main ALFA detectors to each other, see ref. [16]. A hitmap of the ALFA detector is shown in figure 7.3. There are eight detectors in total distributed over 4 stations, as can be seen in figure 7.4.

7.2 Detection of Protons

In the LHC beam pipes there is a very high vacuum, and therefore, to move the ALFA detector close to the beam, Roman Pots are used. A Roman Pot is a device which allows the ALFA detector to approach the beam in a separate,

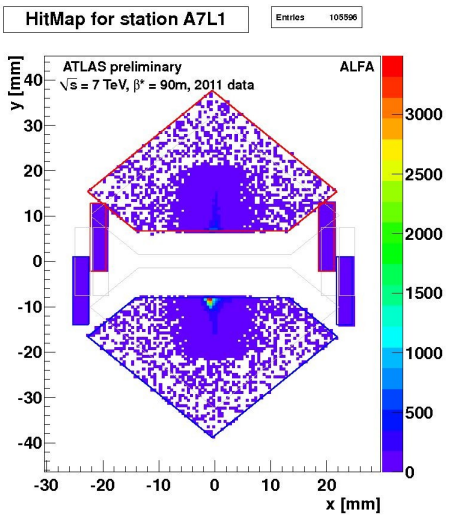

Figure 7.3: The hitmap of one of the ALFA stations. The overlap detectors are shown as well, however they are slightly misplaced to show both of them in their entirety. [51].

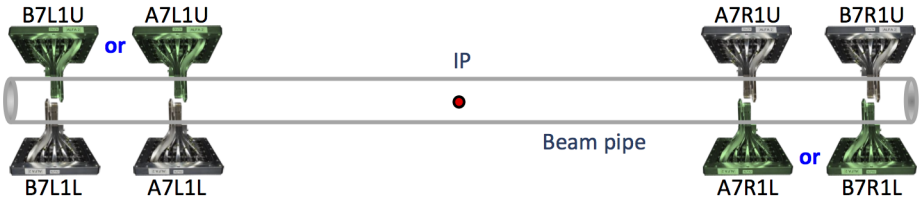

Figure 7.4: The names of the 8 ALFA station. A7 and B7 refers to inner/outer detectors, L1 and R1 refers to the left/right side of ATLAS and U and L refers to an upper/lower position around the beam. The stations highlighed in green shows the trigger logic of the `L1_ALFA_ELAS15`. [56].

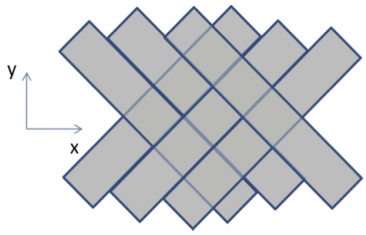

Figure 7.5: The pattern in which the fibers are placed in one layer. [52].

secondary vacuum, see figure 7.2. Because of these two separate vacua, the ALFA detector, located inside the roman pot, is separated from the LHC vacuum by a thin wall as seen on figure 7.2. This wall has a thickness of 200 μm. Due to the thinness and the LHC vacuum, this area is subject to a large pressure, and the wall would bend were it not for the vacuum inside the roman pot. The vacuum does not have to be as good as the LHC vacuum, but good enough that the wall does not bend.
To detect incoming particles, the detector uses scintillating fibers. These are squared wires which, when hit by a particle, transports light down the wire where they are read out using photomultipliers. To do this they are coated with aluminium which totally reflects light hence ensuring the photons are trapped inside one fiber. Since the fibers are only read out in one end, they are also coated in the other end to ensure no light is lost at that end. Each fiber measures 5×5 mm.
The fibers offers no means of detecting where on the fiber there was a hit, and therefore they are arranged in a pattern where an incoming particle hits more than one fiber, and hence the hit was where these two fibers intersect. This creates the pixels that the ALFA detector detects particles with. The pixels created measure 500 μm on each side and 707 μm on the diagonal. The pattern is show in figure 7.5. To give a better resolution, a total of 10 layers are used. Each layer is shifted by 1/10 of the width of the fibers. This shift, combined with ten layers, gives a final resolution of $\sim$30 μm.
The fibers are attached to a titanium wedge placed inside the roman pots. See figure 7.6 for an overview. The figure also shows how some of the fibers are cut of to obatin the diamond shape of the main ALFA detector.
Scintillating fibers are also used for detection in the overlap detector. Here only three layers are used as it is not important to know exactly where the detector is. What is important to know is the relative postion of the upper and lower detectors. This is the purpose of the alignment and overlap detectors, and it is done by using particles from the beam halo that passes through both of the overlap detectors. Because the upper and lower main detector and their corresponding overlap detectors are at a fixed distance,

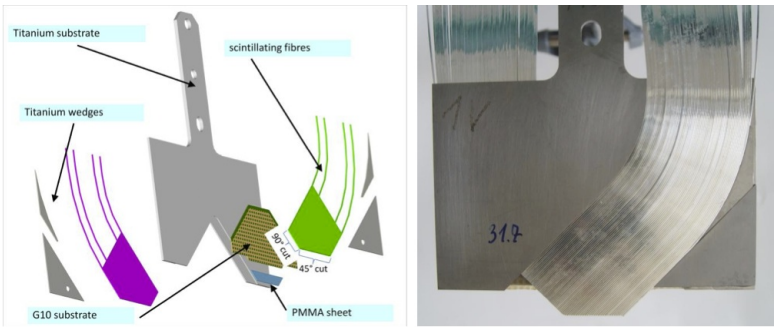

Figure 7.6: An overview of how the scintillating fibers are mounted on the wedge. [53].

a hit in like this gives the relative position of the upper and lower main detectors.

7.3 Event Signatures in ALFA

The main purpose of the ALFA detector is to measure the absolute luminosity of ATLAS. This is done using elastic events. At small values of the momentum transfer, t, the electromagnetic interactions becomes dominant to the strong force. This change can be measured in the elastic cross section, and, since the Coulomb interaction is theoretically completely known, the luminosity can be determined. At these t values however, a very small scattering angle is required, roughly of the order $\sim$3.5 μrad. This is the reason for ALFAs position at roughly $\pm$ 240 m.
However, this position causes some trouble with the proton transportation down the beam pipe. Between ATLAS and ALFA there are six quadropole and two dipole magnets, as shown in figure 7.1. These are designed to keep the beam in place, and hence they affect the elastic or diffractively scattered protons. This is of course undesired for ALFA, and, to account for possible effects, a detailed simulation of protons travelling down the beam pipe with different energies and momenta has been done. For the standard optics, $\beta^* = 0.65$ m, the result of the transportation can be seen in figure 7.7a. Figure 7.7a shows that, for $\beta^* = 0.65$ m, elastic events will not reach ALFA. Elastic events are events with $\Delta E = 0$, and displayed as the empty and filled circles. Protons with an energy loss, filled and empty squares, can be seen leaving a signal that, for a fixed energy loss, spreads over large values of x. Since a precise x measurement is need to estimate the energy loss of a diffractively scattered proton, this is not ideal. Correspondingly, figure 7.7b shows the hitmap for $\beta^* = 90$ m optics. Here it is seen that elastic events,

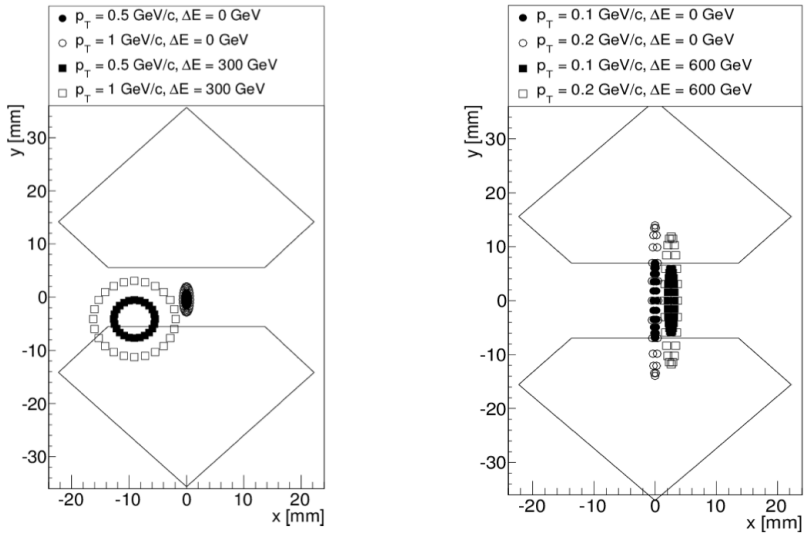

(a) (b)

Figure 7.7: The efftect of the transport from the interaction point to ALFA given the optics. The effect is shown for different energy losses, momenta of the proton and azimuthal angle (the 24 points). (a) shows the effect for $\beta^* = 0.65$ m, and (b) is for $\beta^* = 90$ m. [54].

empty and filled rings, leave a signal in ALFA at the center of the detector with little spread. Likewise, a proton with an energy loss, empty and filled squares, leave a signal of the same form but with a shifted x value.

8 Detector Summary

As the theory and detectors have been described, it is time to consider how these two combine and what one would naively expect to see in the detectors, when studying diffractive events.

To describe the variables of a collision, the coordinate system used has to be defined. The LHC coordinate system is defined such that the z axis follows the proton beam moving in the counter clockwise direction. Even though the beam is moving in a circle at the LHC, the circle is large enough that the z direction can approximately be taken as the beam direction in the ATLAS system. The xy plane is then the plane perpendicular to the z axis, where $(x, y) = (0, 0)$ is at the z axis, i.e. the proton beam. The x axis is defined to be horizontal and positive towards the center of the LHC ring, while the y axis is vertical and positive in the upwards direction.

For the forward detectors, one usually uses A and C side, where the A side of ATLAS is the positive z direction while C is the negative. This also means that the A side refers to positive η while the opposite is true for the C side.

In this thesis, ATLAS and ALFA will be used in unison to identify and measure the properties of diffractive events. To identify diffractive events, the idea is to use ALFA to tag the proton while requiring activity in ATLAS. This should exclude elastic events as well as most non-diffractive events. When the selection has been done, the next step is to analyse the properties of diffractive events, such as the energy loss of the diffractive protons and rapidity gap distribution in ATLAS.
As the idea behind this thesis is to use tagged protons in the identification of diffractive events, the focus will be on SD and CD events as DD events leave no proton to tag. The expected signature of a single diffractive event is, in ALFA, hits that move towards positive x values for higher energy losses of the proton, see figure 7.7b. In ATLAS, the expectation is a rapidity gap in η, from the proton side to the first track in ATLAS.
The expected CD signature is a proton tagged on either side of ATLAS, where the kinematics are the same as for SD protons. In ATLAS, a rapidity gap is also expected, however due to the Pomeron collision involved in CD events the gap will be different from SD events. The activity should be centered around $\eta = 0$, depending on the energy loss of the protons, with gaps to both protons.

Part III
The Analysis

9 Previous Results

Diffractive events and rapidity gaps have been measured before at the LHC with ATLAS, as can be seen in ref. [17]. The focus of that article was to measure rapidity gaps in ATLAS for pp collisions at 7 TeV. This analysis was done for several values of a $\mathbf{p}_{T,\min}$ cut of the tracks and clusters used. The analysis was done using ATLAS only. The result can be seen in figure 9.1 with the $\mathbf{p}_{T,\min} > 200$ MeV cut for calorimeter clusters and inner detector tracks in the region $\eta < |4.9|$.

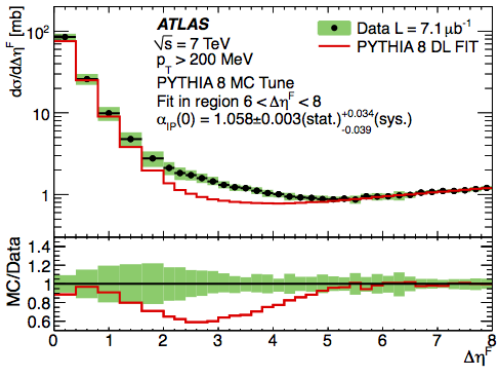

Figure 9.1: The cross section as a function of the forward rapidity gap for $\mathbf{p}_{T,\min} > 200$ MeV. Both data and a Pyhtia 8 simulation is shown as well as a comparison of the two. Also included is a fit value to the Pomeron Regge trajectory at $\alpha_{\mathbb{P}}(t = 0)$. [17], page 16.

The forward rapidity gap was defined by slicing the η region $|\eta| \leq 4.9$ into steps of 0.2. Each track or cluster passing the selection was then put into one of these bins. Then the rapidity gap is, when counting from the A side, defined as the distance in η from the edge, 4.9, to the nearest filled bin. The largest possible gap is from 4.9 to -3.1 due to requirement of a high efficiency trigger in the MBTS acceptance region. The same is done from the C side, and the forward gap, $\Delta\eta_F$, is then the largest of these two gaps. For small gaps, $\Delta\eta_F < 2$, the steps are of the size 0.4 due to the granularity of the FCal. Due to the acceptance limits of ATLAS, the measured forward rapidity gap, $\Delta\eta_F$, will not be the whole gap, but rather $\Delta\eta \approx \Delta\eta_F + 4$, where $\Delta\eta$ is the true gap. +4 because the proton is expected to have a rapidity of

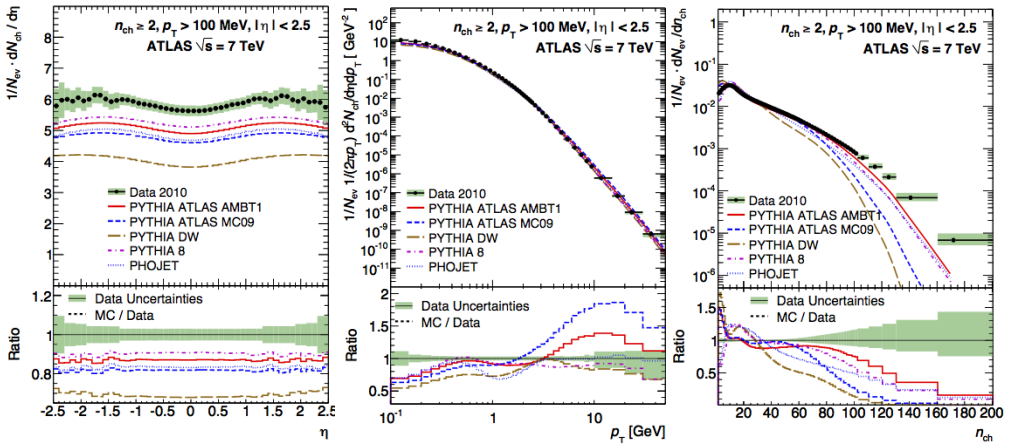

(a) (b) (c)

Figure 9.2: The distributions of (a) η, (b) $\mathbf{p}_T$ and (c) multiplicity for minimum bias events at $\sqrt{s} = 7$ TeV. A cut of $\mathbf{p}_T \geq 100$ MeV has been applied as well as a reuirement of at least two tracks per event. All three plots are also compared to different Monte Carlo samples. [18], page 34, 36, and 38.

$\eta \approx \pm \ln s/m_p^2 \approx \pm 8.9$ which is 4 from the η edge of ATLAS.
Figure 9.1 shows a clear diffractive contribution to the rapidity gap measurements. Recall section 4 where it was argued that a distribution of rapidity gaps due to SD events is roughly constant while it was exponentially supressed for non-diffractive events. A contribution of both types is visible in the figure.
Also included in the plot is the fit result of the Pomeron trajectory intercept, $\alpha_{\mathbb{P}}(t = 0) = 1.058 \pm 0.003(\text{stat})^{+0.034}_{-0.039}(\text{syst})$, which is compatible with the theory (ref. [19]) and other measurements (ref. [20]).

Charged multiplicity studies have also been done at ATLAS for minimum bias events at a collision energy of $\sqrt{s} = 7$ TeV, see ref. [18]. The result of this paper is that, on average, a total of $5.630 \pm 0.003(\text{stat}) \pm 0.169(\text{syst})$ charged particles are created per unit of rapidity. This result is for events with at least two tracks, a track $\mathbf{p}_T \geq 100$ MeV cut and both tracks are required to be within the inner detector acceptance region. This means that the average distance between tracks is very small in minimum bias events which supports the exponential suppression of a rapidity gap, only resulting in large gaps due to statistical fluctuations in the hadronisation process. The track distributions can be seen in figure 9.2.
For diffractive events, it is naively assumed that the track $\mathbf{p}_T$ and multiplic-

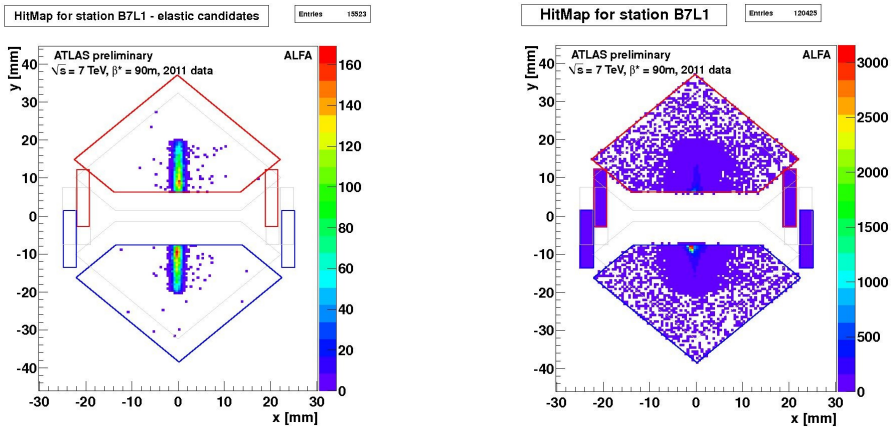

(a) (b)

Figure 9.3: A figure showing (a) the golden elastic events in ALFA and (b) all events in ALFA. The diamond shape is there to display the actual physical ALFA detector, red for upper, blue for lower. The four rectangles, two on either side, display the overlap detector part of ALFA. The chosen ALFA station is B7L1. [51].

ity distributions are similar to those found in figure 9.2. The η distribution, however, is expected to be, for SD events, shifted towards the opposite side of the proton reflecting the rapidity gap of diffractive events. For CD events, it would be expected that the track η distribution is centered around $\eta = 0$ with gaps on either side while the $\mathbf{p}_T$ and multiplicity distributions are similar to minimum bias distributions. However, it is quite possible that the CD event gaps are outside the ATLAS acceptance region in η.
Diffractive events have not previously been measured with ALFA and ATLAS combined. However, there is an ongoing elastic analysis with ALFA. The current results can be seen in figure 9.3a. According to figure 7.7b, elastic events, $\Delta E = 0$, all lie on a vertical line with the length detemined by the $\mathbf{p}_T$ distribution of the elastic protons. The line is in fact an ellipse, however it is a very narrow ellipse. A few events lie outside this region, but the vast majority fits the expected elastic signature.
Diffractive protons, with low energy loss, is expected to leave a similar signal, while for higher energy loss, the line moves towards positive x values, and thus the expected diffractive signal is an elastic like signature with a tail towards positive x which decreases in $|y|_{\max}$. This is expected for both SD and CD protons.
In figure 9.3b, all the hits of ALFA is shown to get a feeling of the general hit pattern in ALFA. The signal region is seen to be dominant.

10 The Data Runs

This section will introduce the data used in the analysis. It will present information on the optics, luminosity blocks (LB) and the triggers of the runs. Information on the runs can be found in ref. [22], [23] and [24]. A list of the data runs used is found in appendix C.

The data runs included in this thesis are special dedicated runs to either elastic or diffractive physics, meaning that the optics have been chosen to be the most optimal in terms of this, $\beta^* = 90$ m. The runs used can be seen in table 10.1. In the run 206881, beam one had 86.7×10^{11} protons, while beam

Data run	Collision energy, $\sqrt{s}$	Bad LBs
191373	7 TeV	1, 2, 4, 26, 31, 34, 39, 53, 74, 75,81, 125, 148, 159, 160, 169, 191, 207, 216, 222, 237, 248, 259, 262 and 263
206881	8 TeV	336, 340, 341, 347, 349 350, 352, 370, 373, 377, 378, 383, 384, 385, 386, 387, 388, 397, 398 and 646
206885	8 TeV	1, 2, 3, 6, 12, 13, 15, 21, 22, 66, 79, 82, 83, 91, 111, 112 and 113

Table 10.1: The data runs used, the corresponding collision energy and bad LBs.

two had 87.3×10^{11} protons. The run 206881 had a total of 647 LBs. The first part of the run, until LB 336, was an elastic dedicated run and was not included in further analysis. The total luminosity was 24.11 nb^{-1}.
Run 206885 had 81.7×10^{11} protons in beam one, and 82.6×10^{11} in the other. It delivered a total luminosity of 6.651 nb^{-1} over 128 LBs.
The 7 TeV run, 191373, had a total of 263 LBs. Beam one had 1.35×10^{11} protons, and beam two had 1.48×10^{11}, and it delivered a total luminosity of 0.1032 nb^{-1}. The bad LBs of all three runs can be seen in table 10.1.

10.1 Trigger Information

The triggers are used to select interesting events that are relevant for further analysis. Here, the trigger logic will be explained. The triggers are based on

what is recorded in ALFA and ATLAS. Trigger information is found in ref. [21].

All triggers involved in this thesis, in addition to their specific selection, have a requirement on the bunch crossing identification (BCID) of the given event. These requirements are (ref. [26]):

- `BGRP_0` - All BCID, except the ones reserved for beam dumping.
- `BGRP_1` - Filled, meaning physics ready bunches.
- `BGRP_2` - CalReq. These are long gap empty bunches and used for laser calibration.
- `BGRP_3` - Empty, used for background studies.
- `BGRP_4` - IsolatedUnpaired. Unpaired refers to exactly one bunch in one beam, and isolated means BCIDs with at least 3 bunch separation.
- `BGRP_5` - NonIsolatedUnpaired. Same as `BGRP_4` except they are not isolated.
- `BGRP_6` - EmptyAfterPaired, empty bunches immediately following filled bunches.
- `BGRP_7` - AllUnpaired, combined `BGRP_3` and `BGRP_4`.

`BGRP_0` is the only one used for all triggers, while the others are trigger specific. In this thesis only `BGRP_0`, `BGRP_1` and `BGRP_3` are used.

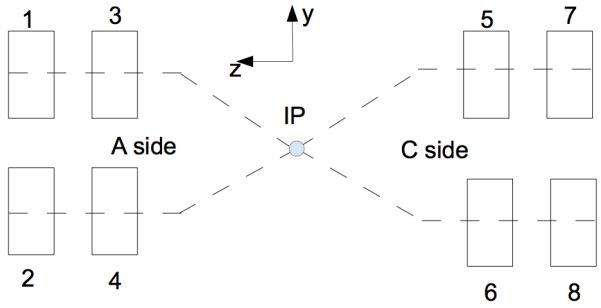

Figure 10.1: An overview of the stations in ALFA, numbered from 1 to 8. The dashed lines indicate the possible proton paths. IP is the interaction point.

An overview of the different stations in ALFA can be seen in figure 10.1. The four possible trajectories of the proton are referred to as arms in ALFA. Therefore the arm 13 is the path with detectors 1 and 3, meaning the upper left hand side of the interaction point (IP). Arm 24 is the lower left hand side, arm 57 is the upper right hand side and arm 68 is the lower right hand

side. This figure also gives an overview of which is the A side and which is the C side of the interaction point as this becomes important in the later analysis. Based on these stations, the trigger logic has been decided for the different triggers.
In the 8 TeV data runs, 206881 and 206885, the available, relevant triggers were:

- `L1_ALFA_ELAS15` and `L1_ALFA_ELAS18` - 250.
- `L1_ALFA_SDIFF5`, `L1_ALFA_SDIFF6`, `L1_ALFA_SDIFF7` and `L1_ALFA_SDIFF8` - 3000.
- `L1_LUCID_A_ALFA_C` and `L1_LUCID_C_ALFA_A` - 10.
- `L1_ALFA_ANY` - 300.
- `L1_ALFA_ANY_EMPTY` - 200.
- `L1_MBTS_2_A_ALFA_C` and `L1_MBTS_2_C_ALFA_A` - 10,

where the number following the trigger is the prescale used in the 8 TeV runs of the corresponding trigger. The prescale factor denotes the number of the triggers that are stored for offline analysis, e.g. a prescale of 200 means only every 200th event is stored. This is done to know the exact number of triggers fired. Using prescales ones know the exact number as it is the amount of triggers stored times the prescale. This becomes important when counting or calculating in a further analysis.

The first two are elastic triggers. `L1_ALFA_ELAS15` require a hit in one or both of the detectors of arm 13 and arm 68. In addition to this, it is also required that the bunch crossing is paired in ATLAS, meaning that the two bunches crossing in ATLAS were both filled bunches. Likewise, the `L1_ALFA_ELAS18` trigger is a hit in one or both detectors of arm 24 and arm 57 as well as a paired bunch crossing.
The `L1_ALFA_SDIFF5` to `L1_ALFA_SDIFF8` trigger requires a hit in both detectors of arm 13 (`SDIFF5`), arm 24 (`SIFF7`), arm 57 (`SDIFF6`) or arm 68 (SDIFF8). In addition it also requires `BGRP_1`
The `LUCID` triggers are based on the A and C sides of ATLAS. The trigger logic of `LUCID_A` refers to a LUCID hit on the A side, and the `C` referes to a hit on the C side. It is also required that one or both of the arms in ALFA of the opposite side of the LUCID hit is hit in both detectors. Last, `BGRP_1` is required.
The `MBTS` triggers are similar to the `LUCID` triggers, except that at least two of the MBTS segments are hit instead of just one hit in LUCID.
The `L1_ALFA_ANY` trigger is a hit in any of the eight detectors, while requiring `BGRP_1` as well. Likewise, the `L1_ALFA_ANY_EMPTY` is a hit in any of the

eight ALFA detectors, but with BGRP_3, i.e. empty events.
With the trigger logic explained, the trigger statistics available in the relevant runs can be seen in table 10.2.

Trigger	**Run 191373**	**Run 206881**	**Run 206885**
Total number of events	6,587,371	13,921,360	4,174,543
L1_ALFA_ELAS15	743,211	473,885	134,361
L1_ALFA_ELAS18	682,507	466,201	131,117
L1_ALFA_SDIFF5	944,625	57,737	17,000
L1_ALFA_SDIFF6	269,971	60,268	16,783
L1_ALFA_SDIFF7	536,176	57,132	16,397
L1_ALFA_SDIFF8	263,172	57,683	16,226
L1_LUCID_A_ALFA_C	0	2,156,805	621,765
L1_LUCID_C_ALFA_A	0	1,809,469	538,551
L1_ALFA_ANY	6,388,231	206,793	58,626
L1_ALFA_ANY_EMPTY	132,331	19,674	13,149
L1_MBTS_2_A_ALFA_C	0	4,611,851	1,378,327
L1_MBTS_2_C_ALFA_A	0	4,484,392	1,386,483

Table 10.2: Trigger counts of the different runs analysed in this thesis. The total number of events is also shown beneath the run numbers.

The trigger efficiencies, meaning the probability of firing the trigger given a proton within the detector acceptance, are found to be very high for the ALFA stations, see ref. [27]. For elastic triggering the efficiency is above 0.996 for all eight stations while the diffractive triggering system depends more on which detector is triggering, However, all eight stations has an efficiency above 0.99, which is very high. Trigger efficiency is therefore not considered further in this thesis.

11 Calorimeter Noise

In section 9, a forward rapidity gap for a 7 TeV run was introduced. In that analysis both the calorimeter parts and the inner detector was used to find the gap. However, due to the way the calorimeters are designed, a correction for noise is needed to make the data useful.

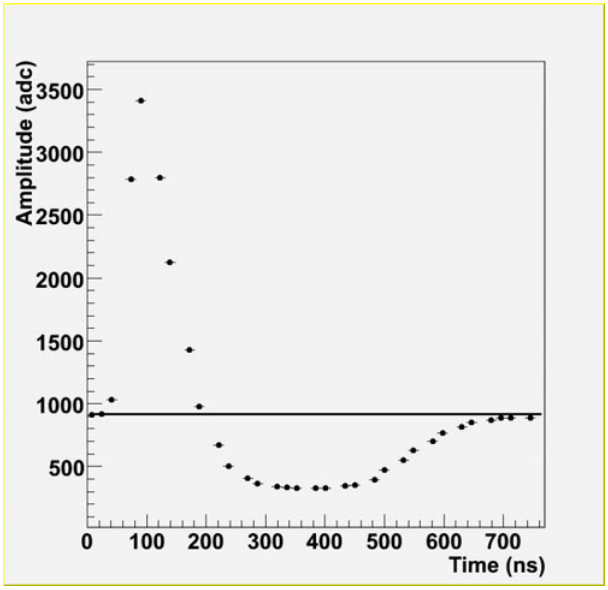

Figure 11.1: The recharge time for calorimeter cells. This plots shows ATLAS data arising from cosmic rays. [57].

The calorimeter noise arises because of the many collisions occuring over short intervals of time. The calorimeter measures an energy deposit in cells, and after a cell has been hit it takes time to normalize the output signal when storing event data, see figure 11.1. Here the amplitude peak refers to the size of the energy deposited in the calorimeter cell. When the signal has passed, it is seen that the calorimeter takes a period of time to normalize the signal output to zero, sometimes overshooting, sometimes underestimating. For this reason, it is possible to see remnants of the previous event leave a signal in the current event as a gaussian signature around 0. To remove this noise, a significance cut can be defined. The significance is defined as

$$P = \frac{S}{N} \quad , \tag{11.1}$$

where S is the signal and N is the average size of the noise. N is determined by plotting the energy deposits of the calorimeter. This plot should show a

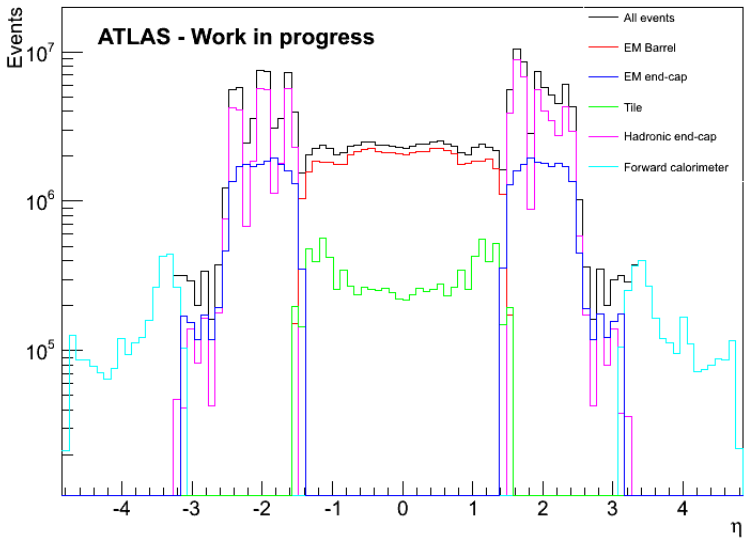

Figure 11.2: Distributions of η for the different calorimeter parts.

gaussian profile around zero energy with a long non-gaussian tail. This tail represents the signal in the calorimeters, while the gaussian profile is due to noise. Thus, N is the width of the gaussian noise profile. Therefore, to remove noise from the calorimeter contribution to the rapidity gap measurement, a calorimeter noise investigation was carried out.
It turns out that calorimeter part specific cuts are needed as the noise is diffferent in, for example, the FCal compared to the EM barrel calorimeter. After the noise reduction cuts, the η distribution of all calorimeters can be seen in figure 11.2. Here, a requirement of $\mathbf{p}_T > 200$ MeV and a significance above ~ 4 is required. This should remove the noise contributions, and one would then expect a roughly constant production of particles per unit of η. It is seen that the distribution is far from what would be expected for minimum bias events. Here, a large amount of clusters in the calorimeters are found, especially in the hadronic end-cap. To investigate this further, empty events are used.
Empty events are events where, given the selection or trigger, the calorimeter should have no signal. One way to select empty events is to use the `L1_ALFA_ANY_EMPTY` triggers. This triggers on unpaired bunch crossings, meaning bunch crossings where the bunches are empty. Another selection of empty events is to choose golden elastic events, see section 12 for details on the golden elastic cuts. In addition to the golden elastic cuts, it is required to have no hits in the MBTS or LUCID detectors, and a requirement of no

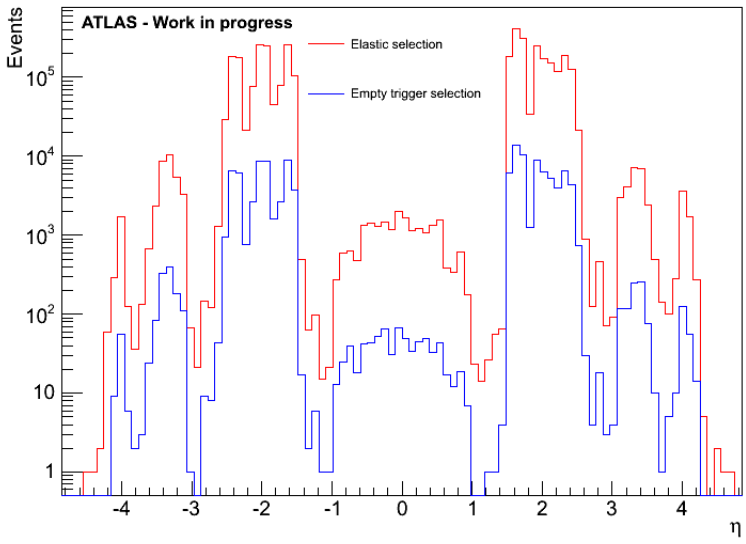

Figure 11.3: A distribution of η for all the calorimeter parts for empty events. A selection of golden elastic and empty trigger is shown.

reconstructed vertex in the inner detector. These cuts should ensure that no pile-up collision occurs along with the elastic event. The result can be seen in figure 11.3.
As seen in figure 11.3, even empty events have large noise distribution. For the `EMPTY` trigger there is not a single track in the inner detector, and the empty elastic selection has 120 out of 802522 events with one or more tracks. Therefore, it is not in the selections that problem arise. The shape of the distributions is also roughly similar to that of figure 11.2 which suggests that the largest contribution to figure 11.2 is in fact noise. Thus, an obvious problem has been encountered with the data. As the calorimeters have worked for other data runs it is not there the problem arises, and therefore it is most likely due to a problem in the reprocessing of the data. When data is collected at ATLAS, it does not come in ready-to-analyse data files, but rather a reprocessing has to take place to transfrom the raw data into the files used in this thesis.
As there was no time to look into this process and fix it, the calorimeter data will have to be disregarded for the rest of the thesis. This is a problem for the further analysis of diffractive events, especially the analysis of rapidity gaps. The effect is a smaller range in the η distributions in ATLAS as well as the maximal size of the forward rapidity gap.

12 Elastic Events

This section is dedicated to elastic events, as part of the thesis aim was to incorporate golden elastic events into the framework used for diffractive event analysis. The reason behind this is to establish a possible exclusion of elastic events from the central diffraction event selection.

Cut-Flow	Number of events
Total number of events	6,587,371
BCID = 1	1,889,587
Luminosity cut	1,817,050
Trigger	1,103,790
Reconstructed tracks	897,289
Acolinearity cut in x	863,117
Acolinearity cut in y	849,264
x vs θ_x background cut	835,327
Beam screen cut	802,167
Detector edge cut	795,128
Pile-up Rejection	793,573

Table 12.1: The cut-flow for the 7 TeV data run, 191373. On the left the cuts are mentioned, and on the right the number of events, after the cut, is written.

The 7 TeV elastic cut-flow can be seen in table 12.1. The cuts were developed by the ALFA group at CERN, ref. [25]. The bunch crossing ID (BCID), LB and trigger cut are the simplest. The first two are done to exclude bad data while the trigger is selecting events for further analysis. The triggers considered are the `L1_ALFA_ELAS15` and `L1_ALFA_ELAS18` triggers for the obvious reasons.
For an elastic event in ALFA, it is required that there are hits in two of the ALFA arms, one on each side. It is also required that these arms are not both an upper arm or a lower arm. Hence there are only two possibilities, arm 13 and 68 or arm 24 and 57, see figure 10.1. This is the reconstructed track cut.
Due to momentum conservation, the transverse momentum of the two elastic protons must be equal. This means that they are expected to hit ALFA back-to-back. The acolinearity cut in x and y are back-to-back requirements. The cut is done for both inner and outer ALFA stations in both x and y.
As has been discussed previously, it is known that elastic events have an energy transfer of $\Delta E = 0$. Thus, when considering the discussion at the end

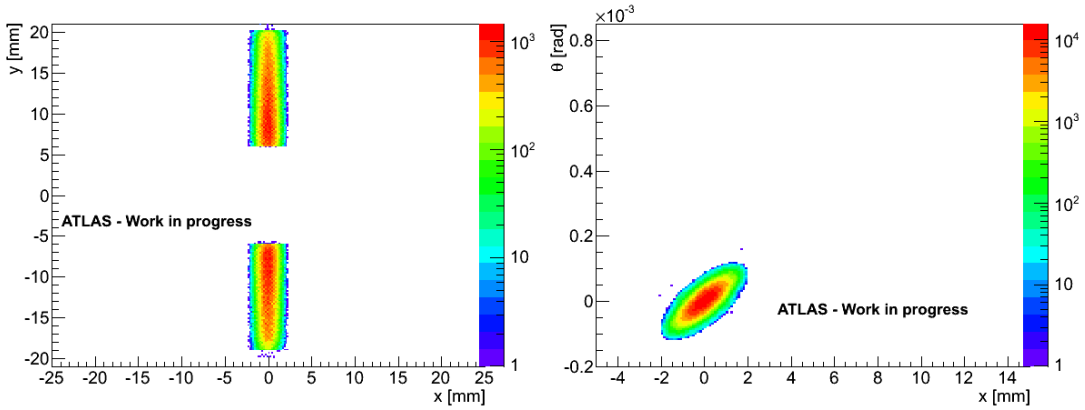

(a) (b)

Figure 12.1: The data after all cuts for the entire data run. (a) shows the hit map, the x coordinate plotted against the y coordinate. (b) is the correlation between the x coordinate and the θ_x angle.

of section 9, it is expected that the elastic signal only has hits centered on $x = 0$. To account for this, a cut in the x-θ_x plane is introduced. This ensures that the direction of the track in ALFA has the direction corresponding to an elastic signature.
Events with both elastic triggers fired undergo a pile-up cut. This selects the most-elastic-like event and discards the other. The beam screen and detector edge cuts will be discussed in section 14.1. They remove events that are too close to the edge of the detector increasing the likelihood that the particle is only seen by one detector. The beamscreen cut removes particles that are due to showers or scatterings from the beamscreen.

As this elastic analysis was done to include the selection into another framework than the one used by the ALFA group at CERN, the 191373 data run was reprocessed. However in the reprocessing of the run, five files out of 1162 failed, and therefore the cut-flow presented here has slightly fewer events than that of the ALFA group. The loss is of the order ~ 4000 elastic events, but the relative number of events per cut is the same without the five files as what is found by the ALFA group. It is therefore not that important, as in this thesis they will only be used for comparison and background discussions.

The result of the the cuts is shown in figure 12.1. This is exactly as was expected, events centered around $x = 0$, corresponding to $\Delta E = 0$.
With the elastic cuts, the number of events with at least one vertex in ATLAS

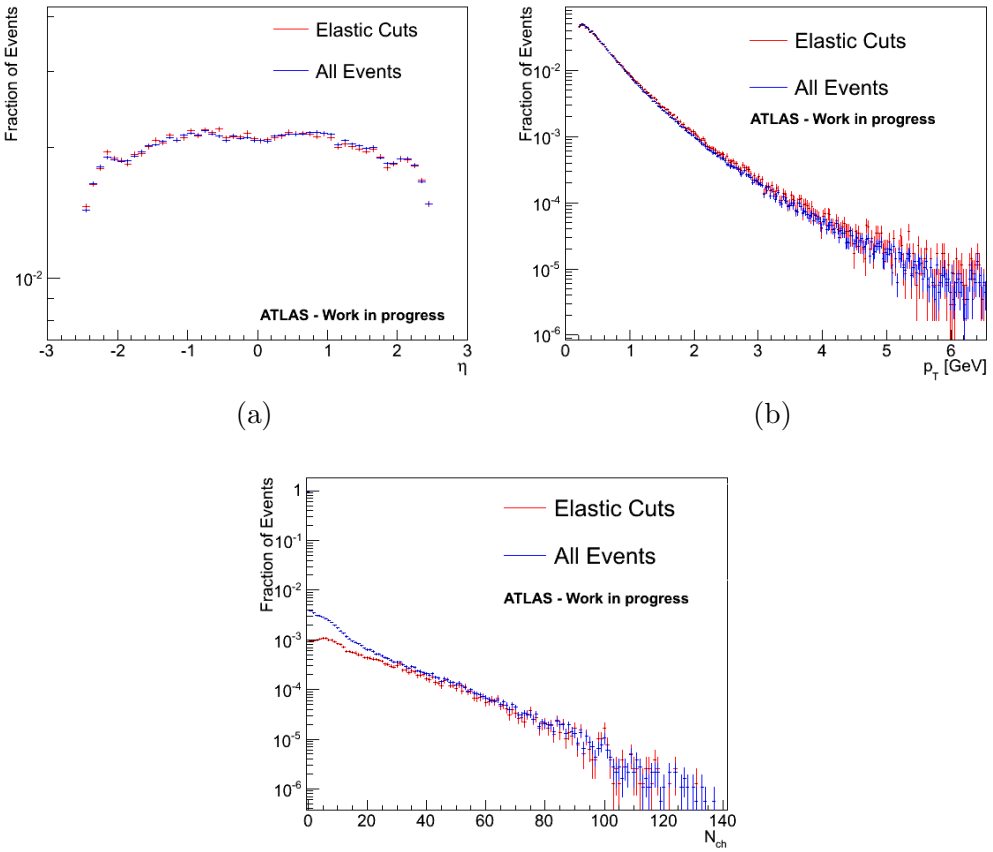

Figure 12.2: ATLAS activity for the full elastic cut selection and all events in the given run. (a) shows the η distribtion of tracks., (b) is the $\mathbf{p}_T$ of the tracks and (c) is the number of tracks per event.

is 18,518 events. Hence roughly 2% of the events have activity in ATLAS, and this activity is shown in figure 12.2. It is seen that the tracks in ATLAS show similar traits as the minimum bias events indicating that these are pile-up collisions, i.e. events where there was both an elastic event and a minimum bias event in the same crossing. Another possibility is that these events are low energy loss central diffractive events, and this type of event is discussed further in section 15.

The energy of the elastic proton is expected to be 3500 GeV at $\sqrt{s} = 7$ TeV, and a plot of the energy can be seen in figure 12.3. The method for determining the energy of a proton measured in ALFA is explained in section 14.1. A gaussian fit of the elastic region results in a mean of 3500.70 ± 0.04 GeV and a width of 36.31 ± 0.03 GeV. It is also seen that some noise remains in the energy spectrum. The energy plateau in the region ~ 3180 to ~ 3360 is seen in diffractive events as well, and it will be discussed in the later sections. The remaining background contribution is close to a factor 100 smaller than the signal, and therefore the signal is considered fairly clean. As elastic events are well known, this fit roughly determines the energy resolution measureable with ALFA. For a further and more precise discussion on energy resolutions, see ref. [28].

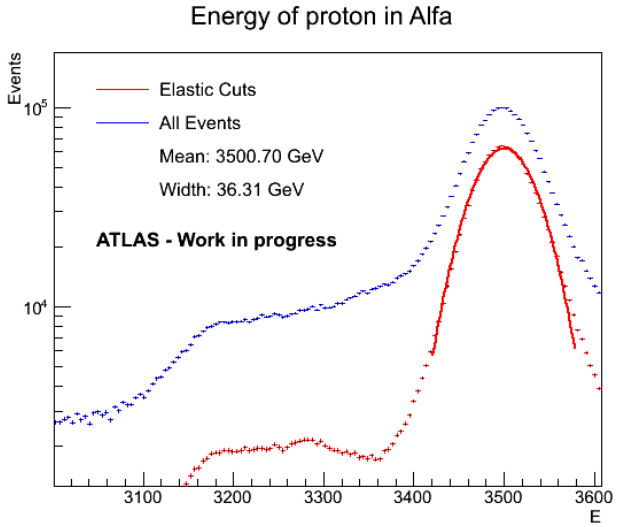

Figure 12.3: Energy of the elastic proton in ALFA. Both the elastic signal and all hits in ALFA is shown. Included is also a gaussian fit of the elastic signal fitted to the region 3425 to 3575 GeV.

This concludes the elastic analysis, and the following sections will discuss

diffractive events measureable with ALFA. The elastic events, because they are well know and well defined, will be referred to occasionally for comparison between elastics and low ξ diffractive events and other background related discussions.

13 Rapidity Gap Definition

It has previously been mentioned that the presence of a rapidty gap is a signature of diffractive events. In this section, a definition of how the rapidity gap is found and measured for the rest of this thesis is introduced. The method is chosen because it allows for an easy adaptation to a search for multigap structures.

To find the forward gap, one slices the η region of the ATLAS detector, from -4.9 to 4.9, into 98 steps. This results in a stepsize of 0.1. When a track, passing the cuts specified, is detected the corresponding η slice is marked. An example of an event is shown in figure 13.1. A rapidity gap can then be determined by counting the number of slices between two neighbouring filled slices.

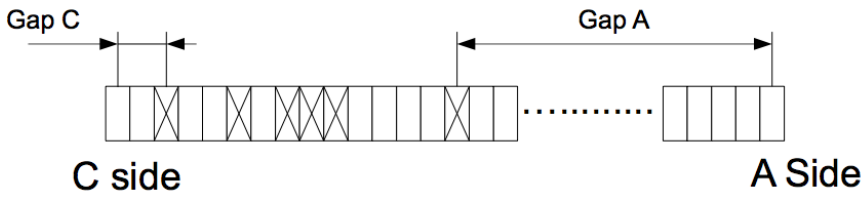

Figure 13.1: An example of how an event might look when the η region has been sliced into 98 steps of 0.1. The dots indicates a large number of empty slices. The definition of gap A and gap C is also shown.

When considering SD events the forward rapidity gap, $\Delta\eta_F$, is defined as the gap from the edge of the detector to the nearest track. As there is both an A and a C side of the ATLAS detector, two forward gaps are found per event. In previous experiments, see section 9, the forward gap was defined as the largest of these two gaps. However, in this analysis, a tagged proton is used, and therefore one knows from which side to start counting empty η slices, the one with the proton. Gap A refers to the forward gap where one starts counting empty slices from the A side, and gap C from the C side.
As there was trouble with the calorimeter noise for the 8 TeV data, only the inner detector regime is considered.

14 Single Diffraction

In this section, it will be discussed how to select single diffractive (SD) events. The selection is based on information from ALFA and ATLAS. It is important to know that all results and discussions for the rest of this thesis will be preliminary. This is because the final alignment of ALFA has not been completed in time to be applied. Likewise, the final esitmate of the optics, i.e. the magnet effects on the protons travelling between ALFA and ATLAS, is not yet implemented in the software used here. While this is expected to have an effect on data, the effect is small, and hence the data can still be used in a diffractive analysis. No full Monte Carlo simulation has been produced yet for SD events at 8 TeV. Therefore, a toy model Monte Carlo is used to make rough comparisons between simulation and data. In addition, a background discussion and a look into the ATLAS distributions will also be given.

The diffractive event selection will be developed for the 8 TeV data sets as these runs are diffractive dedicated runs. A plot of the raw data can be seen in figure 14.1. Both the hit-map, 14.1a, and the angle plot, 14.1b, shows all ALFA stations combined into one figure. In both plots, an elastic or low energy loss diffractive signal is clearly visible as the red area, and in the angle plot the rest of the diffractive signal is also visible as the green area of positive correlation. The negatively correlated ellipse is LHC background, and it will be discussed in section 14.3.

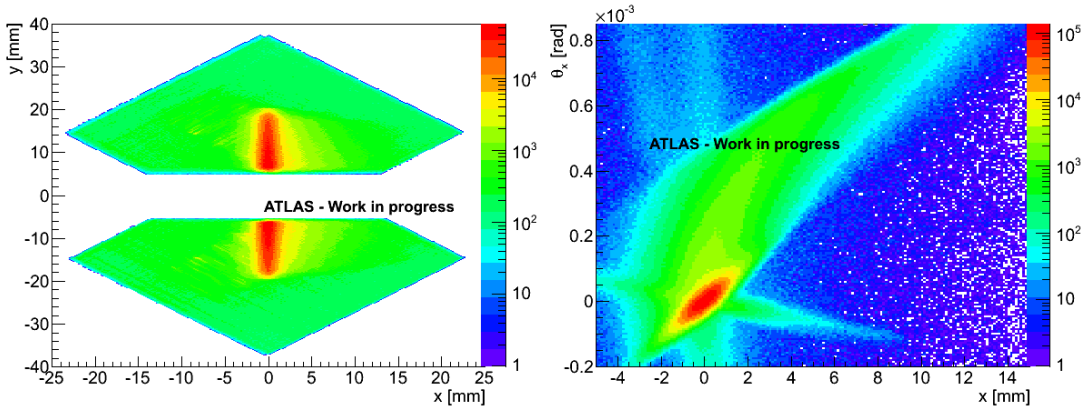

(a) (b)

Figure 14.1: The raw 8 TeV data. (a) shows the hit map, the x coordinate plotted against the y coordinate. (b) is the correlation between the x coordinate and the θ_x angle. The z axis is number of events in both plots.

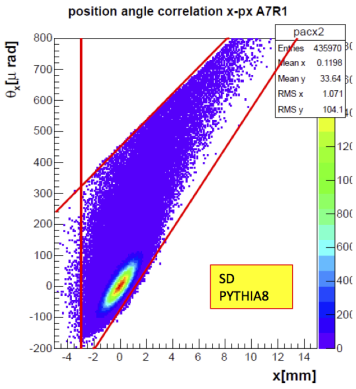

Figure 14.2: A simulation of the expected diffractive proton signal in ALFA, shown in a x vs θ_x plot. The red lines enclose the region thought to contain diffractive protons. [55].

In section 7.3 and 9 the shape of a diffractive signal in ALFA was mentioned. The conclusion was that, as the energy loss of the diffractive proton increases, it moves towards higher positive x values in ALFA. Because there are two ALFA stations on both sides of the interaction point (IP), a track in ALFA can be measured. Therefore, the x scattering angle, θ_x, of the proton can also be measured. It is defined as

$$\theta_x = \sin^{-1}\left(\frac{x_{241} - x_{237}}{\mathrm{RP}_{\mathrm{dist}}}\right) \approx \frac{x_{241} - x_{237}}{\mathrm{RP}_{\mathrm{dist}}} \quad , \tag{14.1}$$

where x_{237} and x_{241} refers to the x coordinate at the inner and outer roman pots, at ± 237.398 or ± 241.538 m in the z coordinate. $\mathrm{RP}_{\mathrm{dist}}$ is the distance between the inner and outer roman pots. The last approximation, $\sin x \approx x$ for small x, is valid in this analysis as the angles are very small, and the approximation error is not comparable to the error from the x measurements. It turns out that a diffractive signal is more clearly visible in a x-θ_x plot, as shown in figure 14.2. Here the red lines enclose the diffractive signal region, referred to later as the diffractive banana region due to its shape. The tail, at higher values of x and θ_x , reflects higher energy losses of the proton. Inside the diffractive region, a positively correlated ellipse is seen, centered roughtly on $(0, 0)$. This ellipse is also a signature of elastic events as this area represents protons with either very small or no energy loss. As this is a simulation for single diffractive events only, it is seen that most diffractive protons are expected to lie in this region. This is why elastic events are background events to diffractive events, especially central diffractive as these require protons on both sides of the interaction point, like elastic events.

However, at higher energy losses of the proton, the signal moves up in both angle and x coordinate. Hence it becomes distinguishable from elastic signals. This energy loss will, for the rest of this thesis, be expressed in terms of ξ, defined as

$$\xi \equiv 1 - \frac{E_{\text{proton}}}{E_{\text{beam}}} \quad . \tag{14.2}$$

In addition to this expected ξ dependent hit pattern in ALFA, the forward rapidity gap, $\Delta\eta_F$, is the most characteristic signature of a diffractive proton. Remembering the experimental definitions of diffraction in section 4, the gap distribution for diffractive events is expected to be roughly constant, while it is exponentially supressed for non diffractive events.

14.1 The SD Selection

This section will go into detail concerning the selection and identification of SD events. As run 206881 and 206885 are both 8 TeV data runs with the same optics, beam and LHC configuration, the cut-flow is developed and applied to the combined data set for the rest of this analysis. Certain cuts are run specific, and that has been taken into account.

Cut-Flow	Number of events
Total number of events	18,095,903
Luminosity Block cut	17,266,910
Trigger	15,282,220
Reconstructed tracks	14,678,940
Multiplicity cut	10,985,520
Veto on other tracks	8,519,494
MBTS hit cut - Same side	8,057,218
MBTS hit cut - Opposite side	5,753,163
Beam screen cut	5,741,517
Detector edge cut	5,734,564

Table 14.1: The cut-flow for the SD events of the combined 8 TeV data runs, 206881 and 206885. On the left, the cuts are mentioned, while on the right the number of events remaining after the cut is written.

The cut-flow for SD events can be seen in table 14.1. The cuts are good luminosity blocks (LB), triggers, reconstructed track, multiplicity, veto on other detectors, two MBTS hit cuts, beam screen and detector edge cuts. The selection shown in table 14.1 is the final selection. The following will

explain the cuts in detail, discuss the result and give the reasoning behind some of the cuts, such as why no vetex requirement is included and the effect of the MBTS cuts.

The first cut is excluding the bad LBs from the analysis, see table 10.1 for a full list of excluded LBs. This is done as the data quality is poor in these LBs, and therefore they are excluded from any further analysis.
The triggers represents the first real selection of events, and it is used to select possible SD candidate events in the given data run. The available trigger information was introduced in section 10.1. From the previous sections, the expected SD signature is a forward proton with minimum bias activity on the opposite side of the proton. Hence, to select a SD candidate event, the triggers used are `L1_ALFA_SDIFF5-8`, `L1_LUCID_A/C_ALFA_C/A` and `L1_MBTS_2_A/C_ALFA_C/A`. The `MBTS` and `LUCID` triggers make the most sense as they require hits in both detectors of any ALFA arm and hits in the MBTS or LUCID detector on the opposite side. This is the very essence of a SD event, and they are therefore used to trigger events for further analysis.
In addition to this, the `L1_ALFA_SDIFF5-8` triggers are also used to select events as it requires a recontructed track in ALFA, i.e. hits in both detectors of an ALFA arm.
Because of the large distances between the interaction point (IP) and ALFA, the angles measured in ALFA are very small, roughly of the order $\sim \mu$rad. This means that, if a proton hits one of the ALFA stations it will also hit the second, unless it is at the very edge of the detector. It is possible that, when the proton hits the ALFA station, it breaks into a hadronic shower which gives trouble in the reconstruction of a hit. To remove events where this is the case, a cut requirement of a reconstructed track is required. This means that, for the selected ALFA arm, it is required that the number of hits in the inner detector corresponds to the number of hits in the outer detector for that arm.
One of the biggest issues with a diffractive selection is that it is not easily possible to match a detected proton in ALFA with a vertex in ATLAS. This is due to the many magnets between the IP and ALFA. A proton kinematic reconstruction code, see ref. [28], is used later to determine the energy of the proton. This code uses, amongst other variables, the vertex or beamspot information of ATLAS to determine the kinematics of the proton. However, in the case of multiple tracks in ALFA, it is not possible to know which of the tracks in ALFA originates from a vertex in ATLAS (if any), and therefore events with more than one reconstructed track in ALFA are cut away. This is the multiplicity cut.
Along the same lines and to exclude elastic events, a veto on the other ALFA

	1	2	3	4	5	6	7	8
BS, 206881	19.28	-17.87	20.24	-18.74	19.28	-19.64	18.4	-18.72
DE, 206881	5.43	-5.62	5.78	-5.78	5.72	-5.75	5.48	-5.59
BS, 206885	19.32	-17.9	20.28	-18.77	19.24	-19.6	18.4	-18.7
DE, 206885	5.43	-5.64	5.78	-5.78	5.73	-5.75	5.49	-5.59

Table 14.2: The values of the beam screen (BS) and detector edge (DE) cut for the two 8 TeV runs. The numbers, 1 to 8, refer to the different detectors as shown in figure 10.1.

arms is also used. This means that no track, beside the one used for analysis, are present in the other ALFA arms.
As the `LUCID` and `SDIFF` triggers only relies on ALFA and LUCID, to enhance the probability of some activity in the ATLAS acceptance, events with no hits in the MBTS are vetoed. This cut will require at least one hit in the MBTS on the opposite side of the detected proton.
In addition to this, to suppress events with a beam gas background hit in ALFA and a non-diffractive interaction in ATLAS, it is required that there are no more than eight hits in the MBTS on the same side as the detected proton candidate. This cut is also referred to as a 'clean proton' cut, meaning that forward region of the proton side should be less populated by particles compared to a non-diffractive event.

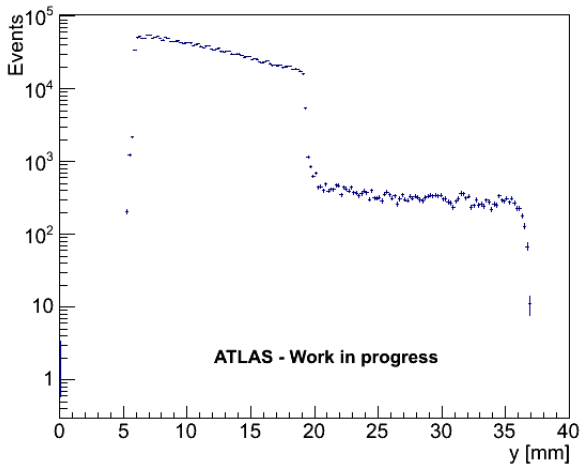

Figure 14.3: The y distribution for ALFA detector 1. The high event plateau defines the region of good events. This plot contains all events of the run 206885.

As mentioned in section 5.1, beamscreens are used to protect the magnets. These, however, can be hit by particles scattered at low angles from the IP. This means that the beam screen can possibly absorb protons that would otherwise hit ALFA. If the beam screen is hit, it can also create showers that make it all the way to ALFA. Therefore a beam screen cut is introduced to remove these particles. The cut removes hits that have a $|y|$ coordinate above ~ 20 mm as this is where the beam screen causes trouble.
Hits at the very edge of the detector, towards the beam, have a high chance of not hitting the other detector of that arm. Therefore events that are less than 60 μm from the edge are removed. The beam screen and detector edge cut values can be seen in table 14.2.
The beam screen cut were found from plots similar to that of figure 14.3. The high plateau from ~ 5 to ~ 20 is the region of good data, and the beam-screen and detector edge cuts are defined as the y value where the good data begins plus a buffer of 60 μm. These cuts are run specific, hence they are made separately for both the 206881 and 206885 run.

The result of the cuts can be seen in figure 14.4. Figure 14.4a and 14.4b shows the hit information of ALFA, 14.4a is the hit map and 14.4b is the x-θ_x plot. Both agree well with the expected signature.
The energy loss of the proton after all cuts, ξ, is plotted in figure 14.4c. The expected peak at low ξ values is visible as well as the fall off for higher values. However, a plateau is seen that is not present in simulations. This plateau will be discussed in greater detail in section 14.3. To find the energy of the diffractive proton, a reconstruction code has been used. This code uses the hit coordinates in ALFA and vertex (or beamspot, if no vertex is available) information to calculate the proton energy. The code was made via detailed Monte Carlo studies of the transport of protons from ATLAS to ALFA. With these variables, it extrapolates the hit information backwards, through the magnetic field, to see which proton energies can correspond to a hit of that kind. See ref. [28] for details.
Some of the plots discussed in the further analysis are side specific, as the proton is seen on one side versus the diffractive mass system on the other. These are plots regarding the rapidity gap measurements or η distributions in ATLAS. Therefore, when side specific plots are discussed, only events with an A sided proton are used in further analysis. A comparison of A and C sided protons can be seen in appendix B.1. It is seen that they give similar results for the cuts, and therefore which side is chosen does not matter.
Last, the rapidity gap distribution, after all cuts, is shown in figure 14.4d. Note the clear difference between which side the gap is counted from, i.e. when the gap is measured from the proton side it becomes approximately

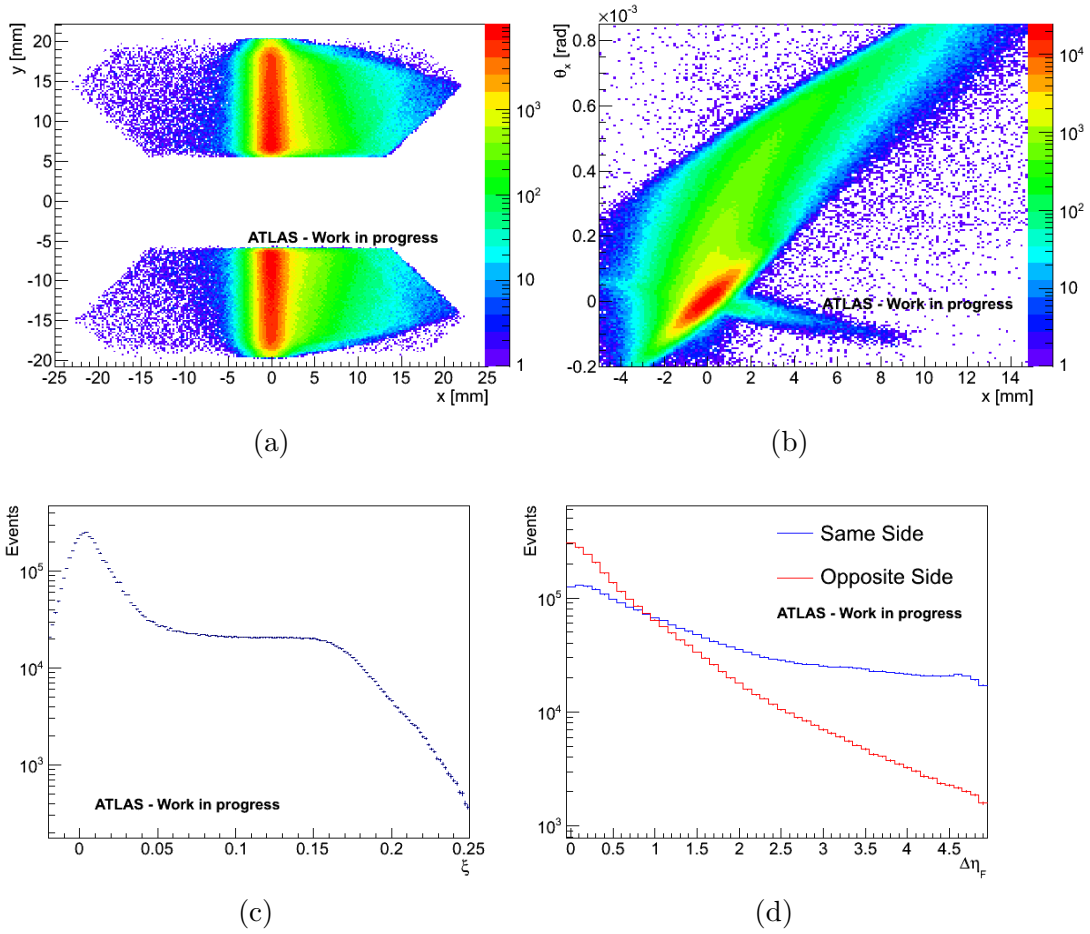

Figure 14.4: The data after all SD cuts for the entire data run. (a) shows the hit map, i.e. the x coordinate plotted against the y coordinate. (b) is the correlation between the x coordinate and θ_x angle. In plot (c) the ξ distribution of the protons is shown, and (d) shows the rapdity gap distribution from both sides, given a proton on the A side.

constant for higher gap sizes while the opposite side decreases exponentially over the entire gap size range.

The expected diffractive signature is clearly visible, yet it is seen in figure 14.4 that background hits are still present after applying the cuts, visible as a uniformly spread distribution of hits and a negatively correlated ellipse in figure 14.4b. However, compared to the total number of events, these make up a small fraction of events. About 0.8% of the events are outside the diffractive banana region. As this number does not include events inside the

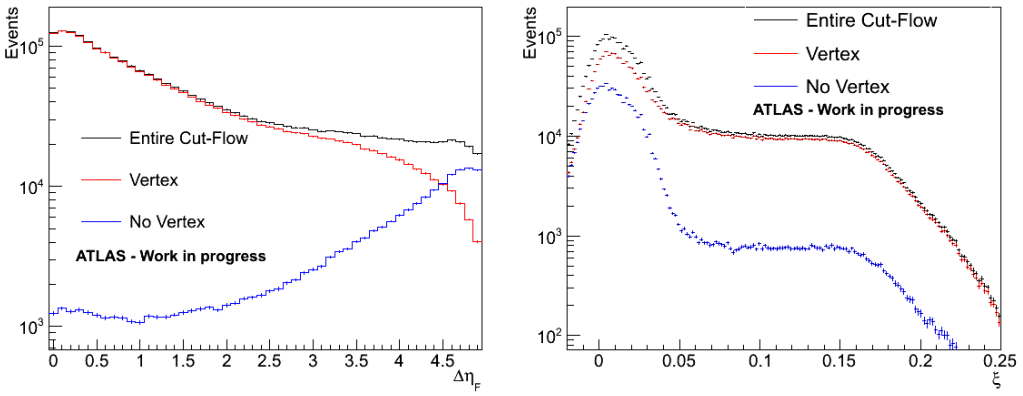

(a) (b)

Figure 14.5: The effect of excluding a vertex cut in the SD selection with a SD proton in ALFA on the A side of ATLAS. (a) is the effect on the forward gap size due to the two subsets, no vertex and at least one vertex. The gapsize is measured from the same side as the proton. (b) shows the ξ distribution of the same two subsets.

SD region that are really background events, it is not the entire background. It will be seen that there is a significant amount of these. The background ellipse, seen in both figure 14.1b and 14.4b, is due to beam induced background. All background events will be discussed in section 14.3.

Another cut that might seem obvious, in a SD selection, is a vertex requirement in ATLAS. However, as is shown in figure 14.5a, this will exclude a small but significant amount of events where one or a few reconstructed tracks are found, but no vertex, in the inner detector. This is seen by the fact that, for large gap sizes, the distribution with no vertex is the dominant contributor to the forward gap size distribution. Therefore they are likely to be part of a forward diffractive mass system where the rest of the particles were simply too forward for the acceptance region of the inner detector. In ALFA, this should correspond to a larger fraction of lower ξ diffractive protons, and this is indeed the case as is seen in figure 14.5b.
Before any conclusion can be reached, one has to consider the amount of these events that could be background. In ALFA, the number of events outside the diffractive banana region is smaller for the distribution with no vertex, $\sim$ 0.4%, compared to $\sim$ 1% with a vertex. Both numbers are small, but there is still more than a factor of two difference. The plateau is still visible in the ξ plot, but, compared to the size of the low ξ-peak, it is significantly smaller,

and therefore especially events with a low ξ are seen to be more likely to not have a vertex in ATLAS.
Given an event with no vertex and a proton in ALFA, 87.9% of the events have no hits in the MBTS on the same side. As a comparison, 97.0% of the elastic events in the 7 TeV data have zero hits on any side in the MBTS. Because SD events with no vertex are seen to generally have a lower ξ, the diffractive mass system is not expected to have aquired enough energy to cover large, if any, areas of η in ATLAS. It is therefore seen that, in figure 14.5a, some background from non-diffractive events is visible at gap sizes ≤ 1. This indicates the size of the background contamination in ATLAS for a selection without a reconstructed vertex, and it is roughly a factor 10 smaller than the signal.
This shows that the subset of the cut selection with no vertex in ATLAS seems to show a higher signal-to-noise ratio than the rest of the selection. The reason for this is likely to be the triggering. The chance of seeing a beam induced hit in ALFA does not depend on what is happening in ATLAS. Therefore, the probability of triggering a non-diffractive event in ATLAS plus a background hit in ALFA is likely. However, the chance that the trigger fires on events with no vertex but hits in the MBTS (and maybe a few tracks) is lower, as non-diffractive events are not likely to be this forward.

In figure 14.6a the MBTS hits on both sides are shown, given a diffractive proton on the A side. This plot is made without the clean proton cut, i.e. the requirement of less than nine MBTS hits on the same side. A clear SD signature is seen as the band of events with zero hits in the MBTS on the same side, however a signal resembling non-diffractive events is also seen in the regime with a high number of hits in the MBTS on both sides. Because of this, a look into the effect of requiring different MBTS cuts on the same side has been done.
Three cuts were chosen. First, a cut removing all events with MBTS hits on the same side, i.e. selecting only the band on the left hand side of figure 14.6a. The second and third are chosen to cut away events with more than four and eight hits respectively in the MBTS on the same side. These cut values were, to some extent, arbitrarily chosen based on the plot in figure 14.6a.
These selections limit the amount of background found outside the SD banana region, the stricter the MBTS cut, the less background is found outside the diffractive region. However, the stricter cuts also remove high ξ events where the kinematics of the diffractive system allow particles to be created over larger regions of η. This can be seen in figure 14.6b and 14.6c which is the forward gap size and the energy loss, ξ, of the diffractive proton.

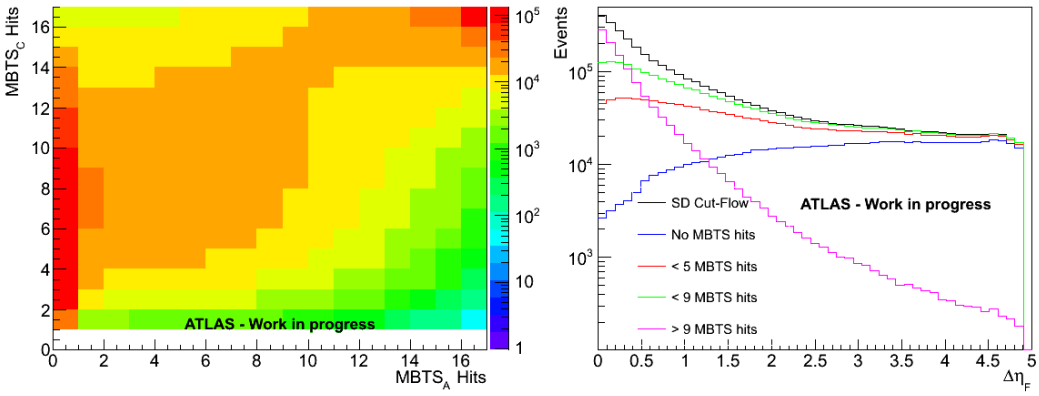

(a) (b)

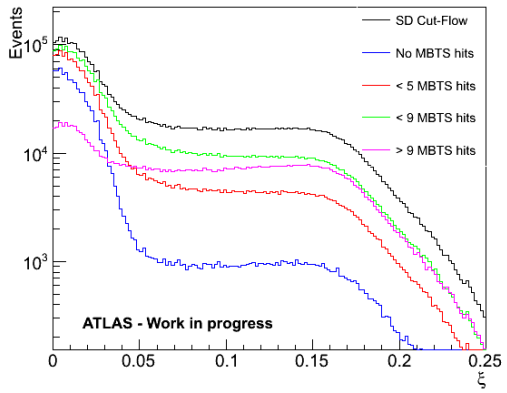

(c)

Figure 14.6: (a) shows the MBTS hits given the SD cuts and the diffractive proton is found on the A side of ATLAS. (b) and (c) show the effect of cutting on the MBTS hits on the same side as the proton. The cuts chosen are a maximum of zero, 4 and 8 hits. Events with 9 or more MBTS hits are also included. (b) is the forward gap size and (c) is the ξ distribution. In this figure, SD cuts refers to the SD cuts minus the MBTS hits requirement on the same side.

The purple line are events with 9 or more MBTS hits on the same side. This selection is shown to discuss the events removed by the 'clean proton' cut. As will be discussed in section 14.2, because of the low ξ peak seen in figure 14.6c, a significant part of these events are likely due to beam induced background. Therefore events with more than eight hits in the MBTS on the same side are likely to be non-diffractive events with beam background in ALFA. These have therefore been excluded from further analysis.

Thus, overall a clear single diffractive signature is seen with the chosen selection, such as a flattening distribution of forward rapidity gap sizes and the hit shapes found in ALFA. However, some unexpected features were seen as well, such as the plateau in the ξ distribution. This, and other features, will be discussed in the following sections.

14.2 MC comparison

In the cut-flow table, table 14.1, it is seen that some cuts remove quite a large amount of events. As some of these might be diffractive events, this section will discuss the effect of these cuts and how the acceptance regions of ALFA and ATLAS affects the cut-flow. This is done using a toy model Monte Carlo (MC) simulation of SD events at $\sqrt{s} = 8$ TeV, see section C. The simulation is made using Pyhtia 8 with default options, and it contains only events where the proton is within the ALFA acceptance region. All MC plots presented here uses truth information only, as a detector simulation has not been done. Because of this, the plots shown here are only used as a comparison between shapes of distributions. Note also that, in this section and later when discussing this MC, a hit therefore refers to seeing a truth particle with simple properties, such as being within the η acceptance relevant or passing a $\mathbf{p}_T$ cut.

In figure 14.7 the result is shown for this MC. The first two plots show the x-θ_x plot for two different selections. These are all simulated events and the subset which have particles in the MBTS region corresponding to the SD cuts. Figure 14.7a shows all simulated events and 14.7b shows the MBTS selection. The two distributions are seen to be very similar in shape, however it is important to note that the selection with the MBTS-like cut only has $\sim 54\%$ of the events of the entire simulation. The implication of this is that the selection developed previously removes roughly half of the actual diffractive events, and this is not desired in a SD selection.
The ξ and $\Delta\eta_F$ distributions can be seen in figure 14.7c and 14.7d. It is seen that requiring both MBTS cuts does not change the shape of the distributions

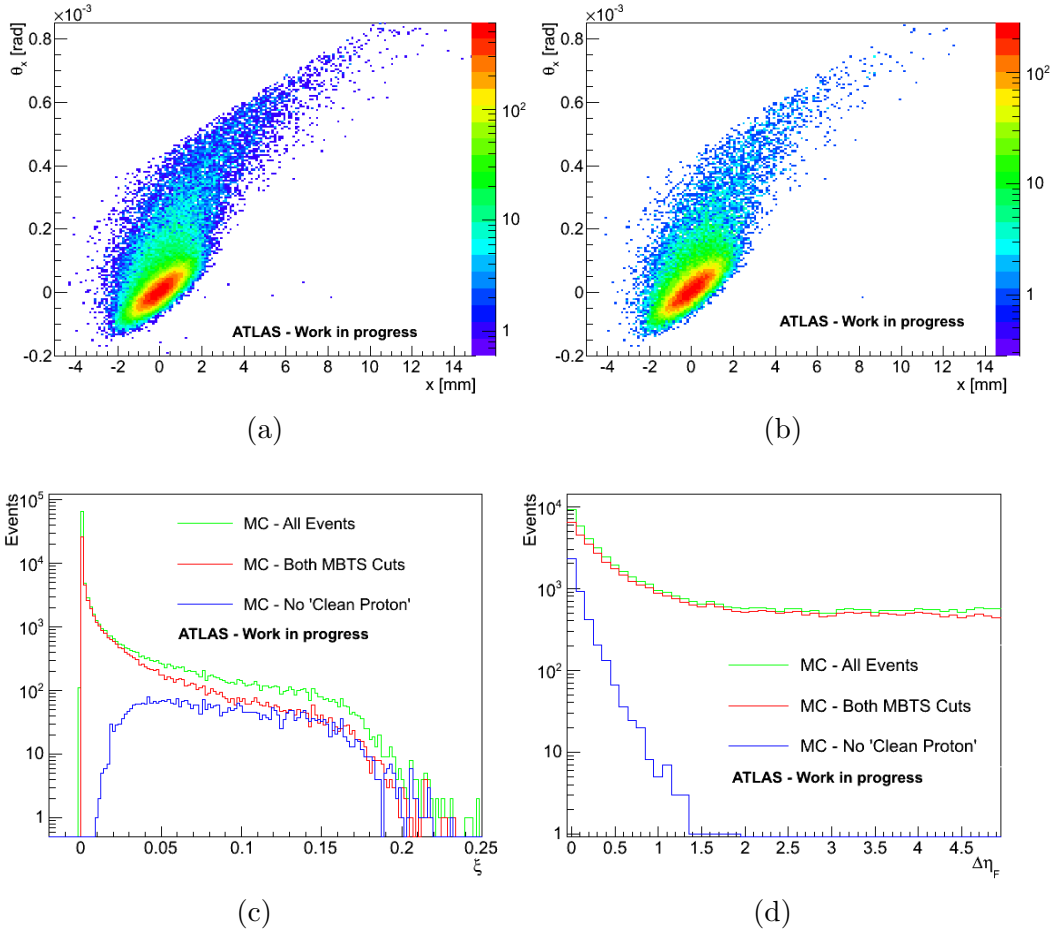

Figure 14.7: A $\sqrt{s} = 8$ TeV Pythia 8 simulation of SD events. (a) shows the angle correlation plot at ALFA coordinates, and (b) shows the same but with a cut on MBTS hits similar to that of the SD selection, i.e. at least one hit on the opposite side and a maximum of eight on the same side. (c) is the ξ distribution of the two MC selections. (d) is the same, but for the forward gap size, $\Delta\eta_F$. (c) and (d) includes the selection where the MBTS cut on the opposite is passed but the 'clean proton' cut is not.

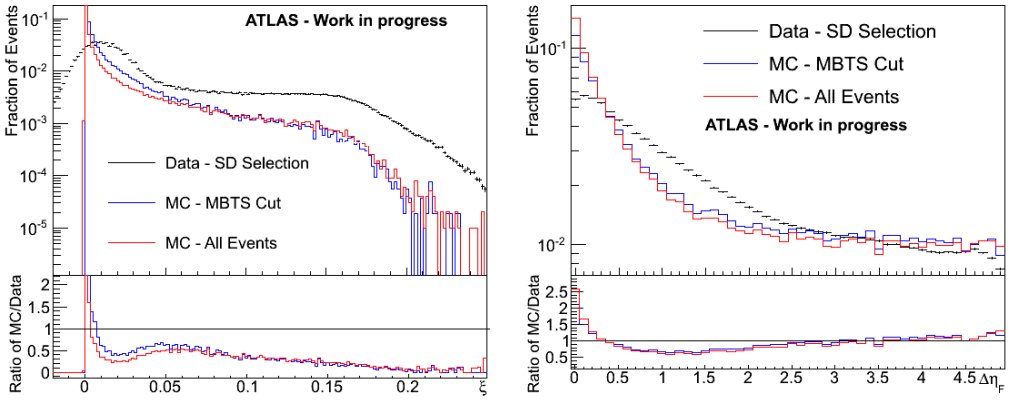

(a) (b)

Figure 14.8: A comparison of the two Monte Carlo selections with data. (a) shows the ξ distribution and (b) is the rapidity gap measurement.

greatly. The plots are shown with the further selection where the hit cut in the MBTS on the opposite side is passed, but the same side has more than eight hits, i.e. not a 'clean proton'. These events show a clear signal of high ξ events only. It is seen that only 4% of the total number of simulated events pass this requirement. This means that the 'clean proton' cut is expected, from this MC, to remove of the order 4% of the events, while it is the requirement of activity in the MBTS acceptance region on the opposite side of the proton that removes the majority of the simulated events, $\sim 42\%$. Remembering the cut-flow table, table 14.1, it is seen that the 'clean proton' cut removes $\sim 32\%$ of the data, not 4%.
This adds to the reasoning behind requiring the 'clean proton' cut in the data selection, as the majority of this third, considering this MC, is most likely non-diffractive events. Looking at the ξ distribution of figure 14.7c and figure 14.6c (for more than eight hits in the MBTS, purple line), the peak seen in data is dominant over a potential high ξ signal. This is not seen in the MC model, and therefore the 'clean proton' cut is used. However, it is quite likely that some high ξ events are excluded from data due to this cut, but the number is expected to be small.
In figure 14.8, a comparison of the two MC selections is made with the data selection of the previous section. It is seen that the agreement is not ideal, especially the ξ distribution is not great. The plateau seen in data is not expected from Monte Carlo studies, and will be discussed in the following section. The peak at zero, however, can be somewhat explained by the energy resolution measureable in ALFA, and it is therefore not thought to be as poor

as it initially seems from the plot.
In previous analysis at ATLAS, see section 9, the forward rapidity gap has been measured. They also saw an excess in data for gapsizes spanning the inner detector. However the results are not really comparable as that article involved the use of calorimeters which would greatly increase rapidity gap measurement region. It is also important to keep in mind that the MC used here is truth info only, i.e. no detector reconstruction simulation has been applied.
This discussion is closely related to acceptance studies of the ALFA and ATLAS detectors combined. The MC was made for 500,000 SD events, but only the events which came within the ALFA acceptance regions were stored. Therefore, as 196,986 events were stored, this simple MC model predicts that only about 40% of all diffractive events can potentially be seen by ALFA. Of these 40%, it has been discussed that requiring activity similar to that of the SD cuts futher reduced this by a factor $\sim$2. Therefore, this simple MC predicts a rough acceptance of the ALFA and ATLAS system of $\sim$ 20% of all SD events. Note that this is a simple simulation, and therefore this number nothing more than an indication of the true acceptance, as it does not account for effects such as detector inefficiencies.

14.3 Background

In the previous section, it has been seen that a clear SD signature is visible. However, great agreement between data and simulation has yet to be achieved, and this section will contain a background discussion as an attempt to explain some of this disagreement.

The backgound in ALFA typically originates from the beam halo, i.e. beam collision between residual LHC gas particles or beam cleaning inefficiencies that results in a halo of particles that accompany the beam.
Using the `L1_ALFA_ANY_EMPTY` trigger it is seen that hits in ALFA look similar to that of the background ellipse, see figure 14.9a. As this trigger is for event crossings with one empty bunch, this is the background signal from stray beam particles hitting ALFA, i.e. particles that are always present in the beam pipe, filled bunch collision or not. Given this trigger, there is no activity in ATLAS or LUCID while only very few events with hits in the MBTS, $\sim$ 124/27747 events. Therefore figure 14.9a shows LHC background events only. By comparing the number of events outside the diffractive banana region to the total number of events, for the `EMPTY` trigger, it is seen that $\sim$68.5% of these background events lie within the diffractive region.
Looking back at the full data selection, one can then select the events out-

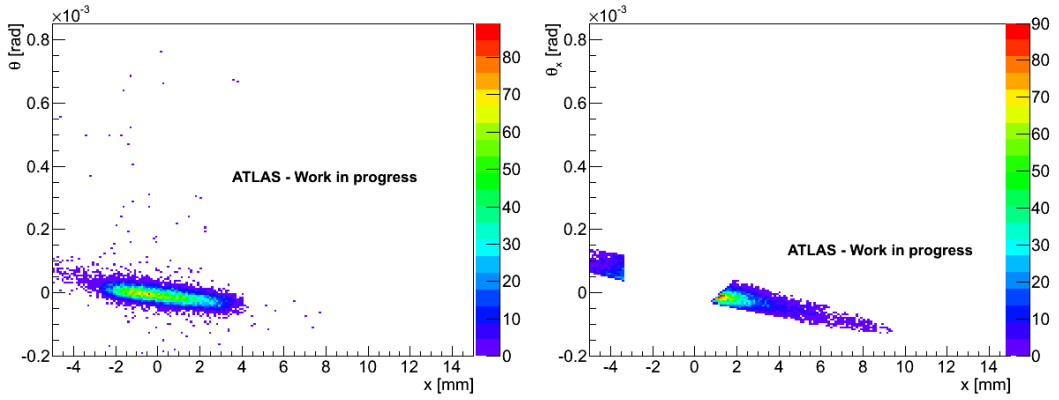

(a) (b)

Figure 14.9: (a) is the x vs θ_x plot with the `L1_ALFA_ANY_EMPTY` trigger. (b) shows the data selection events in the background ellipse outside the SD region.

side the SD region but inside the background ellipse, see figure 14.9b, and use these to estimate the SD selection background contamination from LHC particles. If one assumes that the background ellipse of the SD selection, is only background similar to that of the `EMPTY` trigger, the amount of constant background due to beam halo can be found by dividing the number of events in figure 14.9b by 0.315. It is seen that the background ellipse roughly corresponds to $\sim 1\%$ of the hits inside the diffractive banana region. This is a very rough estimate as the two shapes in figure 14.9 agree, but not perfectly. For example, the ellipse selected in data is seen to cover a larger area, and it is therefore likely to overestimate the amount of LHC background. As this number is small, background in ALFA due to the beam is considered to be small. Note also that this background estimate is done for events where nothing is supposed to happen in either ATLAS or ALFA (one empty bunch), and therefore it is not an estimate of the total background, as non-diffractive inelastic events might contribute once both bunches are filled.

To discuss the properties of background in ALFA due to internal beam collisions or beam halo particles, a selection has been made. It requires the `L1_ALFA_ANY` trigger, corresponding to a hit in any of the eight ALFA detectors. A hit in the other detector of that ALFA arm is also required, to reconstruct a track. It is also required that there are no hits in the MBTS or LUCID on both sides of ATLAS and that there is only one track in the ALFA arms, i.e. a veto on the three other ALFA arms. The selected track

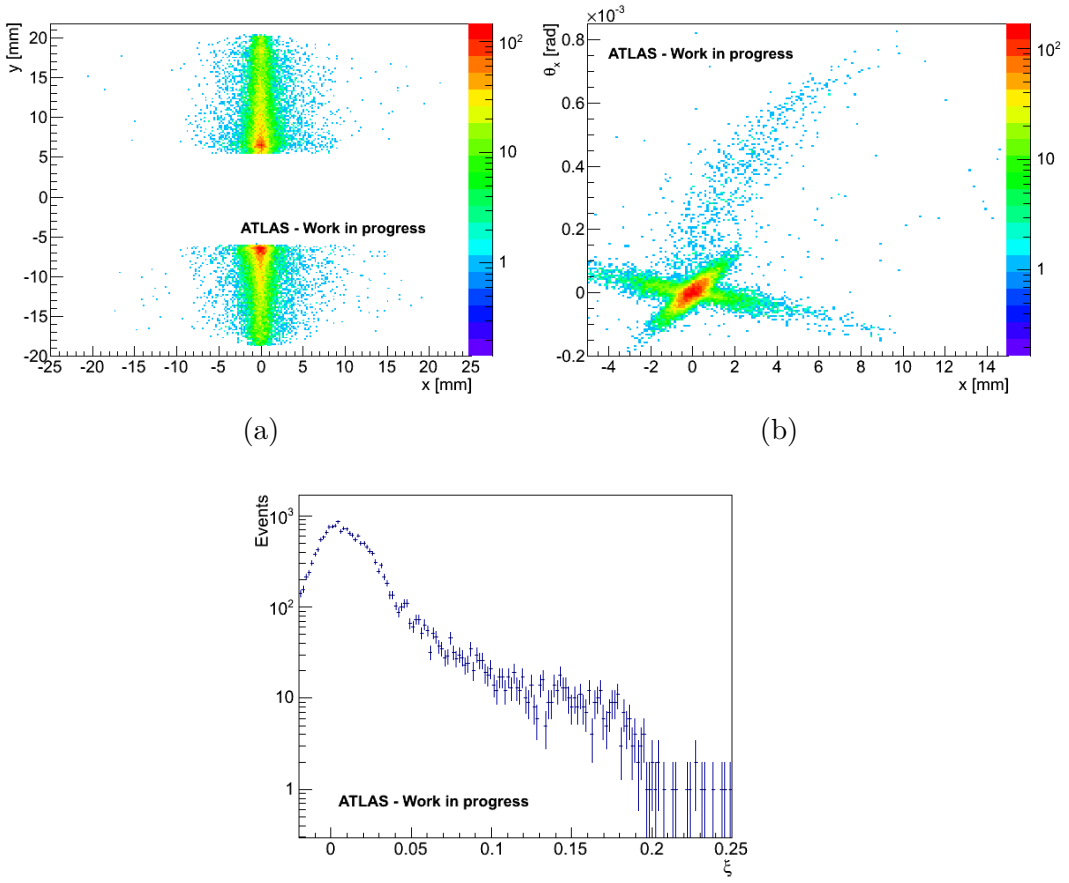

Figure 14.10: Signature of beam background in ALFA. (a) is the hit map, (b) is the x-θ_x correlation and (c) is the ξ distribtion.

is also required to pass the beamscreen and detector edge cuts. This should ensure mainly beam background particles are selected. As expected from the low pile-up probability, only a very small fraction (0.6%) of these events have a vertex in ATLAS, meaning this type of event only has activity in ALFA. This selection is heavily dominated by beam background, but a signal SD and elastic contamination of a few percent is expected, ref. [30]. These signal events are either very low ξ diffractive events, where the diffractive mass system was outside the acceptance of ATLAS, or elastic events where one proton was not seen by ALFA. The selection is taken to be only background. In figure 14.10 are plots showing the effect of these events.
It is seen that events are spread over the entire acceptance of ALFA with a significant portion within the SD signal region, figure 14.10a and 14.10b. As

this type of events are expected to occur regardless of what is happening in ATLAS, it is reasonable to assume that some of these hits in ALFA coincide with ATLAS activity, and hence creating background events that can be part of the final diffractive selection. The ellipse seen in the x-θ_x plot is similar to that of low energy loss diffractive or elastic protons. Likewise, a peak at ~ 0 energy loss is seen in figure 14.10c. It is therefore not unreasonable to assume that at least a good portion of these are in fact very low ξ diffractive events or elastic events, where the diffractive mass system or the other proton was not seen.

In figure 14.4c, a plateau in the ξ distribution is seen instead of the expected $1/\xi$ behaviour. As this behaviour is not seen in simulation and the background outside the diffractive banana region is too small to cause this, it could be the result of background contamination from inside the diffractive region, i.e. possibly beam halo particles. To investigate this plateau further, the diffractive banana region is split into the eight regions shown in figure 14.11. Each region is assigned a number from one to eight in the plot to be able to distinguish between them from now on.

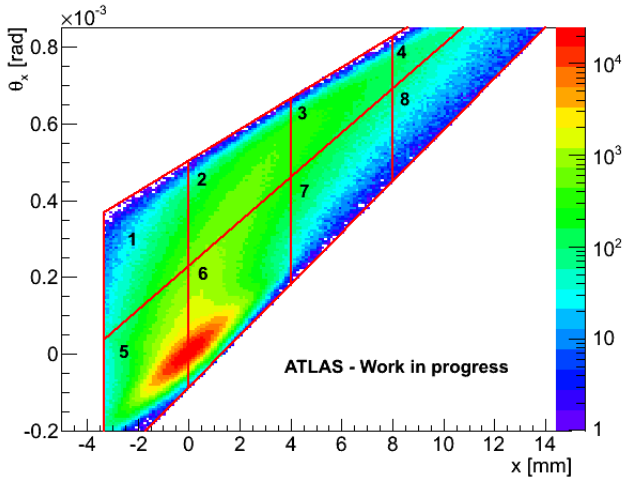

Figure 14.11: The eight regions used to investigate the plateau seen in the ξ distribution.

In figure 14.12a, the ξ distribution is shown for all events in the diffractive region as well as each of the eight regions. With the possible exception of region 1, the four upper regions, 1-4, show peak-like structures around increasing energy for higher x values.
The regions 5-8 show something different. As the low-ξ/elastic ellipse is en-

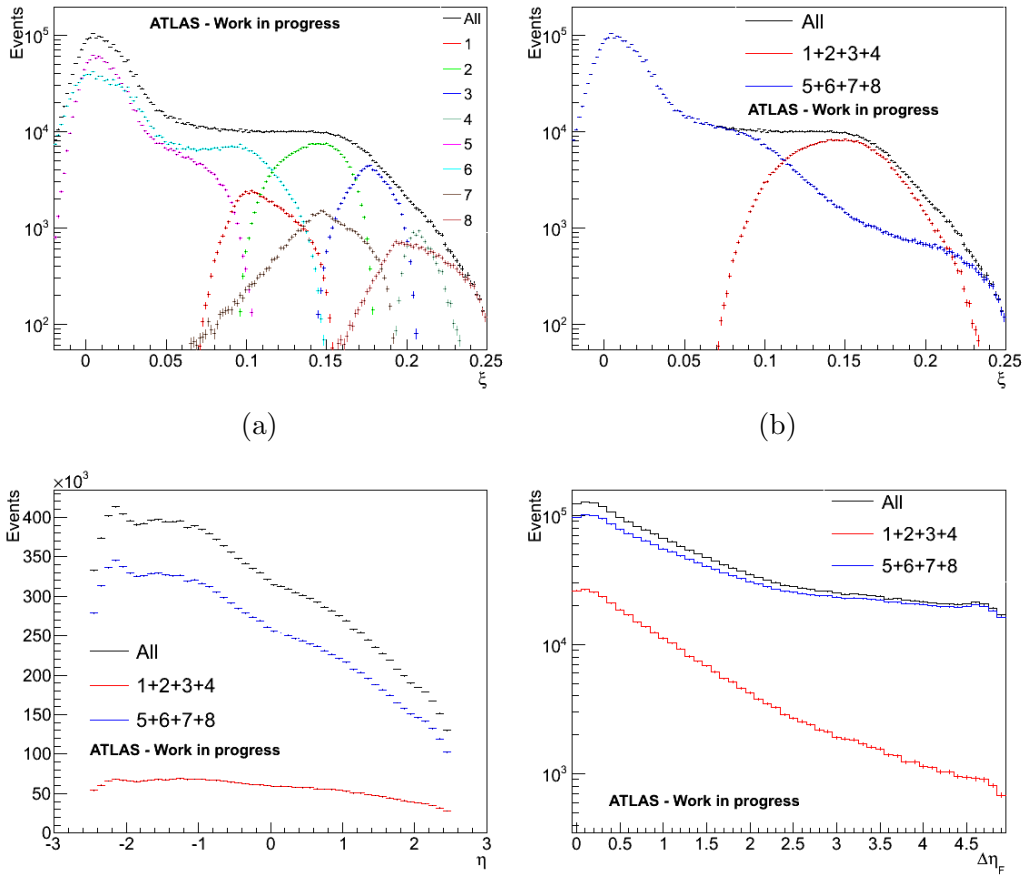

Figure 14.12: (a) shows the ξ distributions for all eight regions along with the combined distribution (black). In (b), the eight regions have been combined into two, the upper (1, 2, 3 and 4) and the lower (5, 6, 7 and 8) regions. The combined distribution is shown as well (black). (c) is the η distribution of tracks for all events, regions 1-4 and regions 5-8. (d) is the gap distribution of all events, regions 1-4 and regions 5-8.

closed by region 5 and 6, both of these make up the peak seen in the combined energy loss distribtion. But, apart from the smaller maximum at $\xi \sim 0.1$ for region 6, region 5-8 all show a decreasing number of events for higher and higher energy losses of the diffractive proton.
This indicates that a look into a combination of region 1-4 and region 5-8 could be interesting for determination of the origin of the plateau. This is shown in figure 14.12b where the ξ distribtuion of the entire diffractive ba-

nana region, region 1-8, has been plotted along with the two subsets of region 1-4 and 5-8, i.e. the lower and upper row of regions. It is seen that the lower row gives a ξ distribution without the presence of a plateau. At $\xi \sim 0.08$ and ~ 0.15 a change in the fall-off of the lower regions is seen. This is possibly due to the strict linear separation of the upper and lower rows of regions in figure 14.11. The upper row gives something that looks rather interesting as it is far from the naively expected diffractive signature, a uniformly distributed peak instead of a peak of decreasing size as a function of ξ.
Therefore, to further investigate the regions, a look into the η and gap distributions have been done for both the upper and lower regions. Figure 14.12c shows the η distributions of tracks in ATLAS for the upper, lower and combined rows while figure 14.12d shows the gap distribution.
The figures show less of an expected diffractive signature for the upper rows, seen in the η plot as a more flat distribution and in the gap plot as an exponentially suppressed distribution. However, given that the energy loss of the proton is always high for the upper row, 1-4, these events have more energy available in ATLAS. This means that the diffractive mass system has more freedom to cover a larger region of the ATLAS detector. Remember that, from appendix A, we have

$$\langle \eta_X \rangle \sim -\ln \frac{\sqrt{s}}{M_X} \quad , \tag{14.3}$$

where $\langle \eta_X \rangle$ is the average value of η for the diffractive mass system. Therefore protons in the high end of the ξ spectrum are expected to have a more uniform distribtion of tracks in η.

The background estimate of 1% is not a total background estimation as it only involved the negatively correlated ellipse seen in the SD selection in figure 14.4b.
Based on the ξ plateau discussion, an excess of high ξ events is seen in data, but the ξ plateau is not likely to originate from beam background. This is because the size of this background contamination is seen to be too small to account for the plateau. In addition, the ξ distribution of the beam background selection is seen to be exponentially suppressed. Another possibility to explain the plateau is non-diffractive inelastic events in ATLAS, however, in ref. [28], the amount of these are estimated to be a factor 30 too low to explain the plateau.

14.4 ATLAS Results

Given the SD selection described in section 14.1, it is interesting to see the properties of the selected events. This section will explore the activity in ATLAS.

Name	Value	Notes
$\lvert\eta\rvert$	< 2.5	
$\mathbf{p}_T$	> 100 MeV	
BLayer Hits	> 0	Hits in the BLayer, if expected
Pixel Hits	> 1	
SCT Hits	> 2	For $\mathbf{p}_T > 100$ MeV
	> 4	For $\mathbf{p}_T > 200$ MeV
	> 6	For $\mathbf{p}_T > 300$ MeV
$\lvert d_0^{PV}\rvert$	< 1.5 mm	If primary vertex is found
$z_0^{PV} \cdot \sin\theta$	< 1.5 mm	If primary vertex is found
$\lvert d_0^{BS}\rvert$	< 1.8 mm	If primary vertex is not found

Table 14.3: A table with the values of the η and $\mathbf{p}_T$ cuts. The BLayer, Pixel and SCT cut show the required number of hits in each layer. d_0^{PV} and d_0^{BS} is the transverse impact parameters w.r.t. the primary vertex or beam spot. Likewise, z_0^{PV} is the longitudal impact parameter w.r.t. the primary vertex. From ref. [26].

One of the most intuitive and immediate things to check is the tracks of ATLAS. However, to reduce background and noise, a track selection has to be applied to select only tracks which are considered good. This should give a clearer signal of what particles are a result of diffractive interactions, as the selection should remove most of the background tracks that can occur due to either cosmic rays or beam induced background. The selection criteria of the inner detector (ID) can be seen in table 14.3 (from ref. [26]).
This selection is not dependent on ALFA, and it is used to discuss the distributions in ATLAS, given the diffractive selection. A total of 782652 events were found with more than one vertex, where a secondary vertex is the result of pile-up collisions in a given bunch crossing, i.e. more than one interaction took place in that event. This corresponds to 4% of all events. However, given the SD selection discussed in section 14.1 this number drops to roughly 1%, and pile-up background events are thus negligible in this SD analysis.

In figure 14.13a two distributions of η of the inner detector are shown. One is a SD proton detected on the A side, and the second is the 8 TeV toy

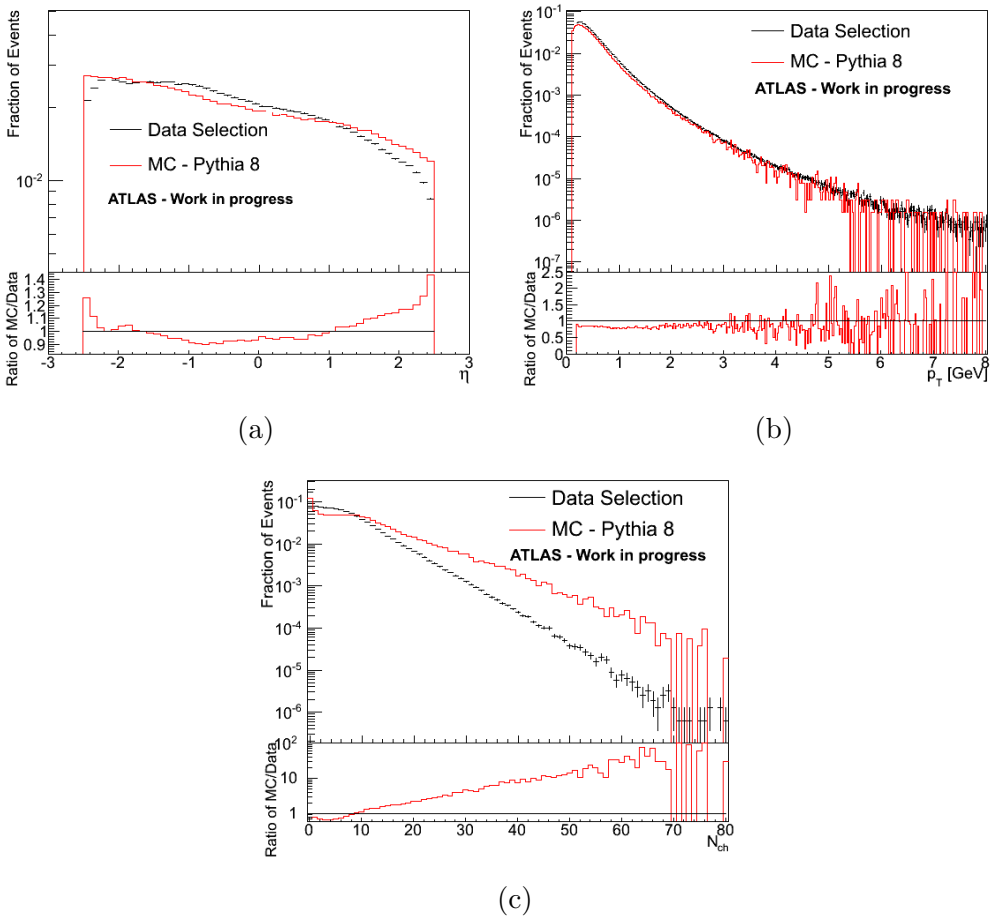

Figure 14.13: Two selections of tracks in the inner detector of ATLAS. First, a selection with a diffractive proton detected on the A side of ATLAS. Second, a simulation, using Pythia 8, with a simple selection to mirror that of the SD cuts. (a) shows the η distribution, (b) is the $\mathbf{p}_T$ and (c) is the number of charged particles, N_{ch}. Each distribution is normalized to the entries of that selection.

model MC used previously. Remember this MC only has truth information, and therefore what is shown here is only a comparison of shapes. There is a clear dependence on the side of the diffractive proton, which is expected. If a SD proton is detected on one side of ATLAS, the η distribution is shifted towards the opposite side in ATLAS. The MC and data selections are not in perfect agreement, but they do have very similar shapes. Detector effects can possibly explain some of the disagreement, especially at the edges of the inner detector.

The $\mathbf{p}_T$ and N_{ch} distributions of ATLAS, for the SD data selection and the MC, can be seen in figure 14.13b and 14.13c. The $\mathbf{p}_T$ distribution is seen to agree reasonably well with the MC, however for higher values of $\mathbf{p}_T$ the disagreement becomes worse. This is in a region of low statistics, and therefore not surprising. A disagreement between data and the MC is found in the charged particle distribution. Here it is seen that there are more events in data with few tracks ($\lesssim 10$) than the MC. Likewise it is seen that the SD data selection also has significantly less events with many tracks, compared to the MC. In this region the deviation between the two becomes very large which might indicate that something is not quite well understood.
It is seen that the agreement is not perfect between the data and MC, however the shapes of distributions agree roughly. Remembering that the MC is only a toy model, no real conclusion can be made before a full detector simulation is made, and these distribution only gives indications of an agreement.

14.5 Further Analysis

Given the previous discussion regarding SD events, there are still questions to be answered. The first and possibly most interesting is the selection efficiency and acceptance studies. The current SD selection was developed using only data, and therefore a detailed study on efficiencies and acceptance of the selection using a full detector simulation is of high interest. This would hopefully help to clarify how much background is actually present in the selection. In addition, this would help provide answers on the effect of requiring the 'clean proton' cut and the events possibly cut away by this requirement.

In section 14.3, a discussion on the plateau of the energy loss distribution, ξ, was done. It revealed interesting sub-division of the diffractive protons in the ALFA x-θ_x plot of the SD data selection. To study the dependence of the energy of the proton as a function of the x coordinate and θ_x with which the proton hits ALFA could therefore be of great interest. This might also help in the determination of whether the plateau effect is due to background in ALFA or if the current models of SD does not correctly predict the amount of higher ξ events.

The activity in ATLAS, given a selected diffractive proton in ALFA, seems to be distributed similarly to that of minimum bias distributions but with shifted η distribution, reflecting the forward production of the diffractive mass system. However, some disagreements were seen, and a more detailed simulation including detector effects might clarify this.
In section 9, a previous result with ATLAS concerning rapidity gaps was men-

tioned, however without the tagging of the forward diffractive proton. The obviuos question is then, does tagging the proton give distributions closer to the expected diffractive signature. To do this, a minimum bias data sample is needed, as the data analysed in this thesis is diffractive dedicated, and therefore only include events which seemed interesting from an ALFA perspective. In addition to this, the inclusion of the calorimeter data is expected to improve the gap measurements.

15 Central Diffraction

The second type of diffractive event that it is possible to see, using ALFA and ATLAS, is central diffractive (CD) events. In this section, a cut-flow for this type of diffractive events will be introduced. In addition, a study of the activity in ATLAS is also presented, and this includes the rapdity gap measurements and track distribtutions. A first look into colour flow measurements is also presented. As this part of the analysis was done towards the end of the thesis, it is not done is as great detail as the SD selection and analysis. The CD analysis is preliminary due to the focus on the SD analysis in this thesis.

CD events are expected to be the result of a double Pomeron exchange causing both protons to survive the interaction with an energy loss. The diffractive mass system is then the result of this double Pomeron collision, and an important difference from SD events is that this diffractive system is not necessarily required to be produced in the forward region. This is due to both protons remaining in the final state, both carrying a large fraction of their initial energies.

15.1 The CD Selection

The cut-flow for CD events is shown in table 15.1. An error in the code used in the analysis was found when applying the beamscreen cut, but not in time to correct it. Therefore the beamscreen cut number is not included, but it is expected (from the SD analysis) to be of the order of the detector edge cut, ~ 350, and therefore not of great importance.
The triggers used are `L1_ALFA_ELAS15/18`, `L1_MBTS_2_A/C_ALFA_C/A` and `L1_ALFA_ANY`. Some of the cuts are similar to those of the SD selection and will not be described here. Note that, due to the requirement of two diffractive protons, the veto, beamscreen and detector edge cut are changed to allow for this. There are four allowed combinations of the two protons as they are

Cut-Flow	Number of events
Total number of events	18,095,900
Luminosity cut	17,266,910
Trigger	12,098,910
Reconstructed tracks	11,645,680
Multiplicity cut	8,597,109
Veto on other tracks	2,206,130
Vertex cut	1,411,802
BG Elastics cut	97,193
Beam screen cut	97,193
Detector edge cut	96,855

Table 15.1: The cut-flow for CD events of the combined 8 TeV data runs, 206881 and 206885. On the left, the cuts are mentioned, while on the right the number of events remaining after the cut in the given run is written.

not necessarily required to be back-to-back like elastics, and therefore, given a track in one of the ALFA arms on one side, a track is also required in one of both arms on the other side.
In addition to this change, a vertex cut is also required due to the expected centrality of the diffractive system. It is naively expected, with some correlation of the energy losses of both protons, that the distributions in ATLAS correspond roughly to that of minimum bias.
The elastic signal dominates over the CD signal for ξ values close to zero, and therefore, to remove some of them, it is required that the hits are not back-to-back, reflecting the fact that the protons have not lost the same amount of energy and therefore have different kinematics. This cut is only applied to CD candidates that have protons in the two elastic modes of ALFA, detector $1+3+6+8$ or $2+4+5+7$.
This is also the reason to require that events that have hits in one of the elastic arm combinations do not pass the elastic x vs θ_x background cut.

Figure 15.1 show the result of the selection. 15.1a is the xy hit map in ALFA, and 15.1b is the corresponding x-θ_x correlation. The hit map is similar to that of the SD selection which is expected. Likewise, the x-θ_x plot shows the same signature as SD events.
In figure 15.1c, the ξ distributions of the two protons is shown. They are plotted against each other to check for any correlations between the energy losses. No such correlation is seen, but a plateau effect similar to that seen in SD events is visible as the yellow regions along both of the axis.

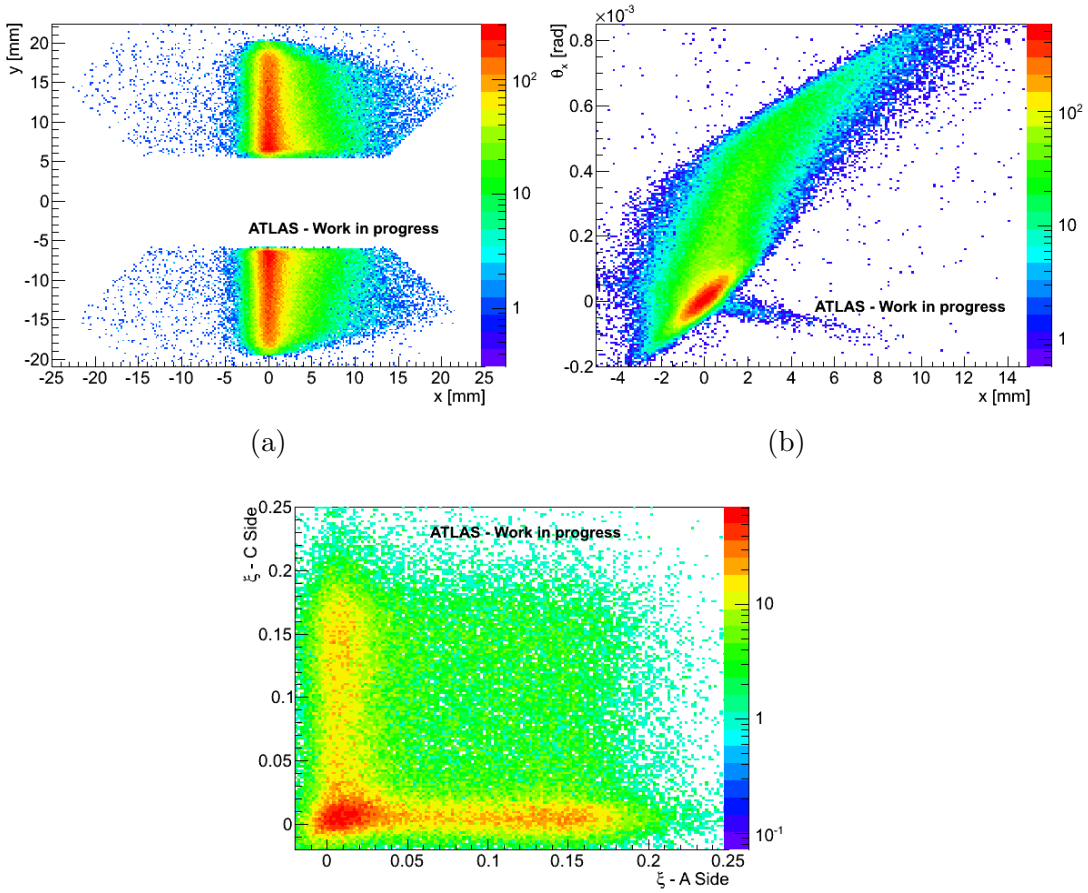

Figure 15.1: The CD data selection for the entire data run. (a) shows the hit map, the x coordinate plotted against the y coordinate. (b) is the correlation between the x coordinate and θ_x angle. In plot (c) the correlation of the energy loss, ξ, of the two protons is shown.

Background is seen in figure 15.1. 1.7% of the events found have one of the two protons outside the diffractive region, and no events have both protons outside.

Figure 15.2 shows a comparison between the CD data selection and the elastic selection with an additional vertex requirement. Figure 15.2a shows the MBTS hits for the CD cuts and 15.2b is the elastic selection. It is seent that these two distribution have similar structures, but the amount of events are distributed differently. The CD selection has two bands at zero MBTS

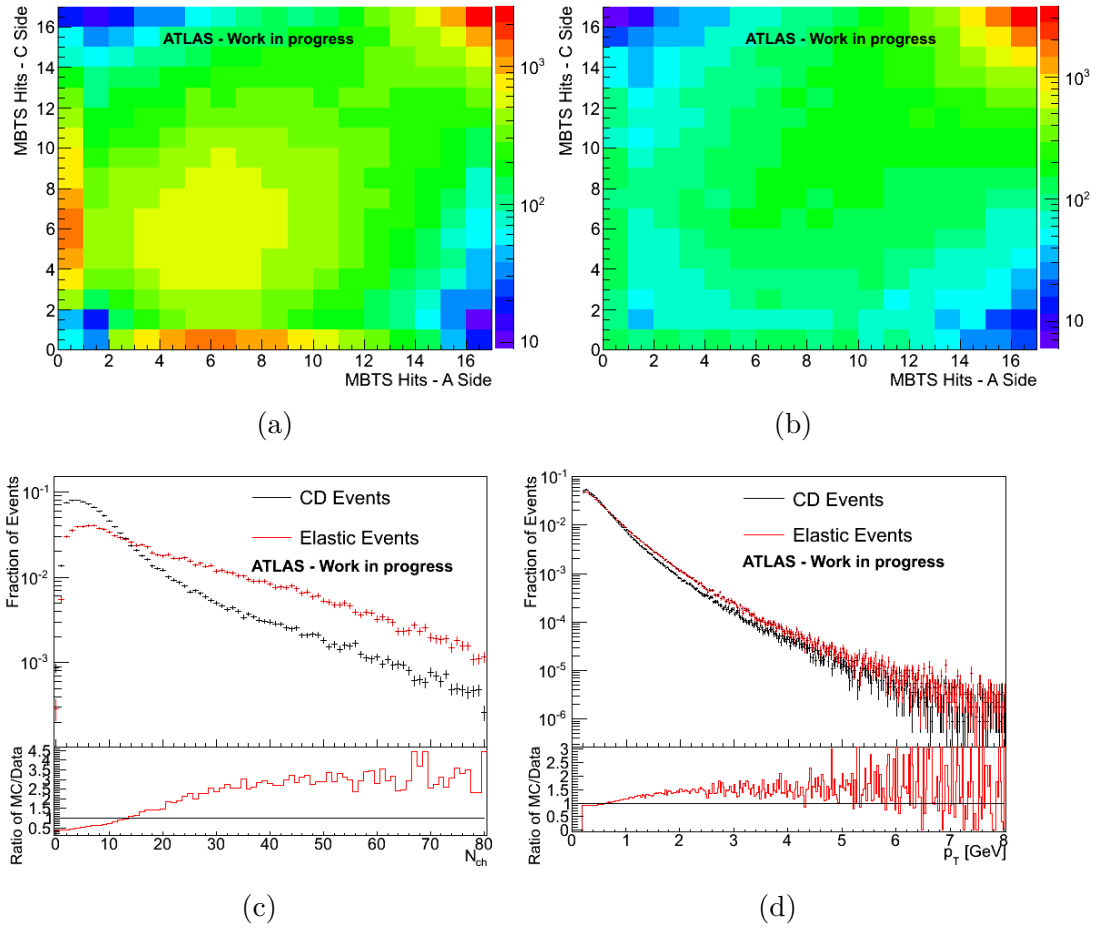

Figure 15.2: The CD cuts compared to the elastic cuts (with a vertex). (a) shows the MBTS hits for the CD selection, (b) is the elastic selection. (c) shows a comparison of the charged multiplicity distribution and (d) is a comparison of the $\mathbf{p}_T$ distribution.

hits, similar to those seen in SD events, and a region where both sides have around six MBTS hits. Quite a few events are seen to have hits in almost all of the MBTS, the region around 16 hits on both sides. The elastic selection is seen to have a high event count in this region as well, but the other structures are suppressed in comparison with the CD selection. Looking at the charged track distributions, N_{ch} in figure 15.2c and $\mathbf{p}_T$ in 15.2d, some disagreement is seen. The elastic selection has relatively more events with a higher multiplicity and transverse momenta. This, along with the MBTS hit count plot, indicates that the majority of the elastic selected events are pile-up events, with one elastic event and one non-diffractive event. This is because, if the elastic events were in fact CD events, they would be low energy loss CD events, i.e. the diffractive mass system would not have a high amount of energy available.
The CD cut selection is seen to have clear diffractive signatures in ALFA. In ATLAS, the comparison to elastic events (with vertex in ATLAS) is seen to have different track distribution. Due to time issues this could not be investigated further.

15.2 CD Event Properties

The properties of the diffractive mass system of a CD event have not been studied before at a $\sqrt{s} = 8$ TeV collision energy. This section will discuss some of the properties of the CD events using angle studies on the diffractive mass system of CD events. In addition, using a MC simulation, a first attempt at a study of the sensitivity of the Pomeron trajetory parameters will be presented.

The Pomeron is colourless, but it is thought to be made of two or more gluons, sometimes called 'glueballs'. As CD events are thought to happen due to a double Pomeron exchange, it can therefore be interesting to look into the colour flow, to try to understand the Pomeron substructure or if they are allowed to interact with each other via triple-Pomeron vertices.
Originally, when measuring the existence of the triple-gluon vertex, event shape angles were devised to describe how the colour flowed. These studies considered final states with two quarks and two gluons, where the two gluons were final state radiation. This can happen in three different ways. The first two was where two gluons were radiated separately from the quarks of the final state. The third was a single gluon being radiated, and that gluon then, via triple gluon vertex, split into two. In the latter, the two gluons are colour connected, and this causes some substructure which is measureable using these angles. See ref. [31].

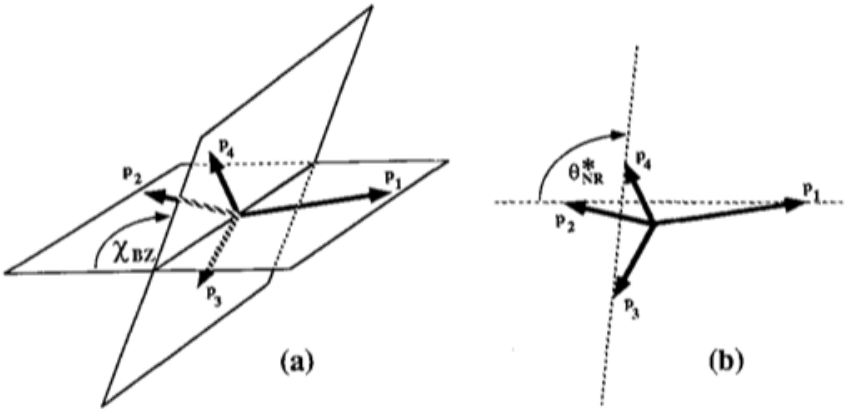

Figure 15.3: An example of (a) the Bengtsson-Zerwas and (b) the Nachtmann-Reiter angles. [31].

The angles are defined by the momentum vectors of the four particles, $\mathbf{p}_1$, $\mathbf{p}_2$, $\mathbf{p}_3$ and $\mathbf{p}_4$. These are energy ordered such that $E_1 > E_2 > E_3 > E_4$. The first angle is the Bengtsson-Zerwas (BZ) angle, defined as

$$\cos\theta_{BZ} = \frac{(\mathbf{p}_1 \times \mathbf{p}_2)(\mathbf{p}_3 \times \mathbf{p}_4)}{|\mathbf{p}_1||\mathbf{p}_2||\mathbf{p}_3||\mathbf{p}_4|} \quad . \tag{15.1}$$

The second angle is the modified Nachtmann-Reiter (NR) angle,

$$\cos\theta^*_{NR} = \frac{(\mathbf{p}_1 - \mathbf{p}_2)(\mathbf{p}_3 - \mathbf{p}_4)}{|\mathbf{p}_1 - \mathbf{p}_2||\mathbf{p}_3 - \mathbf{p}_4|} \quad . \tag{15.2}$$

An example of these two angles can be seen in figure 15.3. Another angle one might consider is the Körner-Schierholtz-Willrodt (KSW) angle defined as

$$\cos\theta_{KSW} = \frac{(\mathbf{p}_1 \times \mathbf{p}_3)(\mathbf{p}_2 \times \mathbf{p}_4)}{|\mathbf{p}_1||\mathbf{p}_3||\mathbf{p}_2||\mathbf{p}_4|} \quad . \tag{15.3}$$

The nature of the Pomeron interaction of a diffractive event is not known, and, as CD events are the result of two Pomerons interacting, the CD selection is a good choice to further study Pomeron interactions. As a first preliminary attempt at studying the colour flow, the method used for triple-gluon couplings is tested on CD events. The goal is to be able to determine if triple-Pomeron vertices are allowed or if they are only allowed to collide via other particles. See figure 15.4 for an example of a triple-Pomeron vertex and an alternative way for a double Pomeron exchange to occur.
This study was done using a Pythia 8 CD Monte Carlo (MC) simulation with a Pomeron flux described by the MBR (Minimum Bias Rockefeller) model,

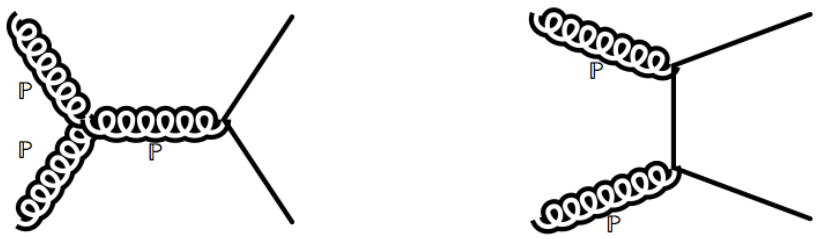

(a) (b)

Figure 15.4: Two Feynmann diagrams of Pomeron interactions. (a) shows a possible interaction given a triple-Pomeron vertex is allowed. (b) is an example of an interaction given triple-Pomeron vertices are forbidden.

see appendix C. This MC is compared to the data selection of CD events. As this is only a first look into these parameters, the naive selection of the four highest momentum tracks was used. From these four tracks, the angles can be measured and compared. In addition to looking for possible colour flow structures, the MC simulation were made for different parameter values of the Pomeron trajectory to study if the angles are sensitive to these parameters. Remembering section 4.2, the Pomeron trajectory is

$$\alpha_{\mathbb{P}}(t) = \alpha(0) + \alpha' t \quad , \tag{15.4}$$

where $\alpha(0)$ is the intercept and α' is the slope of the trajectory. Six different values of intercept were chosen, 1.02, 1.046, 1.072, 1.098, 1.124 and 1.15, and these simulations were done using a slope of 0.25. Likewise four steps of the slope were chosen, 0.1, 0.2, 0.3 and 0.4, all with an intercept of 1.085. In figure 15.5 the result for the BZ angle is shown, 15.5a is the intercept comparison and 15.5b is the slope comparison. Data and MC shows a rough agreement for angles up to around $|\cos\theta_{BZ}| = 0.9$, and for angles close to 1 the MC and data disagree. It is seen that the angles are clumped together towards $|\cos\theta_{BZ}| = 1$. The result for the other two angles can be seen in appendix B.2, and the shapes are seen to be similar. Looking at the effect of changing the parameters in the MC, no clear dependence is seen on either the slope or the intercept of the Pomeron trajectory for any of the angles.

As these angles showed no depence on the Pomeron trajectory, it is possible that other distributions will show a sensitivity. A look at the three distributions of η, $\mathbf{p}_T$ and N_{ch} was done. The result for the charged multiplicity, N_{ch}, can be seen in figure 15.6. It seen that the MC only describes the data with a very rough accuracy, and no visible dependence of the Pomeron trajectory

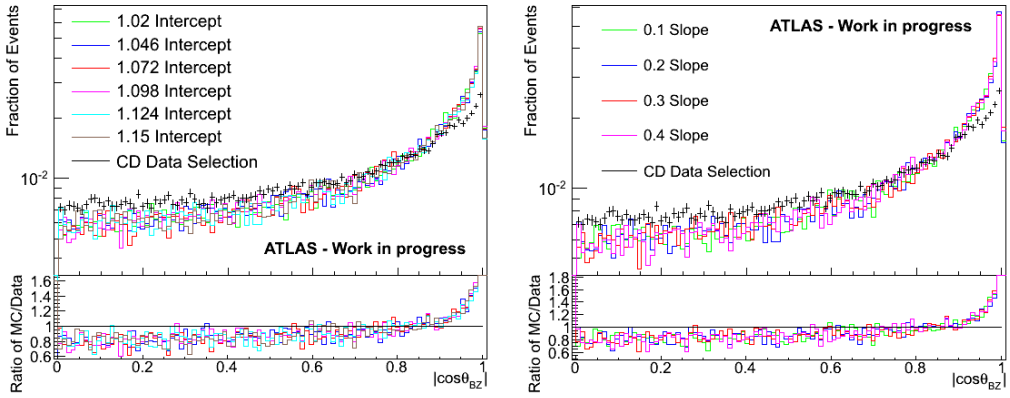

(a) (b)

Figure 15.5: A first attempt to look at the Bengtsson-Zerwas angle distribution for CD event and a Pythia 8 Simulation. The simulation is done six times with different values of Pomeron trajectory intercept and four times with different values of Pomeron trajectory slope. A ratio of MC and data is also included. (a) are the six values of intercept, and (b) are the four values of slope.

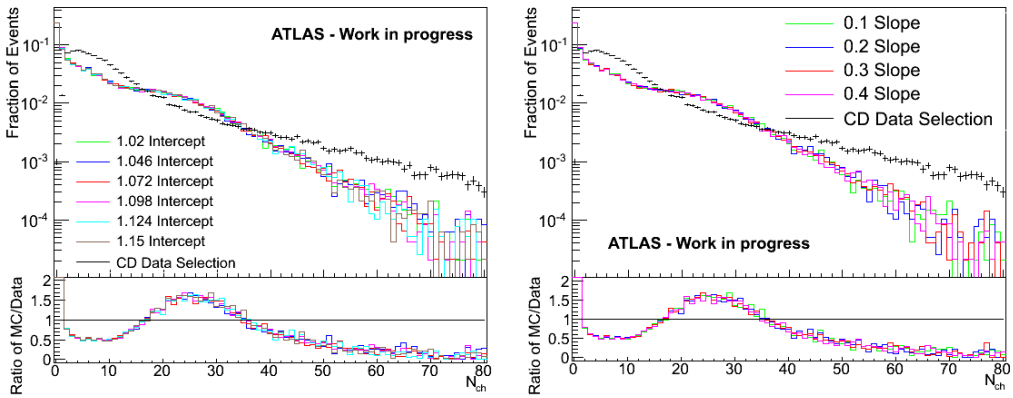

(a) (b)

Figure 15.6: The charged mulitiplicity distribution for data and a simple CD MC simulation using Pythia 8. The simulation is done six times with different values of Pomeron trajectory intercept and four times with different values of Pomeron trajectory slope. A ratio of MC and data is also included. (a) are the six values of intercept, and (b) are the four values of slope.

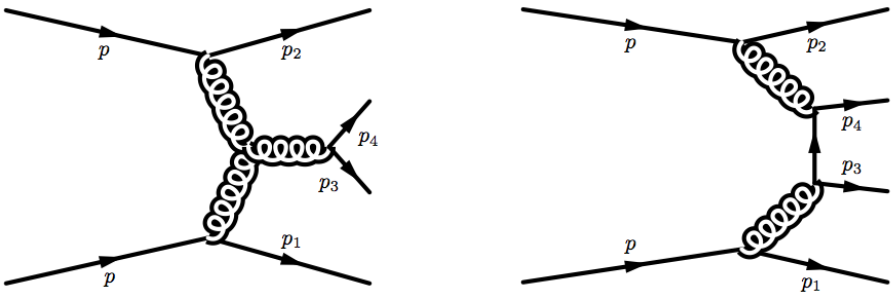

(a) (b)

Figure 15.7: An Feynmann diagram example of future angle studies using the diffractively scattered protons. (a) shows the triple-Pomeron vertex and (b) an alternative way for CD events to happen.

is present. The other two distributions show no sensitivity to the Pomeron trajectory and the same level of distribution accuracy of the MC. They can be seen in appendix B.3.

15.2.1 Further Colour Flow studies

Studies like this have not been done before, and only one CD simulation model was available. Therefore no conclusion can de drawn, except that this model shows some agreement with data, and it is not sensitive to the parameters of the Pomeron trajectory. Note that, as only one CD MC model was available, the result could not be compared to other predictions.
To discuss whether any first clues of a colour flow is visible in figure 15.5, one needs to know the predictions of how dominant each type of diagram would be and what the shape of that contribution would be. For example, the fact that a triple-gluon vertex is allowed meant that more events were observed in the low angle regime, as opposed to the contribution without a triple-gluon vertex (more events with higher angles). No conclusion can be drawn regarding the colour flow, as the exact details of this specific MC model's description of CD events was unknown to the author of this thesis, or even if a triple-Pomeron vertex description is included in the model.
The naive approach of using the angles devised for studying triple-gluon vertices was only the first step, but it does open up for more possibilities regarding studies of colour flow and triple-Pomeron vertices.
An example is shown in figure 15.7 of how the two protons could be included into the angle calculation. This is a more direct measurement of the colour flow of the Pomerons as all particles used are directly coupled to the Pomeron, while currently only two of the particles have direct couplings. This mea-

surement is possible, as the reconstruction code used to find the energy of the proton in ALFA is also able to determine the x and y components of the momentum. In this case one would also have to think about the optimal plane selection for calculating the angles. One possibility is the angle between the plane spanned by the two protons and the plane spanned by the two tracks (or jets). However, the angle between the plane spanned by the highest energy proton and highest energy track/jet and the plane spanned by the lowest energy proton and track/jet could also be interesting. Which gives a better sensitivity, if any, is not known currently.

This is only one of the follow up possibilities to the first step taken in this thesis. Different studies and methods are possibly also interesting and relevant in determining whether a colour flow can be measured in CD events or if a triple-Pomeron vertex is allowed.

16 Concluding Remarks

The aim of this thesis was to develop a selection for single diffractive (SD) and central diffractive (CD) events, and, in addition to this, study some of the properties of these events.
A selection of SD events was found in section 14 which showed clear diffractive signatures, such as a roughly constant forward rapidity gap distribution, $\Delta\eta_F$, and an energy loss, ξ, which is seen to have a peak at low energy losses and a decreasing number of events for higher ξ. These two distributions roughly match the model description of the toy model 8 TeV MC simulation. However, in the energy loss distribution, a plateau was seen around relative energy losses of the proton of ~ 0.05 to ~ 0.15. Further investigation into the origin of this was done by dividing the diffractive banana region into eight and comparing the different regions' contribution to the ξ distribution. It was seen that an excess of high ξ diffractive candidate protons were found. However, a definite conclusion could not be drawn as to whether these were background or our current expectation is incorrect. A rough estimate of the acceptance of the ALFA and ATLAS combined system was found to be $\sim 20\%$ for SD events, but a more detailed study might change this number significantly.
A look into the background of ALFA was also done, and a rough estimate of around 1% background was found due to beam particles inside the diffractive banana region. This estimate does not include background from other sources, such as inelastic non-diffractive events in ATLAS. Further analysis would be needed to give a more accurate estimation of the background. Besides this, a look at the η, $\mathbf{p}_T$ and multiplicity distributions of charged tracks in ATLAS was done. These were compared to a simple toy model MC and seemed to agree. However the agreement was not perfect, therefore a further study of the impact of detector effects on the MCs description of data is needed.

A preliminary selection of CD events was also included. This was not analysed in as great detail as the SD selection, but it still showed promise for future CD analysis. The ξ loss distribution of the two protons showed no correlation between the amount of energy lost by each proton. Given the discussion on elastic events versus CD events, further studies could give insight into whether the elastic events (with a vertex) are indeed pile-up event between an elastic and a non-diffractive event. From the MBTS hit count plot, a 'clean proton' cut might be of interest in further discussions of this.
Looking into event shapes, the Bengtsson-Zerwas, Körner-Schierholtz-Willrodt and Nachtmann-Reiter angles, it was seen that they do not appear to be sen-

sitive to the Pomeron trajectory parameters of Regge theory, at least with this model. As a first step towards measuring triple-Pomeron vertices and the colour flow of CD events, it was seen that these angles roughy describes data. More information about the assumptions behind the model is needed to be able to predict the size and shape of the contribution due to a triple-Pomeron vertex, and thus compare this to the seen distribution in data. However, this conclusion applies only to this single simulation model of CD events, and it is therefore not a general result.

The next step in this analysis will be to complete the full simulation of 8 TeV diffractive events and use this to determine background contaminations and calculate acceptance and efficiencies of the two selection. In addition to this, an inclusion of the calorimeter data is expected to give more information regarding the rapidity gap measurements and possibly improve the selection developed. A first step was also taken towards measuring if a triple-Pomeron vertex is allowed, and the next step would be to use different or new methods to measure this, such as including the protons in the angle calculations.

17 Bibliography

References

[1] Regina Kwee (on behalf of the ATLAS Collaboration), 34th International Conference on High Energy Particle Physics, Philadelphia, 2008 [arXiv:0812.0613v1 [hep-ex]].

[2] Dan Green, *High P_T Physics at Hadron Colliders*
Cambridge University Press, 2005.

[3] David Griffiths, *Introduction to Elementary Particles*
Wiley-VCH, 2nd edition, 2008.

[4] Vincenzo Barone & Enrico Predazzi, *High-Energy Particle Diffraction*
Springer, 2002.

[5] Sandy Donnachie, Otto Nachtmann, Peter V. Landshoff & Gunter Dosch, *Pomeron Physics and QCD*
Cambridge, 2002.

[6] http://lhc-machine-outreach.web.cern.ch/lhc-machine-outreach/ .

[7] http://www.lhc-closer.es/1/4/18/0 .

[8] http://en.wikipedia.org/wiki/A_Large_Ion_Collider_Experiment .

[9] http://en.wikipedia.org/wiki/LHCb .

[10] http://en.wikipedia.org/wiki/Compact_Muon_Solenoid .

[11] http://accelconf.web.cern.ch/accelconf/e94/PDF/EPAC1994_0208.PDF

[12] http://www.atlas.ch/detector.html .

[13] http://en.wikipedia.org/wiki/ATLAS_experiment .

[14] http://www.kip.uni-heidelberg.de/ stamen/LECTURES/JC/PDFs/atlaslumi.pdf .

[15] Sune Jakobsen,
Performance evaluation and optimisation of the luminosity detector ALFA
Master thesis, 2008.

[16] http://www.physik.uni-giessen.de/atlas/publications/overlap.pdf .

[17] ATLAS Collaboration, Eur. Phys. J. C72 (2012) 1926
[arXiv:1201.2808 [hep-ex]].

[18] ATLAS Collaboration, New J.Phys.13:053033, 2011
[arXiv:1012.5104 [hep-ex]].

[19] J.R. Cudell, K. Kang, S.K. Kim, International Conference, *Recent Advances in Hadron Physics*, 1996
[arXiv:9712235v1 [hep-ph]].

[20] Benno List, for the H1 Collaboration, Progress in High Energy Physics, Vol. 3 (2009)
[arXiv:0906.4945[hep-ex]].

[21] https://atlas-trigconf.cern.ch/run/smkey/1433/l1key/8131/hltkey/6734/
.

[22] http://atlas-runquery.cern.ch/query.py?q=find+run+206881+/+show+all
.

[23] http://atlas-runquery.cern.ch/query.py?q=find+run+206885+/+show+all
.

[24] http://atlas-runquery.cern.ch/query.py?q=find+run+191373+/+show+all
.

[25] Internal ALFA meetings and ALFA code,
The ALFA Elastic analysis group.
https://svnweb.cern.ch/trac/atlasphys/browser/Physics/StandardModel/QCD/ALFA/Code/Elastic7TeV/EvSel .

[26] http://etheses.bham.ac.uk/3954/1/Martin12PHD.pdf .

[27] Morten Ankersen Medici,
Diffraction with ALFA and ATLAS at $\sqrt{s} = 8$ *TeV.*
Master thesis, August 30th, 2013.

[28] Simon Stark Mortensen,
Kinematic recontruction of diffractive processes with tagged protons in the ALFA detector at $\sqrt{s} = 8$ *TeV.*
Master thesis, August 30th, 2013.

[29] http://cds.cern.ch/record/719263/files/gen-2004-001.pdf .

[30] Beam Background,
AFP Collaboration meeting. June 19th, 2013, by Hasko Stenzel.

[31] A study of angular correlations in 4-jet final states of hadronic Z^0 decays.
OPAL Collaboration
http://link.springer.com/article/10.1007/BF01570796 .

17.1 Figure List

[32] http://commons.wikimedia.org/wiki/File:Standard_
Model_of_Elementary_Particles.svg .

[33] http://www.quantumdiaries.org/wp-content/uploads/2012/03/pdf.jpg
.

[34] http://www.borborigmi.org/2012/06/28/rivelatori-di-particelle-a-lhc-
ottava-parte-spray-di-particelle-ovvero-come-si-vedono-quark-e-gluoni/
.

[35] http://www-cdf.fnal.gov/physics/new/top/2007/topProp/KA_Afb/ .

[36] http://en.wikipedia.org/wiki/File:Pseudorapidity2.png .

[37] https://cds.cern.ch/record/1482078/files/ATL-COM-PHYS-2012-
1435.pdf .

[38] http://insti.physics.sunysb.edu/ siegel/reggepart/reggepart.html .

[39] http://www.physics.helsinki.fi/vuosikertomukset/2011/
research/elementary_particle_physics.html .

[40] http://arstechnica.com/science/2010/08/following-protons-
on-a-trip-to-and-through-the-lhc/ .

[41] http://www.lhc-closer.es/1/4/18/0 .

[42] http://iopscience.iop.org/1367-2630/8/11/290/fulltext/ .

[43] http://scipp.ucsc.edu/personnel/atlas.html .

[44] http://www.interactions.org/cms/?pid=2100&image_no=CE0155 .

[45] http://www.jetgoodson.com/images/thesisImages/magnetSystems.png
.

[46] http://www.atlas.ch/inner-detector.html .

[47] http://www.atlas.ch/calorimeter.html .

[48] http://project-atlas-lucid.web.cern.ch/project-atlas-lucid/taskforce/main_old.html .

[49] http://atlas-project-lumi-fphys.web.cern.ch/atlas-project-lumi-fphys/default_10112011.html .

[50] http://www.sciencedirect.com/science/article/pii/S0168900207017135 .

[51] https://twiki.cern.ch/twiki/bin/view/AtlasPublic/ForwardDetPublicResults#ALFA_figures .

[52] ALFA readiness review. (13 August 2009), Christian Joram (http://indico.cern.ch/conferenceDisplay.py?confId=62776).

[53] Ref. [15] on page 57.

[54] Diffractive run with ALFA,
Standard Model Plenary Meeting, September 20th, 2012, by Oldrich Kepka.
https://indico.cern.ch/conferenceDisplay.py?confId=153439 .

[55] Experience with elastic events - diffractive background,
Workshop on diffractive analyses with ALFA, October 9th 2012, by Hasko Stenzel.
https://indico.cern.ch/conferenceDisplay.py?confId=209475 .

[56] The ALFA detector system,
ALFA-ATLAS diffractive physics at NBI. September 3rd, 2012, by Sune Jakobsen.
https://indico.cern.ch/conferenceDisplay.py?confId=206054 .

[57] http://www.atlas.ch/news/2006/first-physics-lar.html .

A Appendix - Variables of Diffractive System

To kinematically describe a single diffractive system, it is useful to first look at a two-body process, $1 + 2 \to 3 + 4$. In the center-of-mass (CM) system the four momentum is:

$$\begin{aligned} p_1 &= (E_1, 0, 0, p_z) \\ p_2 &= (E_2, 0, 0, -p_z) \\ p_3 &= (E_3, \mathbf{p}_T, p'_z) \\ p_4 &= (E_4, \mathbf{p}_T, -p'_z) \quad , \end{aligned} \tag{A.1}$$

where $\mathbf{p}_T$ is the two component transverse momentum vector. This also gives the relation

$$|\mathbf{p}_T| = |p'| \sin\theta \quad , \tag{A.2}$$

where θ is the scattering angle and p' is the four momentum of one of the final state particles, i.e. 3 or 4. The CM energy is $\sqrt{s} = \sqrt{(p_1 + p_2)^2}$ and the energies can be expressed in terms of s as

$$\begin{aligned} E_1 &= \frac{s + m_1^2 - m_2^2}{2\sqrt{s}} \\ E_2 &= \frac{s + m_2^2 - m_1^2}{2\sqrt{s}} \\ E_3 &= \frac{s + m_3^2 - m_4^2}{2\sqrt{s}} \\ E_4 &= \frac{s + m_4^2 - m_3^2}{2\sqrt{s}} \quad . \end{aligned} \tag{A.3}$$

With the mass shell condition, $p^2 = m^2$, one gets the equation

$$\begin{aligned} p^2 = p_z^2 &= E_1^2 - m_1^2 \\ &= \frac{1}{4s}(s^2 + m_1^4 + m_2^4 + 2sm_1^2 - 2sm_2^2 - 2m_1^2m_2^2 - 4sm_1^2) \\ &= \frac{1}{4s}(s^2 + m_1^4 + m_2^4 - 2sm_1^2 - 2sm_2^2 - 2m_1^2m_2^2) \quad , \end{aligned} \tag{A.4}$$

where this is the result for both p and p' due to the similarity of the energies. In cases where the masses are equal, this reduces to

$$p = p' = \sqrt{\frac{(s^2 - 4sm^2)}{4s}} = \frac{\sqrt{s - 4m^2}}{2} \quad . \tag{A.5}$$

Another important limit is the high energy limit where $s \gg m_1^2, m_2^2, m_3^2, m_4^2$. In this limit, the size of the momentum becomes

$$p = p' \sim \frac{\sqrt{s}}{2} \quad . \tag{A.6}$$

Now consider the Mandelstam variable,

$$t = (p_1 - p_3)^2 = m_1^2 + m_3^2 + 2(|p||p'|\cos\theta - E_1 E_3) \quad . \tag{A.7}$$

In the case where all masses are equal, this and the previous equations can be used to find the scattering angle,

$$\cos\theta = 1 + \frac{2t}{s - 4m^2} \quad , \tag{A.8}$$

while the momentum reduces to equation A.5. In the massless limit, $s \gg m_1, m_2, m_3, m_4$, the equations reduce to

$$\begin{aligned} \cos\theta &\sim 1 + \frac{2t}{s} \\ |p| &\sim \frac{\sqrt{s}}{2} \quad . \end{aligned} \tag{A.9}$$

Now consider the single diffractive process, $1 + 2 \to 3 + X$. In this case the variable $M_X^2 = (p_1 + p_2 - p_3)^2$ is used as the invariant mass of the system X. Even though the system X is not a particle on its mass shell, and therefore not a constant, it can be treated as the fourth particle in the previous equations. Therefore m_4 can be replaced by M_X, but it is assumed that now both s and M_X^2 is greater than the masses m_1^2, m_2^2, m_3^2. Thus the energies and momenta is

$$\begin{aligned} |p| = p_z \sim \frac{\sqrt{s}}{2}, \quad E_1, E_2 \sim \frac{\sqrt{s}}{2} \\ |p'| \sim \frac{s - M^2}{2\sqrt{s}}, \quad E_3 \sim \frac{s - M^2}{2\sqrt{s}} \quad . \end{aligned} \tag{A.10}$$

From this and equation A.7 one can write

$$\begin{aligned} \cos\theta &= \frac{t - m_1 - m_3 + 2E_1 E_3}{2|p||p'|} \\ &= \frac{t + \frac{s - M_X^2}{2}}{\frac{s - M_X^2}{2}} \\ &= 1 + \frac{2t}{s - M_X^2} \quad , \end{aligned} \tag{A.11}$$

when $s, M_X^2 \gg m_1^2, m_3^2$. Likewise it is found that

$$\mathbf{p}_T^2 \sim -t\left(1 - \frac{M_X^2}{s}\right) \quad , \tag{A.12}$$

since $s \gg t$. The momentum loss fraction, defined as

$$x_F \equiv \frac{|p_z'|}{p_z} \quad , \tag{A.13}$$

is also a variable often used to describe a diffractive event. Because the transverse momentum is usually small in high energy collision, the approximation $|p_z'| \sim p'$ can be made. Thus x_F becomes

$$x_F \sim 1 - \frac{M_X^2}{s} \quad , \tag{A.14}$$

using the above approximations. This also means that, using equation A.12, $\mathbf{p}_T = -tx_F$.

The rapidity, defined as

$$y = \frac{1}{2}\ln\frac{E + p_z}{E - p_z} \quad , \tag{A.15}$$

is another variable used in the description of diffractive events. In the limit where $\mathbf{p}_T \gg m$ the rapidity is the same as the pseudorapidity. The transverse mass is

$$\begin{aligned} m_t &= \sqrt{m^2 + \mathbf{p}_T^2} \Rightarrow \\ E &= \sqrt{m_t^2 + p_z^2} \quad . \end{aligned} \tag{A.16}$$

In the limit $p_z \to \infty$ the rapidity is

$$y \sim \ln\frac{2p_z}{m_t} \quad . \tag{A.17}$$

Hence, when considering a single diffractive process, the rapidity of the remaining proton is

$$y_3 \sim \ln\frac{2p_z'}{m_t} \sim \ln\frac{s - M_X^2}{m_t\sqrt{s}} = \ln\frac{\sqrt{s}}{m_t} \quad . \tag{A.18}$$

Then, considering the rapidity of the diffractive system X, this can be thought of approximately as a particle of momentum $p_z \sim -\sqrt{s}/2$. The average rapidity of the system is therefore

$$\langle y_X \rangle = -\ln\frac{\sqrt{s}}{M_X} \quad , \tag{A.19}$$

with a maximal and minimal rapidity of

$$|y_{X,\max}| \sim \ln \frac{\sqrt{s}}{m} \quad \text{and} \quad |y_{x,\min}| \sim \ln \frac{m\sqrt{s}}{M_X^2} \quad . \tag{A.20}$$

The rapidity gap, defined as the difference in rapidity of the remaining proton and the lowest rapidity of the system X, is then

$$\Delta y = \ln \frac{\sqrt{s}}{m} - - \ln \frac{m\sqrt{s}}{M_X^2} = \ln \frac{s}{M_X^2} \quad . \tag{A.21}$$

This can be coupled to the momentum loss fraction, x_F, by

$$1 - x_F = e^{-\Delta\eta} \quad , \tag{A.22}$$

in the limit $y \sim \eta$, the pseudorapidity.

B Appendix - Additional Figures

B.1 SD Selection - Side comparison

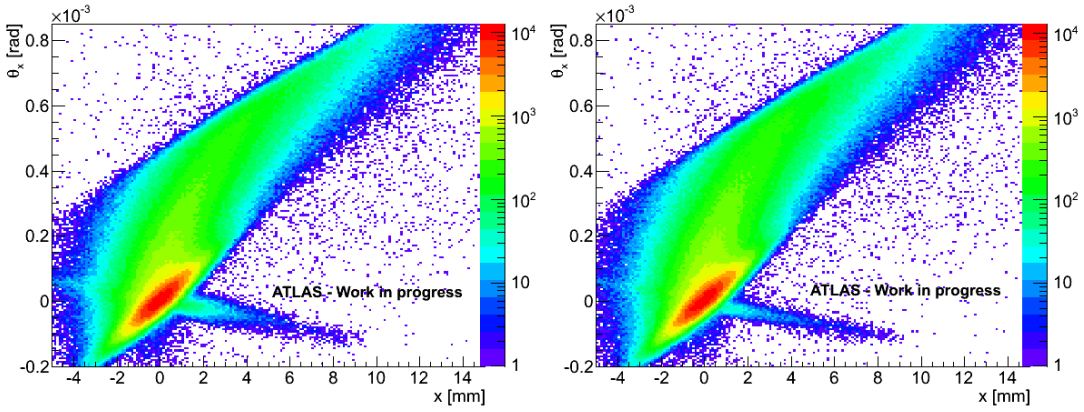

(a) (b)

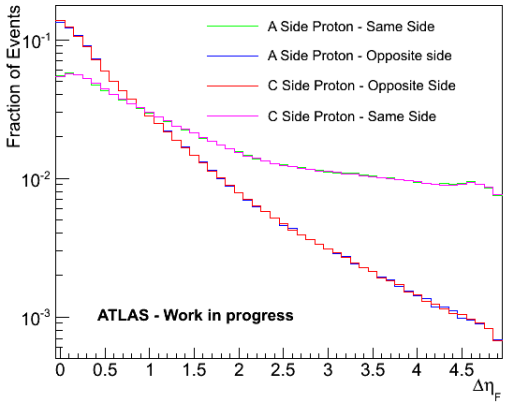

(c)

Figure B.1: (a) and (b) show the x-θ_x plots, (a) is the A side and (b) is the C side. (c) shows a comparison of gap sizes measured with a proton on the A and C side.

B.2 CD Angle studies

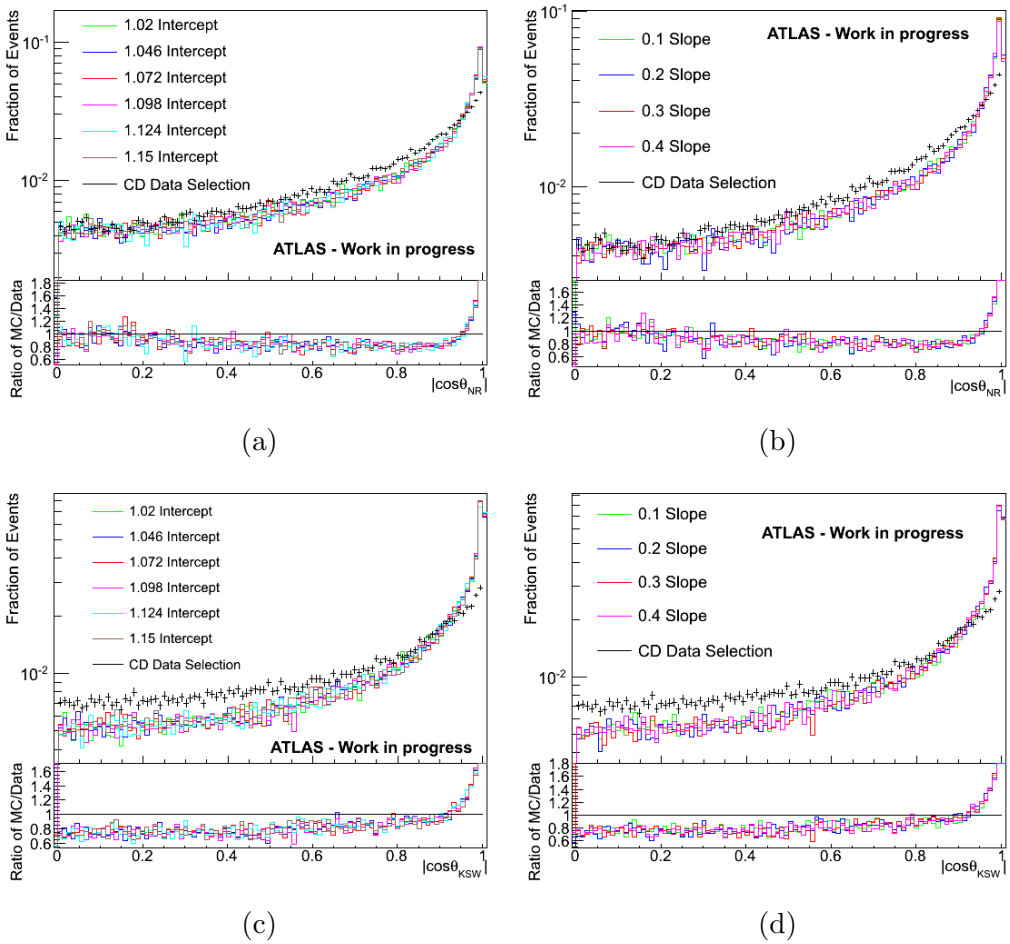

Figure B.2: (a) and (b) shows the θ_{NR} angle distributions. (a) is the angle with a sensitivity of the Pomeron trajectory intercept comparison, and (b) is a sensitivity of the Pomeron trajectory slope comparison. (c) and (d) are the same, but for the θ_{KSW} angle.

B.3 CD Pomeron studies

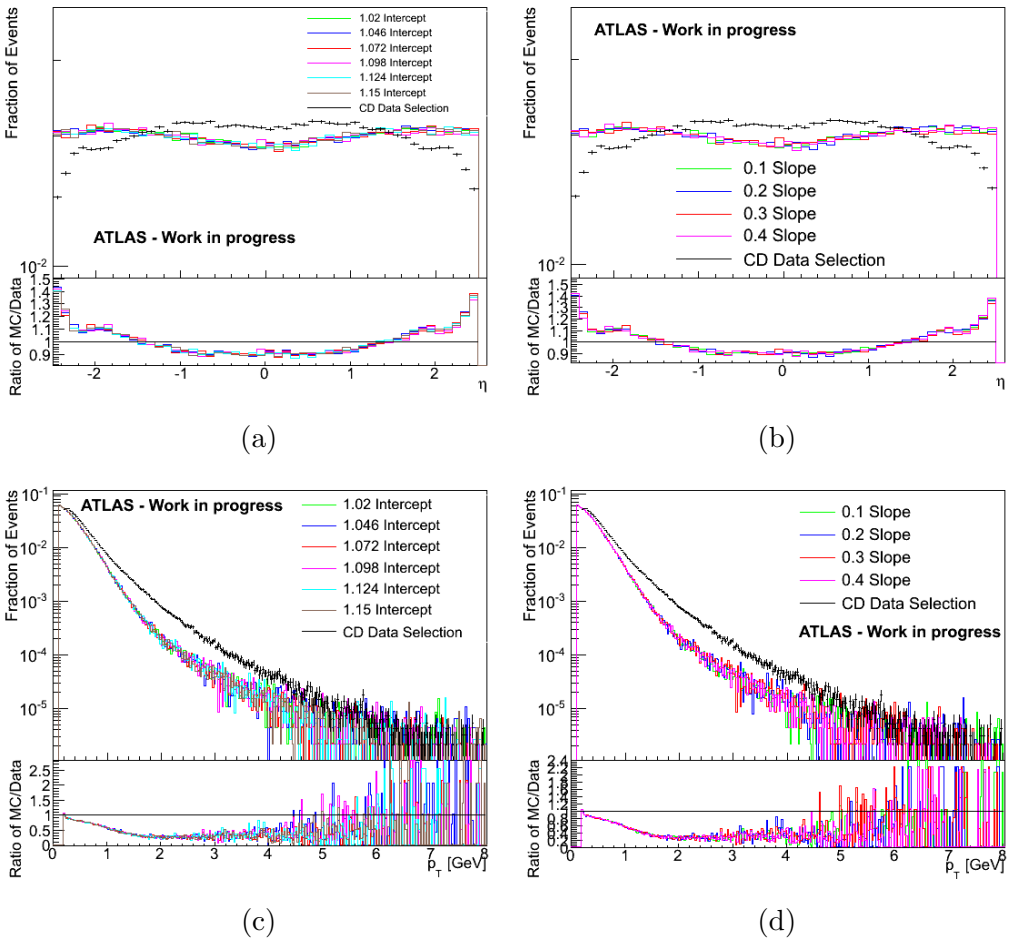

(a) (b)

(c) (d)

Figure B.3: (a) and (b) shows the η distributions. (a) is the η distribution with a sensitivity of the Pomeron trajectory intercept comparison, and (b) is a sensitivity of the Pomeron trajectory slope comparison. (c) and (d) are the same, but for the $\mathbf{p}_T$ distributions.

C Appendix - Data Sets

Data

8 TeV Data

data12_8TeV.00206881.physics_ALFA.NTUP_MINBIAS_BS
data12_8TeV.00206885.physics_ALFA.NTUP_MINBIAS_BS

7 TeV Data

data11_7TeV.00191373.physics_ALFA.merge.RAW

Monte Carlo Simulations

8 TeV

Pythia 8 MC Simulation of SD events - 500,000 events simulated, provided by Peter Hansen (supervisor)
Pythia 8 MC Simulation of CD events - 100,000 events simulation, made by the author.